INFORMATION TO USERS

This manuscript has been reproduced from the microfilm master. UMI films the text directly from the original or copy submitted. Thus, some thesis and dissertation copies are in typewriter face, while others may be from any type of computer printer.

The quality of this reproduction is dependent upon the quality of the copy submitted. Broken or indistinct print, colored or poor quality illustrations and photographs, print bleedthrough, substandard margins, and improper alignment can adversely affect reproduction.

In the unlikely event that the author did not send UMI a complete manuscript and there are missing pages, these will be noted. Also, if unauthorized copyright material had to be removed, a note will indicate the deletion.

Oversize materials (e.g., maps, drawings, charts) are reproduced by sectioning the original, beginning at the upper left-hand corner and continuing from left to right in equal sections with small overlaps.

Photographs included in the original manuscript have been reproduced xerographically in this copy. Higher quality 6" x 9" black and white photographic prints are available for any photographs or illustrations appearing in this copy for an additional charge. Contact UMI directly to order.

Bell & Howell Information and Learning
300 North Zeeb Road, Ann Arbor, MI 48106-1346 USA
800-521-0600

ANALYSIS OF AIRBORNE FLUX MEASUREMENTS OF HEAT, MOISTURE AND CARBON DIOXIDE, AND THEIR CORRELATION WITH LAND COVER TYPES IN BOREAS

Segun Ojo Ogunjemiyo
Department of Natural Resource Sciences, McGill University
Montreal, Canada, April 1999

A Thesis Submitted to
the Faculty of Graduate Studies and Research
in Partial Fulfilment of the Requirements
for the Degree of Doctoral of Philisophy

ABSTRACT

Analysis of airborne flux measurements of heat, moisture and carbon dioxide, and their correlation with land cover types in BOREAS.

Segun Ojo Ogunjemiyo, Department of Natural Resource Sciences, McGill University
Ph.D. in Micrometeorology, February 1999.

The landscape of the boreal forest in north-central Canada is characterised by mosaics of broad-leaved deciduous trees (aspen, *Populus;* birch, *Betula*), evergreen conifers (black spruce, *Picea mariana*; jack pine, *Pinus banksiana*; and larch, *Larix)*, fens and lakes. The forest has been cited as the possible location of a global carbon sink, and its likely response in the event of global climate change remains unclear. To improve our current understanding of the links between the boreal forest ecosystem and the lower atmosphere, the Boreal Ecosystem-Atmosphere Study (BOREAS) was executed in a series of field experiments in 1994 and 1996. This thesis documents the efforts made to characterise and map temporal and spatial distributions of the fluxes of heat, water vapour and CO_2 over two 16 km x 16 km heterogeneous sites at the BOREAS study sites.

Most of the data in this thesis were obtained from the airborne observations by the Canadian Twin Otter Aircraft, operated by the Institute for Aerospace Research of the Canadian National Research Council, at the BOREAS Northern Study Area (NSA), and Southern Study Area (SSA). The research aircraft was flown at a fixed altitude of about 30 m agl . The data acquired in 1994 were primarily used to develop an objective deterending scheme in eddy-correlation flux estimates, that took into consideration the physical nature of turbulent transport during convective daytime conditions, and to map the spatial distribution of sensible heat, latent heat and CO_2 fluxes over three intensive field campaigns. Maps of spatial patterns of the surface characteristics, such as the surface temperature excess over air temperature (T_s-T_a) and Greenness index (GI), were also constructed. The mapping procedure involved generation of an array of grid points by block averaging the parameter

of interests along the flight lines, spaced 2 km apart, over 2 km windows, with 1 km overlap between adjacent windows. The (T_s-T_a) maps showed, not surprisingly, that surface temperatures were relatively cooler over the mature forests than over the disturbed, regenerating and burn areas. However, they also showed a decoupling between sensible heat flux and T_s-T_a not seen in less complex terrain. By contrast, close correspondence was observed between maps of CO_2 flux and greenness, suggesting that the potential to infer CO_2 exchange from remote sensing observations of the surface is higher than that for energy exchange. Quantitative comparison of the flux maps for the three IFCs showed that the CO_2 flux was the most conservative of the three fluxes, while latent heat flux showed the highest variations.

In order to examine persistence and variability in the distributions of surface characteristics and fluxes between 1994 and 1996, the data obtained during 1994 IFC-2 were compared with those that were acquired in 1996. Sensitivity analysis suggested relatively minor effects of boundary layer variability and window size on the main features of the estimated source/sink distributions. By comparing the coefficients of variation of the fluxes with those of net radiation, the dominant role of surface inhomogeneity, as opposed to local variations in solar energy input, on spatial variation of flux distributions was confirmed. Mesoscale motion was found negligible over the grid sites, probably due to the small sizes of homogeneous subareas with sufficient surface contrast to induce thermally generated motion. The previously observed low correlation, due to decoupling between sensible heat flux and surface minus air temperature difference (T_s-T_a) primarily over old black spruce, was confirmed.

Attempts were also made to establish quantitative relationships between the observed fluxes and the cover types within the flux footprint of the airborne observations. Using the footprint function that was developed from the tracer gas release experiments above the boreal forest, the fractions of cover types within the footprint were determined, and were used in a regression analysis against the observed airborne fluxes within the grids. The results showed that, depending on the flux types, as much as 80% to 92% of the variations in the fluxes were explained by the cover types that contributed to them. Model validation using a set of independent data showed high correlations between the observed and predicted

estimates. The study provided a necessary first step in scaling up from local to regional observations based on surface information accessible to remote sensing.

RÉSUMÉ

Analyse des mesures aéroportées de flux de chaleur sensible, de chaleur latente et de bioxyde de carbone, et de leur correlation avec la composition des ecosystèmes forestiére de BOREAS.

Segun Ojo Ogunjemiyo, Département des sciences sur les ressources naturelles, Université McGill. Doctorat en micrométéorologie, février 1999.

La forêt boréale du centre du Canada est caractérisée par un mosaïque de feuillus (peuplier, *Populus*; bouleau, *Betula*), conifères (épinette, *Picea mariana*; pin, *Pinus banksiana*; mélèze, *Larix*), marécages et lacs. Cette forêt a été considéré comme un puit potentiel du carbon à l'échelle terrestre, et sa réponse à un changement éventuel du climat est loin d'être connue. Afin d'améliorer nos connaissances en ce qui concerne les liens entre l'écosystème forestier et l'atmosphère, le projet BOREAS (boreal ecosystem-atmosphere study) a été exécuté sous forme d'une série d'études sur le terrain en 1994 et 1996. Cette thèse présente le cheminement permettant de caractériser et de cartographier dans l'espace et le temps la distribution des flux de chaleur sensible, de l'humidité et de bioxyde de carbone (CO_2) de deux sites hétérogènes (16 km x 16 km) dans le territoire étudié dans BOREAS.

Les données utilisées dans cette étude proviennent largement des observations aéroportées de l'avion de recherche Twin Otter, opéré par l'Institut pour la recherche spatiale du Conseil national de recherche du Canada à des sites nord (NSA) et sud (SSA) du terrain BOREAS. L'altitude de vol était d'environ 30 m au dessus de la surface durant ces essais. Les données recueillies en 1994 ont été surtout utilisées pour développer une approche objective pour éliminer les tendances dans les signaux utilisés pour l'estimation des flux par la méthode des fluctuations ('eddy covariance') et pour cartographier la distribution spatiale des flux de chaleur sensible, d'humidité et du CO_2 durant trois campagnes de mesure intensives. La covariance de tourbillons prend en considération la nature physique du transport turbulent convectif typique de journées ensoleillées. Les distributions des

caractéristiques de surface, la différence de température entre la surface et l'atmosphère (T_s-T_a) et l'indice de végétation, ont également été cartographiées. La cartographie a été basé sur une matrice générée a partir de moyennes mobiles des variables de 2 km le long des lignes de vol (qui étaient séparées par 2 km), avec un chevauchement d'un km. Les cartes de (T_s-T_a), peu surprenant, montrent que les températures de surface étaient plus basses pour les forêts matures que celles des forêts perturbées, en régéneration ou antérieurement brulée. Cependant, elles montrent aussi , à la différence des écosystèmes plus homogènes, un decouplage entre le flux de la chaleur sensible et la variable (T_s-T_a). En revanche, une correspondence étroite a été observé entre les distributions de l'indice de végétation et celles du flux du CO_2. Ceci suggère que les des observations par télédétection ont un meilleur potentiel d'estimation de l'échange du CO_2 que l'estimation du bilan d'énergie. La comparaison quantitative des flux révéle que le flux de CO_2 était plus stable entre les différentes campagnes de mesure, tandis que celui de la chaleur était le plus variable.

Afin d'examiner la persistance et la variabilité dans la distribution des flux et des caractéristiques de surface entre 1994 et 1996, les données recueillies lors de la campagne d' été de 1994 ont été comparées à celles de 1996. L'analyse de sensibilité suggère une influence relativement faible de la structure de la couche limite atmosphérique ainsi que de la longueur de la moyenne mobile utilisée par la cartographie numérique sur l'estimation de la distribution des puits/sources. La comparaison entre la variabilité des flux et celles du rayonnement net confirme le rôle dominant de l'hétérogénéité de la surface (par rapport à celle du rayonnement solaire, qui était relativement constant) sur la variabilité des flux. La circulation à méso-échelle était négligeable au-dessus de ces deux sites, probablement à cause de l'absence de parcelles suffisamment homogènes, avec contraste thermique prononcé, pour déclencher une circulation thermique à cette échelle. La corrélation faible entre le flux de chaleur et la différence de température (T_s-T_a), observée particulièrement au-dessus des épinettes en 1994, a été confirmé en 1996.

Cette thèse a également essayé de formuler des relations quantitatives entre l'observation des flux et les types de végétation à l'intérieur de 'l'empreinte ("footprint"),EP, des observations aéroportées. Fondée sur une expression analytique de EP, développée par des expériences de diffusion d'un gaz traceur au-dessus de la forêt boréale, les pourcentages

des divers types de couverts végétaux à l'intérieur de EP ont été déterminés et utilisés dans une analyse de régression des observations de flux. Les résultats montrent que, dépendant du type de flux, autant de 80% à 92% de la variation des flux pouvait être expliquée par la composition de la surface qui contribuait du le flux. La validation du modèle de régression par des données indépendantes a montré une forte corrélation entre les prévisions et les observations. Cette étude représente une première démarche nécessaire dans nos efforts à extrapoler des mesures locales vers l'échelle régionale, à partir d'information sur la surface terrestre provenant de la télédétection.

PREFACE

The main theme of this thesis is to analyse airborne data that were collected by the Canadian Twin Otter flux research aircraft at two heterogeneous sites in the boreal forest. The goal is to generate data that can be used to validate boundary layer models, and to explore the potential for estimating fluxes from land cover data.

Results are presented as chapters in manuscript format, with the relevant literature review contained in each section. Each chapter is relatively independent but integral to the thesis, and statements that link the following chapter to the preceding one are provided. A general introduction and literature review are given in Chapters 1 and 2, respectively. The introduction is used to highlight the global climate change problem, the need for the BOREAS project and its objectives, and the main focus of this thesis. The literature review summarises the theory of some of the techniques used for the data analysis, and the Twin Otter flight missions in BOREAS. Chapter 3 is focused on the method of analysis and interpretation of the airborne data, which were obtained at two grid sites in BOREAS 1994. In Chapter 4 the data from 1994 IFC-2 are compared with those that were obtained in the 1996 field experiment. The possibility of establishing relationships between the fluxes of sensible heat, latent heat and CO_2, and land cover types that are within the flux footprint of the airborne observations, is discussed in Chapter 5. The appendix is used to present the results of a preliminary comparison between aircraft observed fluxes and satellite-based flux estimates.

STATEMENT FROM THE THESIS OFFICE

In accordance with the regulation from the Faculty of Graduate Studies and Research of McGill University, the following statement excerpted from the Guidelines for Thesis preparation (McGill University 1998) is included:

Candidates have the option of including, as part of the thesis, the text of one or more papers submitted, or to be submitted, for publication, or the clearly-duplicated text (not the reprints) of one or more published papers. These texts must conform to the "Guidelines for Thesis Preparation" with respect to font size, line spacing and margin sizes and must be bound together as an integral part of the thesis.

The thesis must be more than a collection of manuscripts. All components must be integrated into a cohesive unit with a logical progression from one chapter to the next. ***In order to ensure that the thesis has continuity, connecting texts that provide logical bridges between the different papers are mandatory.***

The thesis must conform to all other requirements of the "Guidelines for Thesis Preparation" in addition to the manuscripts. ***The thesis must include the following***: (a) a table of contents; (b) an abstract in English and French; (c) an introduction which clearly states the rational and objectives of the research; (d) a comprehensive review of the literature (in addition to that covered in the introduction to each paper); (e) a final conclusion and summary

Additional material must be provided where appropriate (e.g. in appendices) and in sufficient detail to allow a clear and precise judgement to be made of the importance and originality of the research reported in the thesis.

In the case of manuscripts co-authored by the candidate and others, the candidate is required to make an explicit statement in the thesis as to who contributed to such work and to what extent. The supervisor must attest to the accuracy of this statement at the doctoral oral defense. Since the task of the examiners is made more difficult in these cases, it is in the candidate's interest to clearly specify the responsibilities of all the authors of the co-authored papers.

ADVANCEMENT TO SCHOLARLY KNOWLEDGE

1. Contribution to Knowledge

To the author's knowledge, the following aspects of the thesis constitute original contributions to knowledge.

(1) The development of an objective detrending scheme for airborne eddy correlation signals obtained over heterogeneous surfaces, based on a method that takes into account the physical nature of transport during convective daytime conditions. Until now the choice of a detrending method was, at best, based on the traditional visual inspection of the scalar traces

(2) A method of creating and analysing flux maps of scalars for the purpose of assessing the spatial variability of the scalar and to determine the significance of the flux variability factors, as well as delineating persistence features.

(3) A systematic comparison of flux maps against remote sensing observations of surface characteristics, to explore the potential of using the latter to infer surface-atmosphere exchange of northern boreal forests.

(4) Demonstration of the potential to estimate surface-atmosphere fluxes in a heterogeneous area through regression relationships that link observed fluxes to the fractions of cover types, as a first step in scaling up from local to regional observation.

2. Research Papers in Refereed Scientific Journals

(1) Ogunjemiyo, S.O, P.H. Schuepp, J. I. MacPherson and R.L Desjardins, (1999) : Comparison of the spatial and temporal distribution of fluxes of sensible heat, latent heat, and CO_2 from grid flights in BOREAS 1994 and 1996. *J. Geophys. Res.* In press

(2) Ogunjemiyo, S.O, N. Bussières, P.H. Schuepp, and R.L Desjardins, and J. I. MacPherson, (1998) : Comparison of airborne and satellite-derived maps of heat and moisture fluxes over a boreal forest ecosystem (in French). *Le Climat*, **15** (1)11-32

(3) Ogunjemiyo, S.O, P.H. Schuepp, J. I. MacPherson and R.L Desjardins, (1997) : Analysis of flux maps versus surface characteristics from Twin Otter grid flights in BOREAS 1994 . *J. Geophys. Res.* **102**(D24)29,135-29,145

CONTRIBUTION OF CO-AUTHORS TO MANUSCRIPTS

The first author was solely responsible for the analysis of all the airborne data, preparation of manuscripts for publication, and responses to the reviewers' comments.

Dr. P.H. Schuepp, the author's supervisor, undertook the administrative operation of all research projects, with involved in the design and execution of the grid flights, contributed through research supervision, editorial work, and provided extensive comments on all manuscripts.

Dr. R.L. Desjardins was involved in the data collection, and provided comments and editorial help on paper (1)

Mr. J.I MacPherson was responsible for the Twin Otter aircraft, involved in the design and execution of the grid flights and data collection, and provided comments and editorial help on paper (1) (Chapter 5)

Dr. N. Bussiéres provided the satellite data and analysis used in paper (2) (Appendix)

ACKNOWLEDGEMENTS

First of all, I wish to thank my wife, who is carrying our first baby, for her unique patience, understanding and support.

My sincere thanks go to my supervisor, Dr. Peter H. Schuepp, without whom my dream for a Ph.D study would have been a fantasy. I am particularly grateful for his unique patience, guidance, editorial talents, moral and financial supports.

The assistance provided by Mr. Ian MacPherson and Matthew Bastian in the area of data transfers and processing is very much appreciated. I also wish to acknowledge the assistance and useful comments made by Dr. Ray Desjardins, who is a member of my Ph.D committee.

I would like to thank NASA for paying the publishing cost of one of the journal articles, and for providing the Landsat TM based land cover images. The efforts made by Guillaume Larocque, in classifying the videographic data are highly appreciated. My thanks go to Dr. Norman Bussiéres for his contribution to the Le Climat paper.

To my colleagues, Sam Kaharabata, Constance Mitic, Behzad Abarashi, Rob Pelltier and Zhi-Quing, thank you for the great time we had together.

The financial support from the Canadian Natural Science and Engineering Council, from Agriculture and Agri-Food Canada, Atmospheric Environment Service of Canada, and the Centre for Climate and Global Change Research (C^2GCR), McGill University, is very gratefully acknowledged.

Above all, I give the almighty GOD the gratitude for granting me the strength, good health and knowledge, to start and complete the Ph.D work.

TABLE OF CONTENTS

ABSTRACT	ii
RÉSUMÉ	v
PREFACE	viii
STATEMENT FROM THE THESIS OFFICE	ix
ADVANCEMENT TO SCHOLARLY KNOWLEDGE	x
1. Contribution to Knowledge	x
2. Research Papers in Refereed Scientific Journal	xi
CONTRIBUTION OF CO-AUTHORS TO MANUSCRIPTS	xii
ACKNOWLEDGMENTS	xiii
TABLE OF CONTENTS	xiv
LIST OF ACRONYM	xix
LIST OF SYMBOLS	xix
LIST OF TABLES	xxi
LIST OF FIGURES	xxiii
CHAPTER 1. GENERAL INTRODUCTION	1
1.1 Global Warming and Climate Change	1
1.2 The BOREAS Project	3
1.2.1 Objectives and measurement scales	3
1.2.2 The BOREAS study area	4
1.3 The Focus and Objectives of this Thesis	4
CHAPTER 2. FLUX MEASUREMENTS AND ANALYSIS TECHNIQUE - AN OVERVIEW	6
2.1 Chamber and Micrometeorological Techniques	6
2.2 Eddy Correlation Technique	7
2.3 Tower and Airborne Flux Measurements	8
2.4 Twin Otter Mission in BOREAS	9

2.4.1 Instrumentation 9
2.4.2 Flight Patterns 11
2.5 Analysis Techniques 12
2.5.1 Detrending- linear and non linear 12
2.5.2 Quadrant analysis 14

Link Statement to Chapters 3,4,5 18

CHAPTER 3. ANALYSIS OF FLUX MAPS VERSUS SURFACE CHARACTERISTICS FROM TWIN OTTER GRID FLIGHTS IN BOREAS 1994 19

3.1 Abstract 19
3.2 Introduction 19
3.3 Site Description 20
3.4 Flight Patterns and Data Collections 22
3.5 Weather Conditions and Stability 26
3.6 Flux Calculation, Detrending Procedure and Flux Mappings 26
3.7 Comparing Maps for Similarity and Persistence 28
3.8 Results and Discussions 29
3.8.1 Sensitivity of the detrending scheme 29
3.8.2 Representativeness of the fluxes 30
3.8.3 Maps of surface characteristics 31
3.8.4 Composite flux maps 32
3.8.5 Similarity between flux maps and persistence features 35
3.8.6 Flux correlation with surface characteristics 38
3.9 Conclusions 39

CONNECTING STATEMENT LINKING CHAPTER 3 AND 4 41

CHAPTER 4. COMPARISON OF THE SPATIAL AND TEMPORAL DISTRIBUTION OF

FLUXES OF SENSIBLE HEAT AND CO_2 FROM GRID FLIGHTS IN BOREAS 1994 AND 1996 42

4.1 Abstract 42
4.2 Introduction
4.3 Data Acquisition and Processing 43
4.3.1 Sites 43
4.3.2 Sampling and weather conditions 44
4.3.3 Data Processing 45
4.4 Results and Discussion 48
4.4.1 Grid average fluxes 50
4.4.2 Maps of surface characteristics 51
4.4.3 Flux maps 54
(a) Spatial distribution of fluxes 54
(b) Factors affecting flux variability 56
(c) Direct mesoscale fluxes 58
(d) Stability of flux estimates 59
(e) Effect of mapping scale on flux patterns 60
(f) Significance of the spatial variation 62
4.4.4 Energy partitioning 63
(a) Bowen ratio 63
(b) Surface energy balance closure 65
4.5 Conclusions 66

CONNECTING STATEMENT LINKING CHAPTER 4 AND 5 68

CHAPTER 5: CORRELATION BETWEEN LAND COVER TYPES AND AIRBORNE MEASUREMENTS OF LATENT HEAT, SENSIBLE HEAT AND CO_2 FLUXES AT THE TWIN OTTER GRID SITES IN BOREAS 69

5.1 Abstract 69
5.2 Introduction 69
5.3 Data Description 71
5.3.1 Land classification data 71
(a) Data sources and image projections 71
(b) Classification methods and cover classes 73
(c) Sources of error in the classifications 74
5.3.2 Aircraft-Based Data 74
5.4 Data Processing 75
5.5 Results and Discussion 77
5.5.1 Comparison Between the Classification 77
5.5.2 Footprint Function and Estimates 80
5.5.3 Choosing the most appropriate cover map 85
5.5.4 Regression Analysis : SSA grid 88
5.5.5 Evaluation of model estimates : SSA 90
5.5.6 Regression Analysis: NSA grid 96
5.5.7 Evaluation of model estimates : NSA 97
5.6 CONCLUSIONS 102
GENERAL CONCLUSIONS 104
REFRENCES 106

APPENDIX 119
COMPARISON OF AIRBORNE AND SATELLITE DERIVED MAPS OF HEAT AND MOISTURE FLUXES OVER A BOREAL FOREST ECOSYSTEM 120

I. Abstract 120
II. Introduction 120
III. Description of the Study Area 121
IV. Data Collection and Processing 122
V. Results and Discussions 123

(i) The surface minus air temperature (T_s-T_a) 123
(ii) Maps of sensible and latent heat fluxes from airborne observations 127
(iii) Comparison of aircraft and satellite derived flux estimates 128
(iv) Factors affecting the variability of aircraft measured sensible and latent heat fluxes 129
VI Conclusion 133
References 134

LIST OF ACRONYMS

agl	above ground level
BR	Bowen ratio
BOREAS	Boreal Ecosystem Atmosphere Study
CGR	Counter Gradient fluxes
F_{ml}	Mesoscale flux along the flight line
F_{mg}	Mesoscale flux averaged over a grid
FT	Fourier series truncated at the fifth term
GI	Greenness index
GR	Gradient fluxes
LD	Linear detrending
NIR	Near-infrared radiation
NSA	Northern Study Area
OBS	Old black spruce
OJP	Old jack pine
R	Reflected red
SR	Simple ratio
SSA	Southern Study Area
ST	Fourier series truncated at the second term
TO	Twin Otter
TT	Fourier series truncated at the third term
YJP	Young jack pine

LIST OF SYMBOLS

H	[W m^{-2}]	Sensible heat flux density
k		Ratio of ground flux to net radiation
LE	[W m^{-2}]	Latent heat flux density
β		Bowen ratio

C	[mg $m^{-2}s^{-1}$]	CO_2 flux density
G	[W m^{-2}]	Sum of the minor energy balance terms (ground flux and storage)
q	[g kg^{-1}]	Moisture mixing ratio
Δq	[g kg^{-1}]	Change in moisture mixing ratio
q_*	[g kg^{-1}]	Humidity time scale
R↑	[W m^{-2}]	Incident solar radiation
R↓	[W m^{-2}]	Reflected solar radiation
R_n	[W m^{-2}]	Net radiation
T_a	[°C]	Air temperature
θ	[°K]	Potential temperature
$\Delta\theta$	[°K]	Change in potential temperature
θ_*	[°K]	Temperature time scale
t_*	[s]	Convection time scale
T_s	[°C]	Radiative surface temperature
u_*	[m s^{-1}]	Friction velocity
V_c		Coefficient of variation of CO_2 flux
V_h		Coefficient of variation of sensible heat flux
V_l		Coefficient of variation of latent heat flux
Vr		Coefficient of variation of the incoming radiation
w_*	[m s^{-1}]	Convective velocity scale
ΔT	[°C]	Surface temperature excess over air temperature, T_s-T_a
z	[m]	Aircraft measurement height
z_i	[m]	Mixed layer depth
Δz_i	[m]	Change in mixed layer depth

LIST OF TABLES

Table 3.1	Relative Proportion of Different Land Types at the Northern and Southern Study Twin Otter Grids.	23
Table 3.2	Twin Otter Grid Flight Summary of 1994 BOREAS Field Campaigns	24
Table 3.3	Correlation Coefficient (R) and Similarity Coefficient (C_s) of fluxes at SSA and NSA Grid Sites	37
Table 3.4	Correlation Coefficient between GI and C, C and LE, ΔT and H, and between C and H	38
Table 4.1	Twin Otter grid flight summary	45
Table 4.2a	Northern study area grid average parameters	47
Table 4.2b	Southern study area grid average parameters	47
Table 4.3	Boundary layer parameters	51
Table 4.4	Summary of the flux maps produced from 1 km (X), 2 km (Y) and 2 km with 1 km overlapping windows (Z)	62
Table 4.5	Correlation coefficient (r) and coefficient of similarity (C_s) between X,Y and Z	62
Table 5.1	Description of cover classes based on TE-1 classification	81
Table 5.2	Description of cover classes based on TE-2 classification	83

Table 5.3	Description of cover classes based on RSS	83
Table 5.4	SSA grid flight conditions and footprint estimates.	89
Table 5.5	Description of the Candle Lake segments from west to east	91
Table 5.6	Fraction of cover types within the aircraft footprint, calculated for the Candle Lake segments	92
Table 5.7	NSA grid flight conditions and the associated footprint parameters.	96
Table 5.8	Coordinates for the segments along the old black spruce run	97
Table 5.9	Fraction of cover types within the flux footprint of the black spruce run segments	98
Table 5.10	Coordinates for the segments along the burn run	98
Table 5.11	Fraction of cover types within the flux footprint of the burn run segments	99

LIST OF FIGURES

Figure 2.1 The Canadian Twin Otter aircraft as instrumented for BOREAS 10

Figure 2.2 Flight track plot for site-specific runs flown on 29 July 1994 13

Figure 2.3 Illustrations of (a) linear and non-linear detrending based on a Fourier series truncated at the (b) second term, (b) third term and (d) fifth term. 15

Figure 2.4 Illustrations of the application of hyperbolic holes with k varying from 0 to 2.5 for flux distribution of sensible heat and CO_2 . 17

Figure 3.1 Land classification imagery of the NSA (a) and SSA (b) Twin Otter grid sites. The location of tower sites is indicated. 21

Figure 3.2 North-South oriented flight trajectories for Twin Otter grid flights in the NSA(a) and SSA (b). 25

Figure 3.3 h-scatter plot of latent heat (LE); LE(S) is the value of LE at location S and LE(S+h) is the value of the next grid point along the flight line. 30

Figure 3.4 Composite maps of Greenness index (GI) and CO_2 flux (C) for the NSA grid, for the three IFCs. 32

Figure 3.5 Composite maps of surface temperature excess $\Delta T(^{\circ}C)$ and sensible heat flux (H) for the NSA grid, for the three IFCs. 33

Figure 3.6 Average maps (over all three IFCs) of surface characteristics, fluxes (H and C) and BR for the NSA grid. 35

Figure 3.7 Average maps of surface characteristics, fluxes (H and C) and BR for the SSA grid. 36

Figure 3.8 3.8. Persistence maps for H, LE and C for the NSA and SSA grids. 37

Figure 3.9 Correlation between GI and C. C and LE. and ΔT(°C) and H, for IFC-1. 39

Figure 4.1 Plots of the grid averaged fluxes of (a) sensible heat, (b) latent heat and (c) CO_2. 50

Figure 4.2 Maps of surface minus air temperature, ΔT(°C) and greenness index (GI) at the NSA grid in 1994 and 1996 52

Figure 4.3 Maps of ΔT(°C) and GI at the SSA grid in 1994 and 1996 53

Figure 4.4 Maps of CO_2 flux (C) (mg m^{-2} s^{-1}), sensible heat flux (H) (W m^{-2}), and latent heat flux (LE) (W m^{-2}) at the NSA in 1994 and 1996 55

Figure 4.5. Maps of C, H and LE at the SSA in 1994 and 1996. 56

Figure 4.6 The plots of the ratio of V_f/V_r against V_r 58

Figure 4.7 Maps of (a) H, (b) C and (c) LE produced from perturbed gridded 1994 NSA data 61

Figure 4.8 Maps of Bowen ratio (β) for the NSA and SSA in 1994 and 1996 64

Figure 5.1 Cover maps for the NSA based on (a) TE-1, (b)TE-2, (c)RSS and (d) VDD classifications 78

Figure 5.2	Cover maps for the SSA based on (a) TE-1, (b)TE-2, (c)RSS and (d) VDD classifications	79
Figure 5.3	(a) Footprint function for specified values of z_o and (b) the corresponding cumulative footprint	84
Figur 5.4	Ratio of the proportion of the cover types within the footprint to the grid average value	84
Figure 5.5	Maps showing abundance of (a) regeneration or shrub, (b) conifer (wet) or spruce and (c) conifer (dry) or pine.	86
Figure 5.6	Species composition maps for the SSA grid along showing the (a) regeneration, (b) conifer (wet) or spruce, and (b) fen classes	87
Figure 5.7	Flight trajectory of the Candle lake run	93
Figure 5.8	Comparison of the observed CO_2 fluxes along the Candle Lake segments to the predicted estimates	94
Figure 5.9	Comparison of the observed latent heat fluxes along the Candle Lake segments to the predicted estimates	95
Figure 5.10	Comparison of the observed sensible heat fluxes along the Candle Lake segments to the predicted estimates	95
Figure 5.11	Plots of the observed against the regression model estimates of (a)CO_2, (b) sensible heat, and (c) latent heat fluxes, for the black spruce run	100

Figure 5.12 Plots of the observed against the regression model estimates of (a)CO_2, (b) sensible heat, and (c) latent heat fluxes, for the burn run 101

CHAPTER 1

GENERAL INTRODUCTION

1.1 Global Warming and Climate Change

Has climate change already begun? While no answer can be provided to this question with absolute certainty, there are indications that the earth is warming up and is causing a change in the global climate. Global records of surface temperature over the last 100 years show a rise in global temperatures of about 0.5 °C overall [*Houghton et al.*, 1996]. For the last 15 to 20 years, there has been fairly steady rise in temperatures, giving some assurance that we are now in a global warming phase [*NASA*,1996]. Early this year NASA and the National Oceanic and Atmospheric Administration (NOAA) announced that 1998 was the hottest year on record (1.2 degrees hotter than normal), and that the 1990s will go down as the hottest decade on record, regardless of the final temperature record of 1999. It is now believed that the observed global warming trend is larger than the trends models indicate could be due to natural variability.

Changes in natural modes of the atmospheric circulation have been documented and may be linked to anthropogenic climate change. In particular, the North Atlantic Oscillation (NAO), the Pacific-North American (PNA) teleconnection pattern, and El Niño-Southern Oscillation (ENSO) combine to influence the planetary wave structure over the Northern Hemisphere such that most temperature changes in recent years have been of warming over North America and Eurasia but cooling over the northern oceans [*NASA*,1996]. At the surface, the heat capacity of the underlying surface has a major influence in amplifying changes over land while moderating changes over the ocean, so that global warming is enhanced.

Anthropogenic influence on global warming was first recognized by a Swedish chemist, Svante Arrhenius, in 1896, when at the onset of industrial revolution he observed that carbon dioxide (CO_2) concentration in the atmosphere was increasing, and would continue to increase with the growing global consumption of fossil fuels, particularly coal. From his knowledge of the role of CO_2 in atmospheric heating, he predicted the earth would

become several degrees warmer if atmospheric CO_2 doubled. The increase in atmospheric CO_2 is now well documented, with the likelihood that it will double by the middle of the next century from the levels at the time of Arrhenius [*NASA*, 1996a]. In the period 1750-1992 (and especially since the 1960s), the atmospheric concentrations of the greenhouse gases (GHG's) - CO_2, NH_4 and N_2O- have grown by about 30%, 145% and 15%, respectively [*Houghton et al.*, 1996]. In the global carbon budget the Intergovernmental Panel on Climate change [*IPCC*, 1990] indicated an imbalance of about 1.6 Gt C yr^{-1}, i.e., "a missing sink," in the global carbon budget, even though the carbon sink to the ocean (2.0 Gt C yr^{-1}) was taken into consideration. It was suggested four years later by *IPCC* [1995] that up to 1.6 Gt C yr^{-1} might be sequestered in terrestrial ecosystems, particularly in the northern hemisphere.

It has been hypothesized that terrestrial uptake of atmospheric CO_2 occurs in forest ecosystems, in temperate and boreal forests in the northern hemisphere [e.g. *Tans et al.*, 1990]. Climate models predict that the boreal forest is likely to experience a significant change in climate [*Manabe and Stouffer*, 1980], and ecosystem models predict that potential climate change may cause a shift in the composition and structure of the boreal forest [*Sykes* and *Prentice*, 1995; *Hogg and Hurdle*, 1995]. The boreal forest's potential to affect the Earth's climate arises from its great areal extent (11% of the terrestrial surface according to *Bonan and Shugart*, 1989), and its unique biophysical properties. The dominant vegetation classes in this region, evergreen conifer forests, have a greater ability to exchange mass and energy with the atmosphere than other vegetation types [*Shuttleworth*, 1989; *Kelliher et al.*, 1993].

Current studies to explore the sensitivity of the climate system to surface processes are based on very sketchy assumptions about the vegetated land surfaces. Further investigation of the role of the boreal forest as a carbon sink and its impact on the global climate change requires measurements on a multiscale of the biological and physical characteristics of the boreal ecosystem, and formulation and validation of models capable of reproducing the exchange processes that occur between the ecosystem and the atmosphere. These scientific tasks constituted the major drive for the design and execution of the Boreal Ecosystem Atmosphere Study (BOREAS).

1.2 The BOREAS Project

1.2.1 Objectives and measurement scales

BOREAS was an international scientific effort to understand the interactions of the land surface with the atmosphere [*NASA*, 1995]. It was designed to extend the findings of the First ISLSCP intensive Field Experiment (FIFE) over a tall grass prairie to the more complex boreal forest [*AGU*, 1992]. The main objectives were: (1) improving our understanding of the processes which govern the exchange of energy, water, heat and carbon and trace gases between the boreal forest ecosystems and the atmosphere, with particular reference to those that may be sensitive to global change; and (2) developing methods for applying the process models over large spatial scales using remote sensing and other integrative modeling tools. In particular, BOREAS addresses three major scientific issues: (a) the biogeochemical functioning of the boreal forest, including controls on carbon storage and partitioning and the seasonal and spatial variability of trace gas fluxes; (b) the sensitivity of the boreal forest biome to changes in the physical climate system; (c) the biophysical feedback to the climate system due to ecological changes in the functioning of the biome.

To achieve these objectives, a multiscale approach to data acquisition was adopted. The largest spatial domain (an area approximately 100 km x 100 km) was for meteorological and satellite data acquisition and large scale modeling. Another scale of investigation was set at 50 km x 50 km which corresponds to the two BOREAS study areas. These study areas were small enough to be characterized by surface and aircraft measurements, yet large enough to test scaling hypotheses using models and remote sensing imagery. Within each study area, water vapour, heat, and CO_2 fluxes were measured at the local scale (about 1 km), using eddy correlation equipment mounted on towers which were located in patches of relatively homogeneous vegetation and soils. To complement the tower flux sites, 70 auxiliary sites (100 m x 100 m) were selected. Within these sites, which were stratified by species type, productivity, and age, biometry and optical techniques were used to measure biomass density, leaf area index, net primary productivity, litter fall, etc.

1.2.2 The BOREAS study areas

The field experiments were conducted at two sites, the Northern Study Area (NSA) and Southern Study Area (SSA). These study areas were placed near the northern and southern ecotones of the biome in order to study important processes associated with the controlling factors (temperature in the north, moisture in the south) which are most likely to undergo significant changes within the biome as a whole [*Sellers et al.*. 1997].

The NSA was located 45 km west of Thomson, Manitoba, and close to the northern limit of the closed-crown boreal forest. The predominant species is black spruce which occurs in stands of varying density. There are some jack pine stands mainly in the southern part of the site, and trembling aspen which are scattered within some of the coniferous stands. Stands and uniform patches are small, and no logging or recent burn since 1981 have occurred in the area. The terrain is flat and broadly rolling in low regions and hilly in high areas. The soils consist of clays, organics and some sandy deposits, with depths that vary from bare rock outcrops on the top of hills to deep sedimentation basins in the low areas up to 17 m in depth. Variations in moisture regimes occur due to topography or soil changes. Being generally flat and having abundant wetlands area, the drainage of much of the site is poor. Bogs and fen occur on most of the low-lying terrain.

The SSA was located near Prince Albert, Saskatchewan. The site is near the southern limit of the boreal forest. There are large patches of aspen and, to a lesser extent, jack pine and black spruce and patches of uniform inhomogeneity. Forest cover is often controlled by small changes in relief and soil/soil drainage. Aspen occurs on the upland, jack pine on minor ridges and black spruce in the lower poorly drained sites. In the poorly drained areas throughout the study area, bogs support black spruce with some tamarack. The fen areas are composed mostly of sedge vegetation with discontinuous cover of tamarack or swamp birch.

1.3 The Focus and Objectives of the Thesis

Airborne measurements of surface fluxes of latent heat, sensible heat, and CO_2, were a significant part of BOREAS 1994 and 1996. The measurements involved the use of four airplanes, viz. The Long-EZ from the US National Oceanic and Atmospheric Administration (NOAA/ATDD), the Twin Otter from the Canadian National Research Council, the King Air

from the University of Wyoming, and the Electra from the U.S. National Center for Atmospheric Research (NCAR). The focus of this thesis is on the analysis of the flux data that were acquired by the Twin Otter (TO). The TO was flown in different patterns and at different locations in the study areas (see chapter 2). Most of the data used in this thesis were obtained when the aircraft was flown in a grid pattern over a 16 km x 16 km site in both study areas.

The goals and objectives of this thesis are tailored to be in agreement with those of BOREAS. The main goal is to analyse the acquired aircraft data in such a way that results can be used to upgrade regional scale models and to improve methods to estimate regional scale surface fluxes of sensible heat, latent heat and CO_2. This goal is approached by a number of technical objectives: (a) to address averaging procedures relevant to low level flights over heterogeneous surfaces as found in BOREAS; (b) to assess the significance of surface induced mesoscale motions at the grid sites; (c) to map latent heat flux, sensible heat flux and CO_2 flux over two 16 km x 16 km grid sites at the Northern (NSA) and Southern (SSA) Study Areas of BOREAS; (d) to analyse the flux maps in order to investigate the sources and sinks for the scalars and the role of the boundary layer structures in the transfers of these scalars; (f) to relate the scalar fluxes to spectrally derived surface characteristics, such as greenness and radiometric surface temperature; (g) to explore the relationship between fluxes and land cover types, and to determine the degree to which flux estimates could be predicted from the knowledge of the cover fractions within the flux footprint.

CHAPTER 2

FLUX MEASUREMENTS AND ANALYSIS TECHNIQUES - AN OVERVIEW

2.1 Chamber and Micrometeorological Techniques

The dynamic interactions between the surface and the planetary boundary layer involve exchanges of mass, moisture, momentum and trace gases. To assess accurately the possible causes and potential effects of increasing atmospheric trace gas concentration requires a quantitative understanding of the surface fluxes of these gases. The flux of these scalars (quantity of the scalars transported per unit area per time) is related to the height above the surface. Close to the surface, wind shear and buoyancy forces create turbulent conditions, whereby vertical transport of scalars is enhanced by irregular or random motions. Measuring these fluxes is of great importance in studying sources, sinks and transformation of the scalars.

Several methods can be used to measure fluxes and they vary in both spatial and temporal sampling aspects. The methods used in BOREAS included chambers [e.g. *Lawrence et al.*, 1997; *Middletown et al.*, 1997; *Salvage et al.*, 1997] and micro-meteorological techniques [e.g. *Desjardins, et al.*, 1997; *Baldocchi et al.*, 1997]. Chambers may vary in volume from those that measure the gas exchange for individual leaves ($\approx 10^{-5}$ m^3) to those that monitor an entire soil/plant canopy system ($< 10^3$ m^3). Chamber measurements are usually non-continuous and subject to several problems, including alteration of temperature, radiation, and wind conditions inside the chamber relative to those outside [*Monteith*, 1990; *Leuning and Foster*, 1990]. This may result in nonrepresentative measurements. Despite these limitations, chambers can be useful for making replicated measurements in small plots.

The literature is replete with micro-meteorological techniques that are now available for measuring fluxes in the surface layer [*Brutsaert*, 1982; *Stull*, 1988; *Wyngaard*, 1990, 1991; *Garratt*, 1992; *Kaimal* and *Finnigan*, 1992, Lenschow, 1995]. These techniques estimate fluxes based on measurements of atmospheric elements above the surface. They can be classified into direct and indirect methods. The former include eddy correlation and

eddy accumulation techniques, and derive a flux estimate directly from observation of the wind and concentration (or temperature) fields. The indirect methods generally require some empirically determined relationship to estimate the flux. Among these are Bowen ratio and gradient methods, which estimate flux from the concentration at two or more levels. Unlike chamber methods, these micro-meteorological techniques do not modify the surface micro-environmental conditions and provide a spatially and temporally integrated measurement. They may, however, be unreliable at selected times of the day, especially under low-turbulence conditions [*Verma and Rosenberg*, 1975], and profile methods cannot be used in situations such as within forest canopies [*Denmead and Bradley*, 1985]. Since the eddy correlation method is used in this study, it is described in more detail below.

2.2 Eddy Covariance Technique.

The vertical density flux of a constituent scalar is given by the average of the instantaneous product of the concentration ρ_c of the scalar and the vertical velocity w, where

$$F_c = \overline{w\rho_c} = \overline{w'\rho_c'} + \overline{w}\,\overline{\rho_c} \qquad (2.1)$$

w' and ρ_c' are the fluctuations from the average $\overline{w}$ and $\overline{\rho_c}$, respectively (Reynolds averaging). The eddy covariance technique is based on the assumption that, $\overline{w}\,\overline{\rho_c}=0$, so that $F=\overline{w'\rho_c'}$, i.e. the flux of the transported scalar at the given point in the atmosphere is obtained from correlation of these two fluctuations. *Webb et al.* [1980] demonstrated how the fluxes of sensible heat and water vapour affect the flux estimate of a trace species, and developed correction terms which must be used with Eq. 2.1 to obtain the total vertical flux of the trace constituent, i.e.

$$F_c = \overline{w'c'} + a\frac{\overline{\rho_c}}{\overline{\rho_a}}\overline{w'\rho_v'} + \overline{\rho_c}\left(1+a\frac{\overline{\rho_v}}{\overline{\rho_a}}\right)\frac{\overline{w'T'}}{\overline{T}} \qquad (2.2)$$

where $\overline{w'\rho_v'}$ and $\overline{w'T'}$ are the measured fluxes of water vapour density and temperature, $a=m_a/m_v$ is the ratio of the molecular weight of dry air to that of water vapour, ρ_a is the dry

air density. The correction terms are particularly important in cases with small value of $w'\rho_c'/\rho_c'$

Webb et al. (1980) also showed that no correction to the flux is necessary if the mixing ratio of the constituent with respect to dry air ($c=\rho_c/\rho_d$) is measured instead of its constituent density, i.e,

$$F_c = \overline{\rho}\,\overline{w'c'} \qquad (2.3)$$

The advantages of the eddy correlation method are: (1) turbulent diffusive fluxes can be measured directly across a near-horizontal plane above the surface without intruding upon or disturbing the surface being monitored; (2) it inherently averages over a surface area that increases with height of the measurement above the surface and - in the case of airborne observations - with length of the flight leg; (3) it is particularly useful in situations where counter-gradient flux (or zero gradient flux) must be expected. Eddy correlation is the most direct flux-measuring technique, but it requires fast-response trace gas and vertical velocity fluctuation measurements at approximately coincident points in space over the entire frequency spectrum of the irregular fluctuations that contribute to the flux. In spite of this, it has become the dominant flux measuring technique in the last 10 years due to increasing availability of fast-response sensors. In all the analyses covered by this thesis, fluxes are estimated based on Eq. 2.3.

2.3 Tower and Airborne Flux Measurements

Eddy correlation flux measurements can be made from either fixed or moving sensors. The choice between a fixed point (tower) and moving platform (aircraft) is determined by a host of factors, some of which are accessibility of site, nature of surface, fetch requirement, spatial coverage and duration of measurements. Where measurements are desired for a long duration and limited spatial extent over an area that is relatively homogeneous, tower platforms are preferred. Airborne platforms allow measurements over inaccessible areas and offer advantages where the objective is to integrate gas exchanges

over extended, heterogeneous surfaces. Some large-scale experiments, such as HAPEX MOBILHY [*André et al.*, 1988], the First International Satellite Land Surface Climatology Project Field Experiment (FIFE) [*Sellers et al.*, 1992], the Northern Wetland Study (NOWES) [*Glooschenko et al.*, 1994], the California Ozone Deposition Experiment (CODE) [*Pederson et al.*, 1995], enabled comparison between these two methods, with comparable results over relatively homogeneous areas [*Grossman*, 1992; *Desjardins. et al.*, 1992, 1997; *MacPherson et al.*, 1999].

The level of agreement between the methods is related to how the sampling requirements are met, and the extent to which the errors associated with the flux measurements are accounted for. The most commonly observed problems and errors in flux measurements are given by *Mann* and *Lenschow* [1994], *Lenschow* [1995] and *Mahrt* [1998]. For towers they include: (a) contamination of vertical flux through the distortion of flow around the sensors and supporting structures; (b) potential small-scale loss when measuring close to the surface; (c) inability to capture effects of stationary eddies or stationary updrafts; (d) small footprint or systematic bias due to location; (e) elongation of eddies in the downwind direction and formation of role vortices. For aircraft they include: (a) possible vertical flux divergence due to advection or storage between the surface and the flight level; (b) loss of long wavelength flux contribution due to inadequate sampling length; (c) higher likelihood for flux contamination from changes in height during flight.

2.4 Twin Otter Missions in BOREAS

2.4.1 Instrumentation

The Canadian Twin Otter aircraft as instrumented for BOREAS is shown in Figure 2.1. The aircraft carried a Trimble Model TNL-7880SR GPS/VLF/Omega navigation system, which was used for flying specific tracks and for recording aircraft position. The system was operated in the GPS mode throughout BOREAS, and position and velocity data were recorded at 16 Hz. Air motion relative to the aircraft was measured by a nose-mounted gust boom incorporating a Rosemount 858AJ28 5-hole probe. This device and the associated pressure transducers measure static pressure (altitude), dynamic pressure (airspeed) and the angles of attack and sideslip. A second altitude/airspeed system employs a separate set of

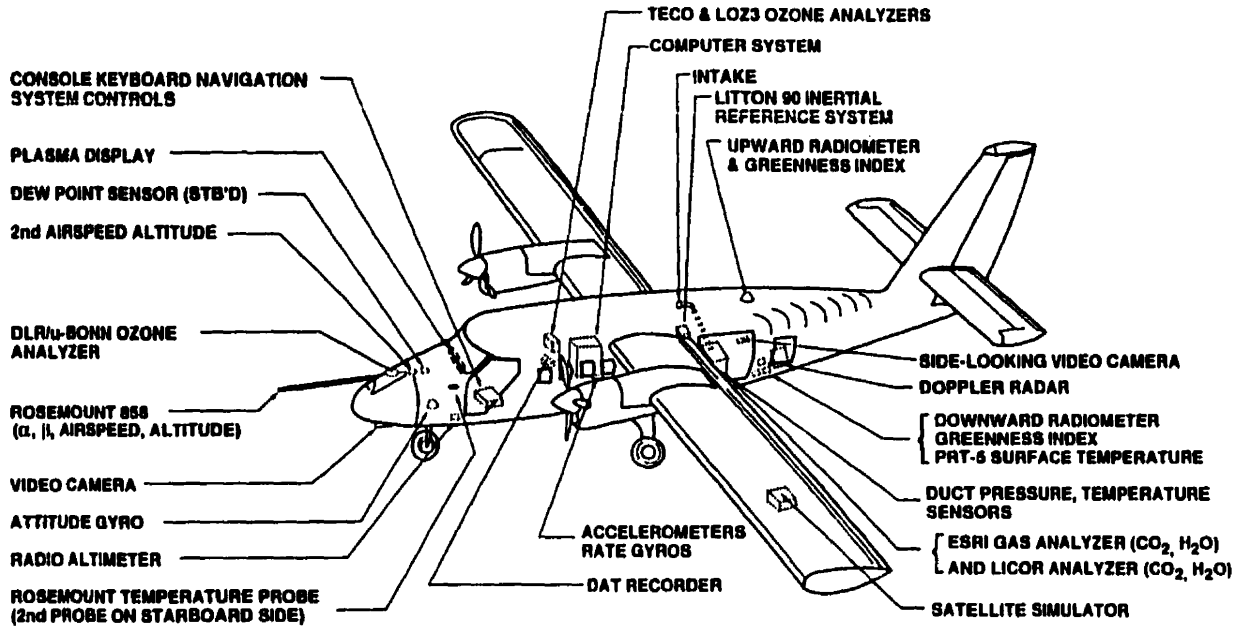

Figure 2.1 NRC Twin Otter atmospheric research aircraft as instrumented for BOREAS

pressure transducers connected to the fuselage-mounted pitot and static ports. Inertial velocity was measured by Litton LTN-90/100 inertial reference system. Air temperature measurement was made by a Rosemount fast response 102DJ1CG heated probe mounted on the port side of the aircraft nose. Carbon dioxide and water vapour concentration were measured by infrared gas analyzer developed by Agriculture Canada (ESRI) and by LI-6262 CO_2/H_2O analyzer developed by LICOR. The devices were mounted in the rear rack of the aircraft, with their sample air drawn from a duct, which was also instrumented for the measurement of the airspeed, temperature and density of the sampled air, in order to calculate the instantaneous CO_2 and H_2O mixing ratios.

The incident solar radiation (R↓) was measured with a Kipp and Zonen CM-11 pyranometer with a 305-2800 nm spectral range. This device was mounted on the aft fuselage of the aircraft. Reflected solar radiation (R↑) was measured by an Eppley pyranometer. The aircraft carried both an upward-and downward-looking Skye Industries Vegetation Greenness Indicator, which measures a ratio of near-infrared (730 nm) to red (660 nm) radiation. Surface temperature was measured by a downward-looking Barnes PRT-5 infrared radiometer. Net radiation was calculated using incident and reflected solar radiation (R↓ and R↑), with longwave contributions derived from PRT-5 surface temperature (T_s in deg K) and air temperature (T_a in deg K) in the following equation:

$$R_n = R\downarrow - R\uparrow + (1.20\sigma T_a^4 - 171.0) - (0.98\sigma T_s^4)$$

where the last two terms represent the incident and reflected longwave [*Swinbank*, 1963] components, using the Stefan-Boltzmann Constant $\sigma = 5.6924 \times 10^{-8}$ $Wm^{-2}°K^{-4}$ and a surface emissivity of 0.98.

2.4.2 Flight Patterns

The principal role of the Twin Otter in BOREAS was to make low-altitude (≈ 30 m agl) flux measurements for use in scaling up fluxes from tower scales to the regional scales observable by satellite. The flight patterns flown included site specific runs, grid pattern, L pattern, Candle Lake run, agricultural run, transect, soundings and intercomparison runs.

Most of the data used in this study are from the grid pattern flights, which are discussed in subsequent chapters. The Candle Lake run is explained in Chapter 5, where data from the run are used to validate regression models. The smallest-scale 'site-specific' runs were chosen to sample, as much as practicable, a single type vegetation. Figure 2.2 shows the flight track plot for site-specific runs flown on 29-July 1994. Most of the runs were made to pass within about 100 m of one of the main BOREAS flux towers. In the SSA, site specific runs were made past the towers at Old Aspen(OA), Old Black Spruce (OBS), Old Jack Pine (OJP) and Fen. In the NSA, similar runs were made at OBS, OJP and Young Jack pine (YJP). Since much of the NSA was dominated by regenerating, burned-over areas, an additional site specific run was flown over it, although it had no flux tower.

The runs varied in length from 3 km to 14 km. The shorter runs were usually repeated up to 10 times to improve the statistical reliability of flux estimates. The Fen and YJP were also flown at slightly lower altitude than other runs to reduce the flux footprint. The longer runs were typically flown 4 to 6 times on a given flight. Data from the OBS runs at the NSA are used in Chapters 4 and 5 to test stability of flux maps and regression models.

2.5. Analysis Techniques

2.5.1.Detrending - linear and non-linear

The eddy covariance method directly samples air parcels to obtain the flux estimate from the time-averaged covariance between excursions in vertical wind (w') and scalars (ρ'). This means that the definition of the mean (and of the effective sampling period or distance over which the mean is determined) is of crucial importance to the flux estimate. Problems arise when the data contain trends or contributions to the variance from long wavelength fluctuations. If a trend is retained, it may bias the flux estimate with a poorly defined contribution from a single (long) wavelength. Transport on intermediate wavelength (slightly shorter than the length of the flux run) can also lead to poor flux estimates because of the small number of samples at those wavelength for a given run. This problem is usually tackled by filtering or detrending. High-pass filtering the data before estimating the covariance will eliminate the mean, any linear trend, and all long-wavelength fluctuations below the cutoff wavelength of the filter, while detrending the data removes the mean and linear trend but

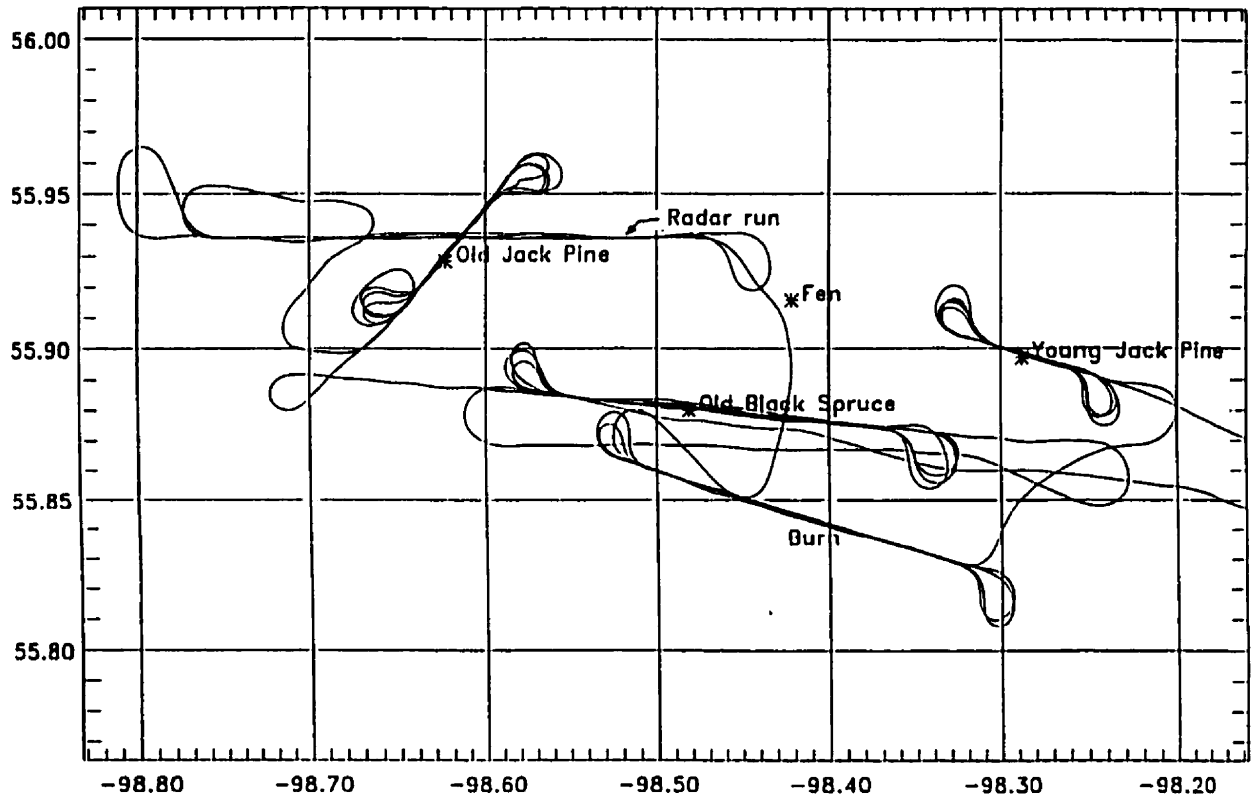

Figure 2.2: Flight track plot for site-specific runs flown on 29 July 1994

retains all long-wavelength fluctuations less than the length of the run. Studies by *Grossman* [1992], *Kelly et al.* [1992], *Desjardins, et al.* [1992], *Betts et al.* [1992] compared filtered fluxes to detrended fluxes; they all reported that filtered fluxes were 10 to 30 % lower than detrended fluxes.

Before applying detrending on any data set it is important to determine its effect on the flux estimates. Linear detrending may be considered adequate for many homogeneous areas, but can be inadequate in situations where the mean concentration of the scalar property (e.g. water vapour) changes non-linearly along the run. On the other hand, non-linear detrending represents a high-pass filtering technique whose effects on the magnitude of the flux estimate cannot be deduced *a priori*. Figure 2.3 illustrates linear and non-linear detrending based on a Fourier series truncated at the second term, third term and fifth term.

Since no formal rules or guidelines existed for testing detrending procedures for optimum estimates, other than the traditional visual inspection of the scalar traces, the development of an objective scheme for choosing detrending procedures was one of the objectives of this thesis. It is addressed in Chapter 3. The basis for the scheme is rooted in quadrant analysis of turbulent fluxes, which will be briefly discussed.

2.5.2 Quadrant analysis.

Quadrant analysis [*Antonia et al.*, 1981; *Raupach*, 1981; *Shaw*, 1985], has been widely used to reveal the structure of turbulent transfer of momentum and scalars in and above vegetation canopies. It represents the instantaneous flux events in Cartesian coordinates, with scalar excursion ρ' on the abscissa and w' on the ordinate, so that each quadrant is defined according to the sign of the two fluctuating components involved in the transport. The four quadrants can be given as

$$Q_1 = quadrant\ 1 : \rho>0,\ w>0 \quad excess\ up$$
$$Q_2 = quadrant\ 2 : \rho<0,\ w>0 \quad deficit\ up$$
$$Q_3 = quadrant\ 3 : \rho<0,\ w<0 \quad deficit\ down$$
$$Q_4 = quadrant\ 4 : \rho>0,\ w<0 \quad excess\ down$$

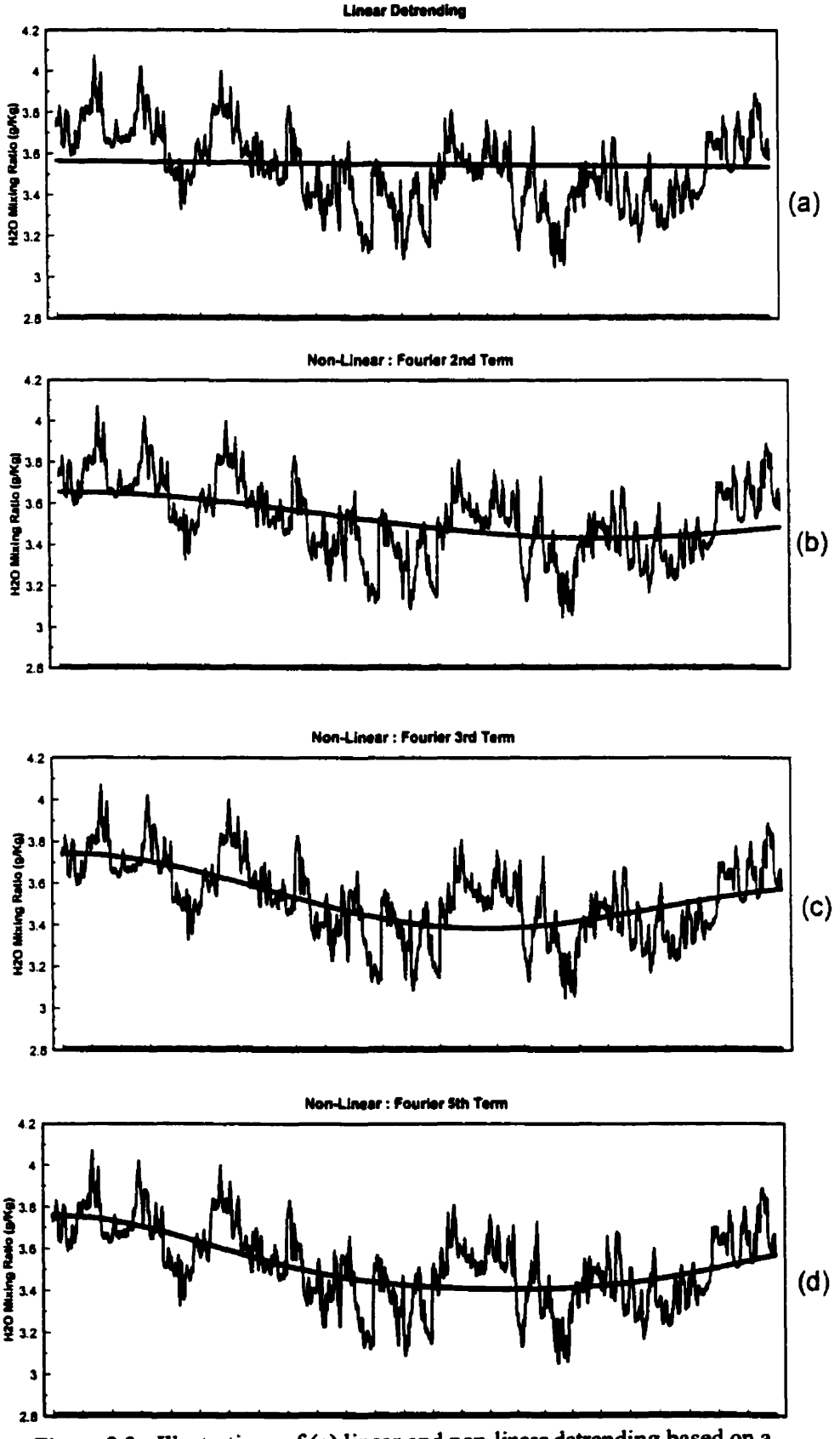

Figure 2.3 : Illustrations of (a) linear and non-linear detrending based on a Fourier series truncated at the (b) second term, (c) third term and (d) fifth term

The imposition of a threshold on the flux events (ρ'w' pair) corresponds to the elimination of points within a hyperbolic hole in the scatter plot, the size of which can be expressed in terms of mean flux [*Grant et al.*, 1986] or standard deviation of the fluxes [*Lenschow and Stephens*, 1980; *Caramori et al.*, 1994]. Using the latter definition, the hyperbolic hole of size H is given as $H = k\sigma_{w'\rho'}$, where *k* is a constant and $\sigma_{w'\rho'}$ is the standard deviation of the flux. Figure 2.4 illustrates the application of hyperbolic holes with k varying from 0 to 1.0 for flux distributions of sensible heat and CO_2. Under unstable atmospheric stability conditions, the bulk of scalar transport takes place in the gradient quadrants (Q_1 and Q_3 for heat and moisture; Q_2 and Q_4 for CO_2), while relatively small transport occurs in the counter-gradient quadrants (Q_2 and Q_4 for heat and moisture; Q_1 and Q_3 for CO_2). Fluxes in the gradient quadrants are termed gradient (**GR**) fluxes, while fluxes in the counter gradient quadrant are termed counter gradient (**CGR**) fluxes. The relative importance of turbulent motion in the transport of scalars can be examined by calculating the ratios of the flux fractions F_i for the various quadrants i. The ratios, F_3/F_1, $(F_3+F_1)/(F_2 + F_4)$ were used by *Coppin et al.* [1986], *Gao et al* . [1989], *Bergström and Högstrom* [1989], *Maitani* and *Shaw* [1990] and *Lee* and *Black* [1992] to describe sensible heat and latent heat transfer mechanisms and their source distributions. By plotting the ratios at different heights above plant canopies against hyperbolic hole size they were able to show that the transfers of momentum and sensible heat (or latent heat) are dissimilar. They also showed that unlike the ratio F_3/F_1, which may be greater or smaller than 1, the ratio $(F_3+F_1)/(F_2+ F_4)$ or GR/CGR increases with increasing hyperbolic hole size and is greater than 1, irrespective of the height above the plant canopies. This observed fact that the values of the ratio GR/CGR consistently increases with increasing hole size, is in agreement with the physically reasonable assumption that the strongest contributions to transfer are from the gradient modes (such as excess-up or deficit down for heat and moisture, etc.), suggesting that the appropriateness of any detrending method can be determined by this approach. (For details see section 3.6).

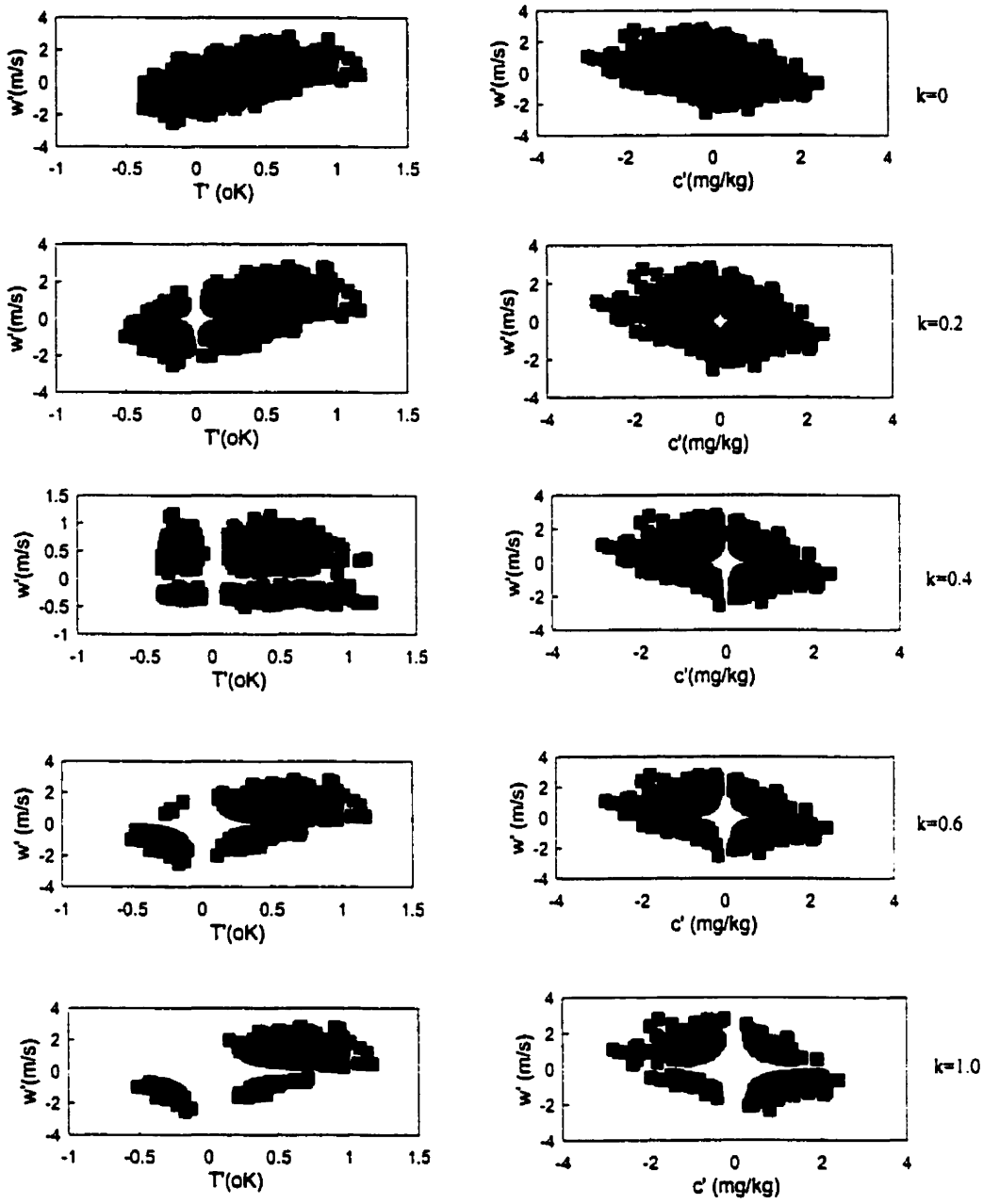

Figure 2.4: Illustration of the application of hyperbolic holes with k varying from 0 to 1.0 for flux distribution of sensible heat and CO2

Link statement to Chapters 3,4 and 5.

The following chapters present detailed analyses relating to the objectives outlined above. The material presented in Chapter 3 has been published in the Journal of Geophysical Research [*Ogunjemiyo et al.*, 1997] and results in graphical form are available in the NASA BOREAS data archives (*ftp://boreas_pre@boreas.gsfc.nasa.gov/data/afm/afm04/*). Although some basic concepts, like quadrant analysis, have already been introduced in Chapter 2, Chapter 3 is presented with a full description of analysis procedures, so that it can be read as a separate unit by the potential user.

CHAPTER 3

Analysis of Flux Maps vs. Surface Characteristics From Twin Otter Grid Flights in BOREAS 1994.

3.1. Abstract

In BOREAS 1994 the Canadian Twin Otter research aircraft was flown at a fixed altitude of about 30 m agl over two 16 km x 16 km heterogeneous grid sites, in an attempt to document the spatial distributions of fluxes of sensible heat, latent heat and CO_2 over typical boreal systems, and to relate them to spatial distributions of surface characteristics. The acquired data were used to construct maps of surface temperature excess over air temperature (ΔT) and Greenness index (GI), as well as flux maps of sensible heat, latent heat and CO_2. Fluxes were estimated by the eddy covariance method, and the scalar and vertical wind variables detrended by a method that takes into account the physical nature of transport during convective daytime conditions. The ΔT maps showed that surface temperatures were relatively cooler over the forests than over the disturbed, regenerating and burn areas. However, their juxtaposition with sensible heat flux maps showed highest heat flux predominantly over the forest areas. Close correspondence was observed between maps of CO_2 flux and greenness. Quantitative comparison of the flux maps for the three intensive field campaigns (IFCs), showed that the CO_2 flux was the most conservative of the three fluxes, while latent heat flux showed the highest variations. Areas with persistent patterns of flux distribution across the IFCs were also identified.

3.2. Introduction

Model studies in the past few decades confirmed the sensitivity of the large scale atmospheric circulation models to lower atmospheric processes [*McCumber and Pielke*, 1981, *Sud et al.*, 1988]. Lower atmospheric processes are driven by surface related phenomena; their occurrence over a large range of temporal and spatial scales, coupled with the heterogeneous nature of the earth surface, have made them difficult to be quantified. Surface flux measurements from fixed point and airborne platforms have been used to

estimate surface-atmosphere exchange processes, with comparable results over homogeneous surfaces [*Desjardins et al.*,1989]. However, over heterogeneous surfaces, flux measurements made at a single point may differ significantly from airborne estimates of area averages. Difficulties arise when nonlinear summations of fluxes from non-static source distributions are approached through linear aggregation procedures [*Lloyd*, 1995]. Airborne measurements over heterogeneous terrain have the potential to integrate variability in surface fluxes and have been widely used in large scale land surface climatology experiments. In particular, grid flight patterns have the potential to quantify regionally averaged flux and - in the case of sufficient surface contrast - to map surface source or sink distributions at scales comparable to those of remote sensing observations and high resolution climate models [*Desjardins et al.*, 1992; *Schuepp et al.*, 1992; *Mitic et al.*, 1995].

In BOREAS 1994, the Canadian Twin Otter atmospheric research aircraft [*MacPherson*, 1996] executed 23 grid flights over two 16 km x 16 km sites that represent typical BOREAS ecosystems in the Northern (NSA) and Southern (SSA) study areas. One of the main purposes of the measurements was the mapping of spatial variation in surface fluxes of sensible heat, water and CO_2 over the grid sites, and to explore the potential of relating airborne observations to the biological and ecological characteristics of the surface. This study reports initial analyses of this data set.

3.3 Site Description

The Twin Otter grid site of the NSA is defined by the diagonal corners of 55.94° N/98.65° W and 55.80° N/98.40° W. The land cover image of the site, with a spatial resolution of 30 m, is shown in Figure 3.1a. The cover data were extracted from the August 20, 1988 Landsat TM scene of the 129 km by 86 km NSA, using bands 1 through 5 and 7. Nine of the 11 cover types defined by the NASA classification scheme [*Hall et al.*, 1996] can be identified, as shown in Table 3.1. More than half of the area is covered by wet and dry conifers. As seen in Figure 3.1a, the southern half of the site is dominated by burn areas, enclosing an unburned stand of primarily black spruce, where regeneration has been taking place in the past 7 to 15 years, with a significant density of bare rock outcroppings (white

color) in the SW corner. The terrain is generally flat to gently rolling, intersected by a few small escarpments and riverbeds.

The diagonal corners for the *grid site of the SSA* are located at 53.92 ° N/104.81 ° W and 53.78 ° N/104.56 ° W. Its land classification distribution, based on bands 1 through 5 and 7 of the August 6, 1990 Landsat TM scene, is also given in Table 3.1 and broadly illustrated in Figure 3.1b. All 11 surface cover types were identified within the grid, with wet conifers constituting about 60 percent of the surface cover. Effects of logging, with new regeneration,

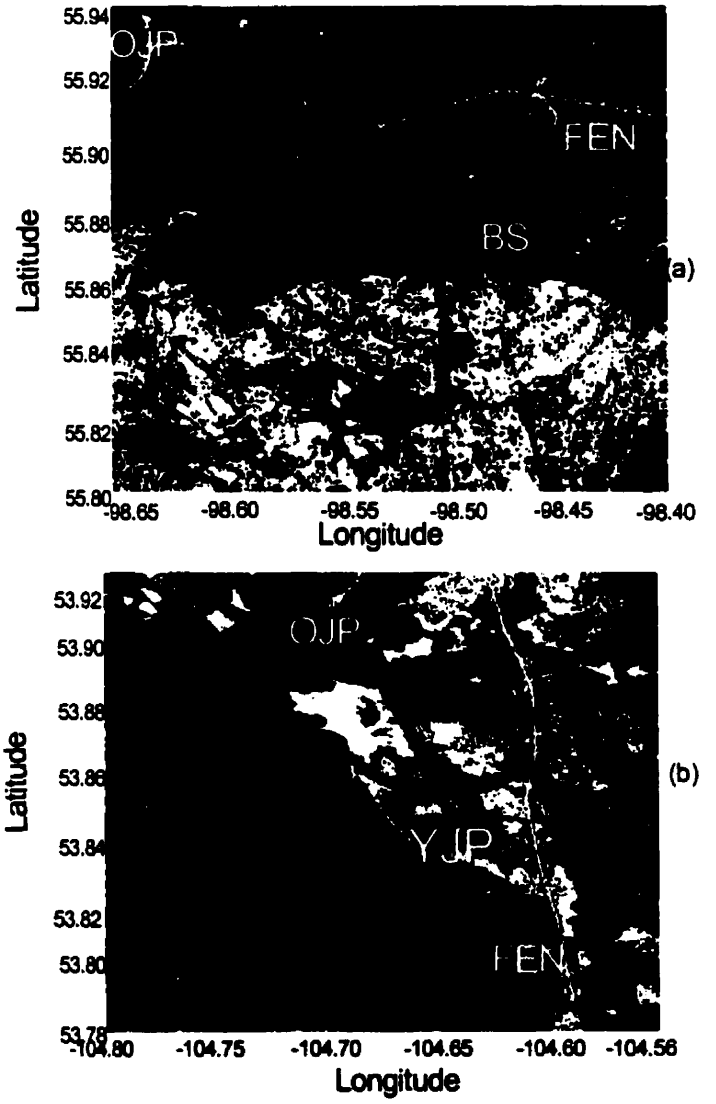

Figure 3.1 : Land classification imagery of the (a) NSA and (b) SSA Twin Otter grid sites. The location of tower sites is indicated

can be seen in the vicinity of the YJP tower. The area beneath the NW-SE diagonal generally contains wetter surfaces, with mixed fen and forest. Forest cover is often controlled by small changes in relief and soil or drainage characteristics.

3.4. Flight Patterns and Data Collections.

The Twin Otter aircraft of the National Research Council of Canada [*MacPherson*, 1990 and 1996] was flown in a grid pattern over the two study sites in either east-west or north-south trajectories. Figure 3.2 a and 3.2 b show the north-south oriented flight track plots for the NSA and SSA grids, respectively. Flight patterns were chosen in response to the prevailing wind direction for closest approach to crosswind conditions. Each grid flight consisted of nine parallel straight lines, spaced 2 km apart, with each line sampled twice in opposite directions, in a sequence that assured that all grid lines were sampled at the same mean time. Flight level was maintained at 30 m agl. With aircraft speed of 60 m s^{-1} it took about 2 hours to complete one grid flight.

A total of 23 grid fights were flown, 14 in the NSA and nine in the SSA, as summarized in Table 3.2. The Twin Otter was instrumented to record, among other parameters, the three components of the wind velocity, incident solar radiation, reflected red (R) and near-infrared (NIR) radiation, air temperature (T_a), radiative surface temperature (T_s),and mixing ratios of H_2O and CO_2. Parameters derived from measured variables include net radiation, R_n, greenness index (GI) (from the Simple Ratio SR = NIR/R), difference between surface and air temperature (ΔT) and potential temperature (θ). Where necessary, corrections were applied for delays between signals recorded at different sensor locations. Data were digitized at 16 Hz. A full description of instrumentation is given by *MacPherson* [1996], and has been summarised in Chapter 2.

Table 3.1. Relative proportion of different land types at the northern and southern study Twin Otter grids, and as sampled by N-S and E-W grid lines

Image Value	Class	NSA Grid			SSA Grid		
		Site	N-S Flight	E-W Flight	Site	N-S Flight	E-W Flight
1	Conifer (wet)	0.36	0.37	0.37	0.57	0.55	0.53
2	Conifer(dry)	0.15	0.15	0.16	0.04	0.04	0.05
3	Mixed	0.10	0.10	0.11	0.11	0.11	0.12
4	Deciduous	0.02	0.02	0.03	0.02	0.02	0.02
5	Fen	0.05	0.05	0.05	0.06	0.06	0.05
6	Water	0.04	0.04	0.00	0.00	0.00	0.01
7	Disturbed	0.03	0.03	0.02	0.01	0.01	0.01
8	Regeneration (younger)	0	0	0	0.04	0.05	0.06
9	Regeneration (Medium)	0.14	0.14	0.13	0.02	0.02	0.02
10	Regeneration (Older)	0.110	0.11	0.1	0.08	0.08	0.08
11	Visible Burn				0.00	0.00	0..00

Table 3.2. Twin Otter grid flight summary of 1994 BOREAS field campaigns

DATE	FLT	FLT DIR	TIME (GMT)	SITE	WEATHER CONDITIONS
May 26	04	E-W	1603-1910	North	Ci, few Cu, winds S
May 31	07	N-S	1611-1933	South	Clear, West winds, becoming NW
Jun 04	09	N-S	1558-1952	South	Initially clear, then Cu with a shower
Jun 07	13	E-W	1609-1912	North	Clear, South winds
Jun 08	14	N-S	1509-1753	North	Clear, warm, WSW winds
Jun 08	15	N-S	1853-2139	North	Clear, warm, SW winds
Jun 10	17	N-S	1624-1904	North	Ci and smoke from fire, light winds
Jun 13	19	N-S	1536-1828	North	Post frontal, cool, Str Cu, East winds
Jul 20	21	E-W	1635-1924	South	Clear, smoke from fire, North winds
Jul 21	22	N-S	1635-1929	South	Mostly clear, few Cu, SW winds
Jul 24	26	E-W	1627-1909	South	Clear, North winds
Jul 26	30	N-S	1638-2005	South	Mostly clear, few Cu, SW-NW winds
Jul 28	33	N-S	1606-1859	North	Clear, NE winds
Aug 01	35	N-S	1536-1839	North	Some Ci, South winds
Aug 04	37	N-S	1534-1807	North	Clear with some smoke, NW winds
Aug 08	39	N-S	1515-1853	North	Few Str Cu, West winds
Aug 31	40	E-W	1707-1928	North	Mostly clear with NW winds
Sep 02	42	E-W	1824-2040	North	Clear, light haze, few Cu, SW winds
Sep 03	43	E-W	1541-1848	North	Clear, Cu forming late in flight
Sep 06	44	N-S	1533-1852	North	Cu greater than 50%, turbulent
Sep 13	49	E-W	1624-1933	South	Clear, WSW winds
Sep 16	53	N-S	1747-1934	South	Absolutely clear, West winds
Sep 19	57	E-W	1528-1823	North	Clear and warm

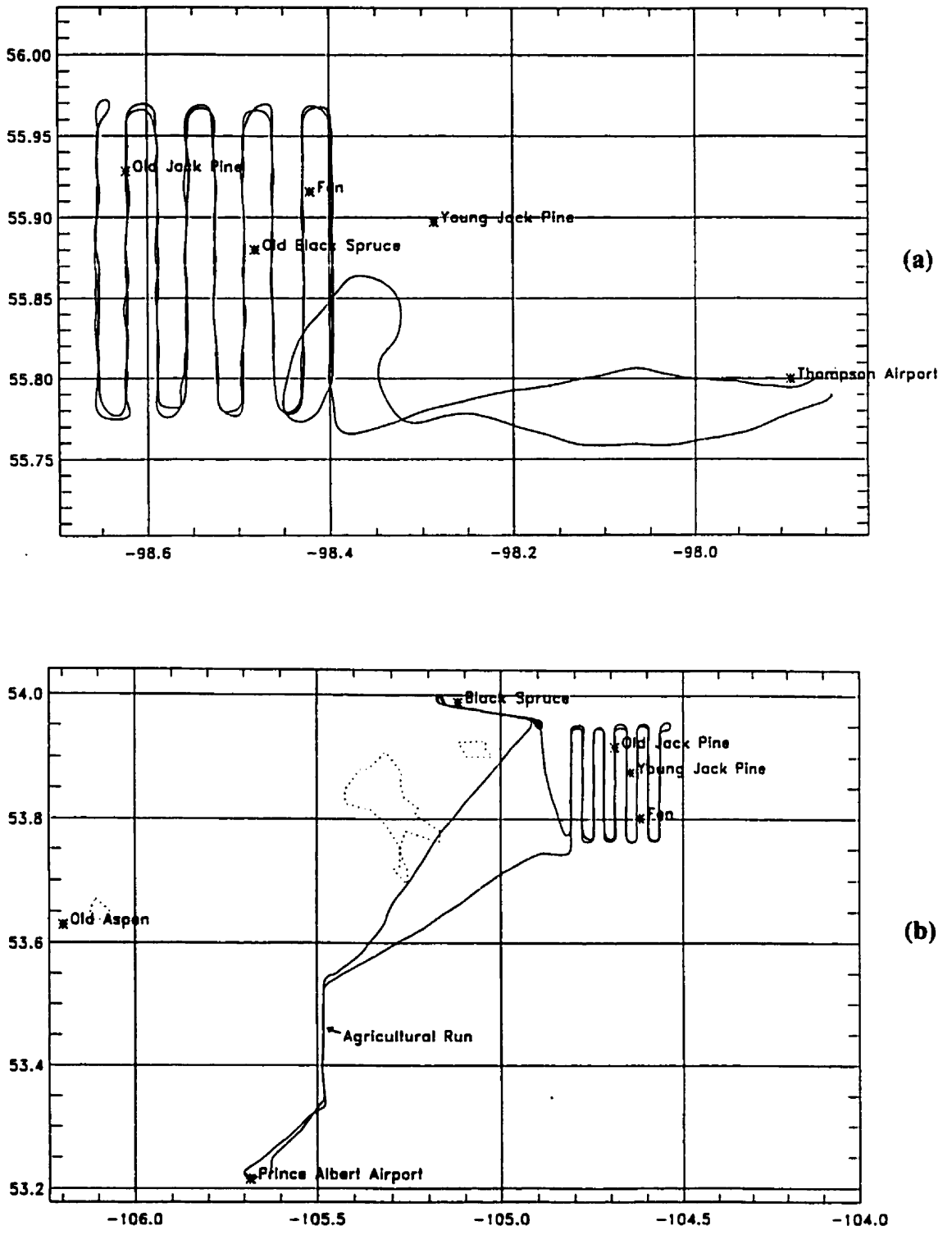

Figure 3.2 : North -South oriented flight trajectories for the Twin Otter grid flights in the (a) NSA and (b)SSA

3.5 Weather conditions and stability

All grid flights were flown around solar noon, most of them under clear weather conditions (Table 3. 2). Mean wind speed varied between 2 m s^{-1} and 8 m s^{-1}, with a mean of 4.3 m s^{-1}, and highest average wind speeds (5.2 m s^{-1}) observed during IFC-3. Wind direction was predominantly southerly or southwesterly. Temperatures ranged from 9.3°C to 26.6°C, with a mean of 19.7°C during the grid flights, and highest mean temperatures (21.1°C) during IFC-2. Thermal stratification was unstable in all cases, with z/L varying from -2.2 on June 10 to -0.07 on July 22, with an average of -0.24 (L ≈ -125m). The Obukhov length L was derived from the mean values of friction velocity u_* and sensible heat flux $\langle w'\theta' \rangle$. The convective boundary layer depth z_i was determined from radiosonde observation and varied from 800 m to 2310 m during the flights.

3.6 Flux Calculations, detrending Procedure and Flux Mappings.

Fluxes of sensible heat, latent heat, and CO_2 were computed by eddy correlation method. The potential temperature (θ) was used in heat flux estimates, to remove the effects of altitude fluctuations during flight, and mixing ratio was used for H_2O and CO_2 flux estimates, to avoid the need for density corrections [*Wyngaard*, 1988; *MacPherson*, 1990].

The sensitivity of eddy flux estimates to the definition of the mean against which the fluctuations are defined is a major drawback of the eddy correlation technique. A local mean is difficult to determine over heterogeneous surface where changes in surface conditions could cause nonlinear trends or discontinuities in scalar traces [*Mitic et al.*, 1995]. *Caramori et al.* [1994] and *Mitic et al.* [1995] showed that inappropriate choice of detrending procedure can lead to physically unreasonable identification of coherent turbulent structures along a run and - in some cases - to underestimation of flux. In order to avoid choosing a detrending procedure 'by inspection', the detrending procedure described below was designed.

Scalar transport above forest canopies is characterised by coherent structures [*Shaw et al.*, 1985 and 1989; *Gao et al.*, 1989], which dominate the vertical turbulent flux. Using quadrant analysis [*Antonia*, 1981; *Shaw*, 1985], with a scatter plot to display excursions of vertical wind (w') and concentration or temperature (c', θ') from their mean values, the

imposition of a threshold on the flux events corresponds to elimination of points within a hyperbolic hole in the scatter plot, the size of which can be expressed in terms of mean flux [*Grant et al.*, 1986] or standard deviation [*Lenschow and Stephens*, 1980; *Caramori et al.*, 1994]. A progressive increase in the size of the hole systematically removes weaker flux events, leaving the dominant structures, with an effect on the remaining structures that depends on the form of the scatter plot, i.e. on the definition of the mean values. Four methods were used to detrend the scalars and vertical wind along each flight line: linear detrending (**LD**), and non-linear detrending based on a Fourier series truncated at the second term (**ST**), third term (**TT**) and fifth term (**FT**) fitted through the data. Using quadrant analysis, fluxes were classified into gradient (**GR**) and countergradient (**CGR**) modes, and a hyperbolic hole of size $k\sigma_{(w'a')}$ imposed on the scatter plot [*Duncan and Schuepp*, 1992; *Caramori et al.*, 1994]. Sigma denotes the standard deviation of the flux contribution w'a', where a' is the fluctuation of the respective scalar.

Values ranging from 0 to 2.5 were assigned to k, causing progressive elimination of weaker flux contributions, and the gradient-to-countergradient ratio (**GR/CGR**) of the remaining flux events determined. The detrending method yielding the highest GR/CGR ratio with increasing k was selected, on the assumption that the most dominant transport is likely to be found concentrated in the gradient modes (such as excess-up or deficit-down for vertical transport of heat or moisture from a warm, evaporating surface). In a few cases, where no single method gave the highest GR/CGR ratio over all k values, the method which gave the highest ratio over the largest range of k was chosen. The sensitivity of flux estimates to the detrending procedure is discussed in section (3.8.1)

Given the selected detrending method, flux estimates along the 16 km flight lines were block-averaged over 2 km windows, with a 1 km overlap between adjoining windows, giving 15 data points along each flight line. By combining the repeated passes over each grid line, this procedure produced a matrix of 135 points per grid, representing a 4 km average per data point, although the data points are not independent. Smoothing was done by cubic spline interpolation, and the interpolated data were used as input to GIS based IDRISI software to produce the maps presented in this paper. (No difference in spatial patterns was observed when the maps based on cubic spline smoothing were compared to those based on

other methods such as distance-weighted interpolation in the IDRISI Interpol module). Given the relatively high temporal and spatial variability in flux patterns resulting from individual flights, our paper will report only analysis of composite maps of latent heat flux, sensible heat flux, CO_2 flux, Bowen ratio, greenness index and surface temperature excess ΔT, for both grids in each IFCs. For the NSA grid, IFC-1, IFC-2 and IFC-3 maps were composited from five, four and five grid flights, respectively, and for the SSA grid, from three, four and two flights, respectively.

3.7 Comparing Maps for Similarity and Persistence

Visual inspection for pattern similarity tends to be biased towards features within certain spatial scale ranges [*Merriam and Sneath*, 1966], while correlation coefficients are biased towards extreme values and relatively insensitive to similarity in spatial patterns. As a more robust alternative to determine similarity between maps of different parameters, or maps between the same parameter observed at different times, we modified a procedure given by *Jackson et al.* [1989] as follows: The variables A_{ij} at each control point on a map are transformed into a set of values Z_{ij}, by subtracting the mean and normalizing the difference by the standard deviation of the differences s:

$$Z_{ij} = \frac{A_{ij} - \bar{A}}{s} \qquad (3.1)$$

The similarity between two transformed maps is then established on the basis of similarity in the sign of Z_{ij} pairs as

$$C_s = \frac{m+n}{m+n+p} \qquad (3.2)$$

where C_s is the similarity coefficient, m, n and p are the numbers of Z_{ij} pairs with negative, positive or mixed signs. Values of C_s vary from 0 (no similarity) to 1 (absolute similarity).

We define features of flux maps as persistent if they retain their properties throughout the three IFCs. Maps of persistence can then be analyzed for surface characteristics that may or may not be conducive to persistence. To delineate a persistence feature, the data points in

the grid array of a given flux, for a given IFC, are transformed using Equation (3.1). An array of indicators I_{jk} is obtained by comparing the transformed elements, and I_{jk} is assigned a value of 1, 2 or 3 if the elements for the three IFCs are all negative, all positive or mixed, respectively. The resulting array of I_{jk} is contoured to give a persistence feature map for the flux concerned.

3.8 Results and Discussion

3.8.1 Sensitivity of the detrending scheme.

Flux estimates were fairly robust vis-à-vis the various detrending procedures, with differences usually between 10% and 15%, attributable most likely to differences in surface source and sink distributions. Generally, the detrending procedure selected on the basis of our detrending scheme was found to give the highest mean flux estimate. Latent heat flux was found to be most sensitive to detrending, followed by CO_2 flux and sensible heat flux.

Since spatial data are location dependent and - especially in the case of overlapping 'windows' - are not independent of their nearest neighbor, their quality can to some extent be measured by the degree to which successive data points in a grid array resemble each other [*Isaak and Strivastava,* 1989]. We carried out a sensitivity test to evaluate the resemblance between successive data points along the flight lines of three randomly selected grids (three sets of 15 x 9 data matrices), for linear (LD) and nonlinear detrending by Fourier series truncated at the third term (TT) throughout the grids.

The optimally selected detrending method (ST) was also applied individually to each grid line. The "h-scatter plots" [*Isaak and Strivastava*, 1989] of the three data sets were used to determine the correlation between successive data points with spatial separation h. Figure 3.3 shows the h-scatter plot of LE for the case of h = (0,1), i.e. for pairing a window-averaged flux with that of the adjacent window. As seen in Figure 3.3, the selected method (ST) gives the best fit, with a correlation of 0.82, suggesting that it does indeed give the best description of the grid data sets. This was generally found to be the case, with ST providing the most appropriate detrending method (in about 80% of cases), followed by LD. It implies that while there were trends in the scalar signals they were not very pronounced.

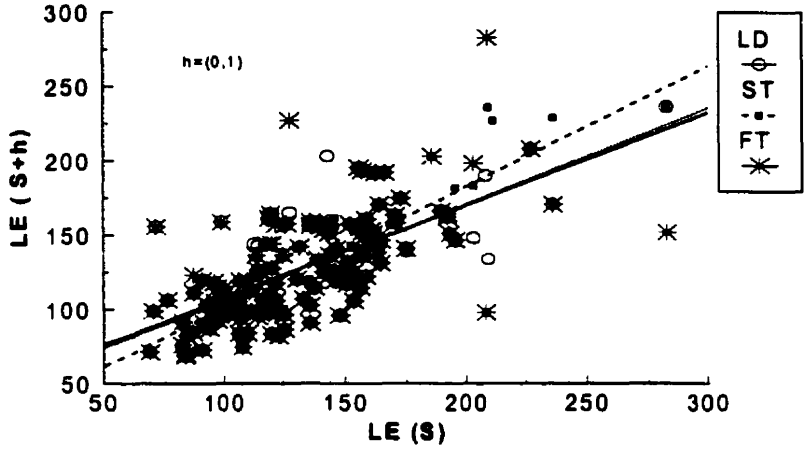

Figure 3.3 : h-scatter plot of latent heat (LE); LE(S) is the value of LE at locations S and LE(S+h) is the value of the next grid point along the flight line. The correlation coefficients for LD, ST and FT are 0.71, 0.82 and 0.64 respectively

3.8.2 Representativeness of the fluxes.

The reliability of estimated fluxes and of the resulting flux maps depends on the extent to which the fluxes represent the grid surfaces. To assess this, we compared the overall distribution of land surface types within the grid sites with the distributions within the surface area strips effectively sampled by aircraft trajectories ('flux footprint') at an altitude of 30 m (Table 3.1). The footprint estimates were based on trace gas release experiments performed over the boreal forest, calculated for wind direction perpendicular to the flight path and for the case of unstable thermal stratification (L = - 100 m). This represents the worst-case scenario of a very narrow footprint, where the area of maximum contribution to the flux is from canopies about 60 m upwind of the flight path and 80% of the flux is estimated to originate from within the nearest 200 m upwind [*Kaharabata et al.*, 1997]. Estimates were made separately for N-S and E-W trajectories. As shown in Table 3.1, over 96 percent of each land cover type was seen by the aircraft for both flight orientations in both grids. The dominant ecosystem types that characterize between 88% and 85% of the NSA grid and SSA grid, respectively, are represented proportionally with average errors of < 1% and 1.8%, respectively, even within the constrained footprints of the unstable case.

3.8.3 Maps of Surface Characteristics

Greenness index (GI) and surface temperature excess over air temperature (ΔT) were mapped from downward looking airborne sensors with a narrow viewing angle, restricting measurements to a strip approximately 3 m wide beneath the aircraft. Maps of these surface characteristics are presented on the assumption that these strips adequately document the spatial distribution of surface features.

The composite maps of (ΔT) and GI for the two grid sites are given in Figures 3.4 to 3.7, together with maps of flux estimates. At the NSA grid, the most striking feature is the surface temperature discrepancy between the warmer regenerating burn area in the southern half of the site (Figures 3.5 and 3.6) and the cooler forested areas to the North of it, which matches in temperature the unburned pocket in the center of the burned area. The high surface temperatures in the SW is attributed to a higher proportion of exposed rock. The highest and lowest values of (ΔT) were observed during IFCs 1 and 3, respectively, and the average range of (ΔT) was about 5 °C. The corresponding greenness maps (Figures 3.4 and 3.5) show an inverse relationship with surface temperature, as expected, and higher values of GI over the mature forest than over the regenerating burn areas, with lowest values in the area of partly exposed rock. Highest and lowest values of GI were observed during IFCs 2 and 3, respectively.

The SSA grid is characterized by a NW-SE diagonal structure, as noted in Figure 3.1b, which is strongly reflected in the surface temperature signal (Figure 3.7), with an average range of (ΔT) about 8 °C. The surface temperature excess of the logged and regenerating areas (upper middle) is persistently prominent. Greenness is in these latter areas, as well as in the wet, cool SW corner with its patchwork of fen interspersed with coniferous forests (Figure 3.7). The inverse relationship between GI and (ΔT) is generally present, although not as pronounced as at the NSA grid. The highest value of GI is also observed during IFC-2, but the lowest during IFC-1, unlike at the NSA grid where the lowest values were observed during IFC-3 due to the earlier onset of senescence.

The relatively low values of (ΔT) observed over the forest are probably attributable to the fact that downward looking radiometers respond to shaded parts of the lower canopy and of the moist ground between trees within their view field [*Hall et al.*, 1995; *Sun and*

Mahrt, 1995], and to the high degree of aerodynamic coupling between coniferous foliage and ambient air resulting from the small characteristic dimensions of needles in convective heat transfer.

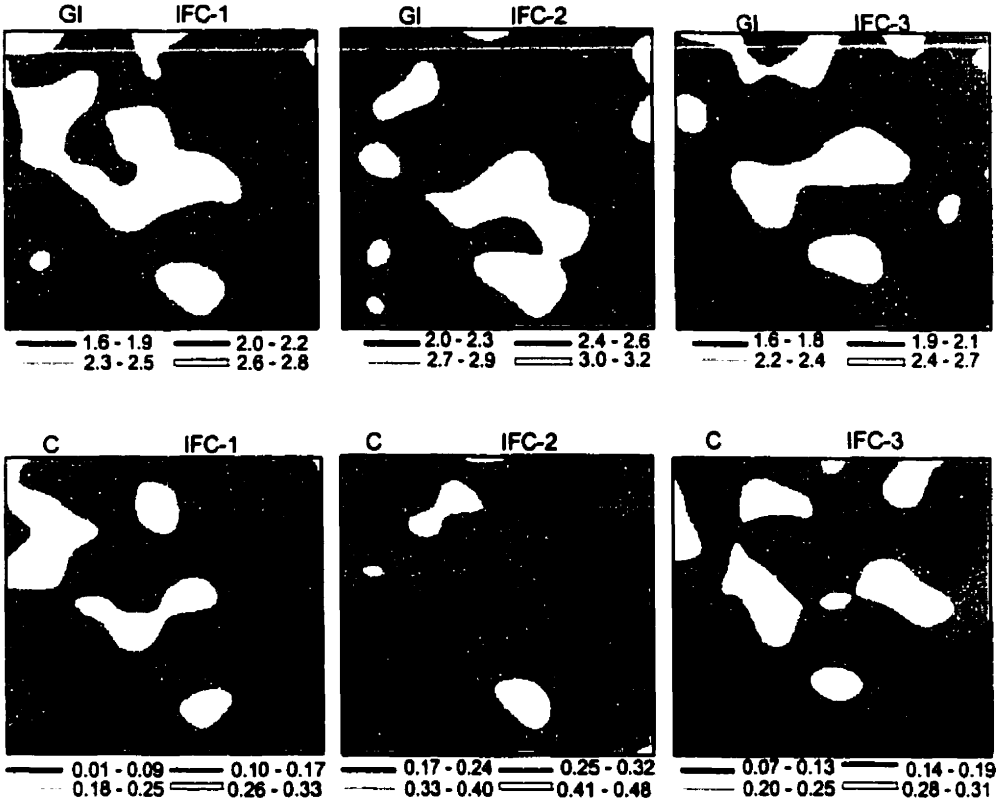

Figure 3.4 : Composite maps of greenness index GI, and CO_2 flux C (mg $m^{-2}s^{-1}$) for the NSA grid, for the three IFCs

3.8.4 Composite flux maps

Although the 288 km of airborne sampling at an altitude of 30 m represented by each of the 23 grid flights can be expected to be sufficient for convergent flux estimate for the overall grid with a relative error of ≤ 5% [*Lenschow and Stankov*, 1986, *Mahrt*, 1998], the 8 km averaging distance represented by each grid point cannot assure a local flux estimate in equilibrium with local surface conditions. Furthermore, violent singular events (with local sensible heat flux densities up to 1.8×10^4 Wm^{-2}) were intermittently encountered

[*MacPherson and Betts*, 1995] and could seriously bias a flux map on any given flight, and radiation conditions varied somewhat between flights (Table 3.2). In view of the resulting temporal variability between maps of individual flights, and in the current absence of a more detailed analysis of each grid flight, this study focuses on composite flux maps representing all flights within the same IFC over a given site. As seen in Table 3.2, such flights were flown during intervals ranging from 3 to 11 days, with the exception of IFC-3, where a last sample of the NSA grid was added 13 days after the initial 7 day period.

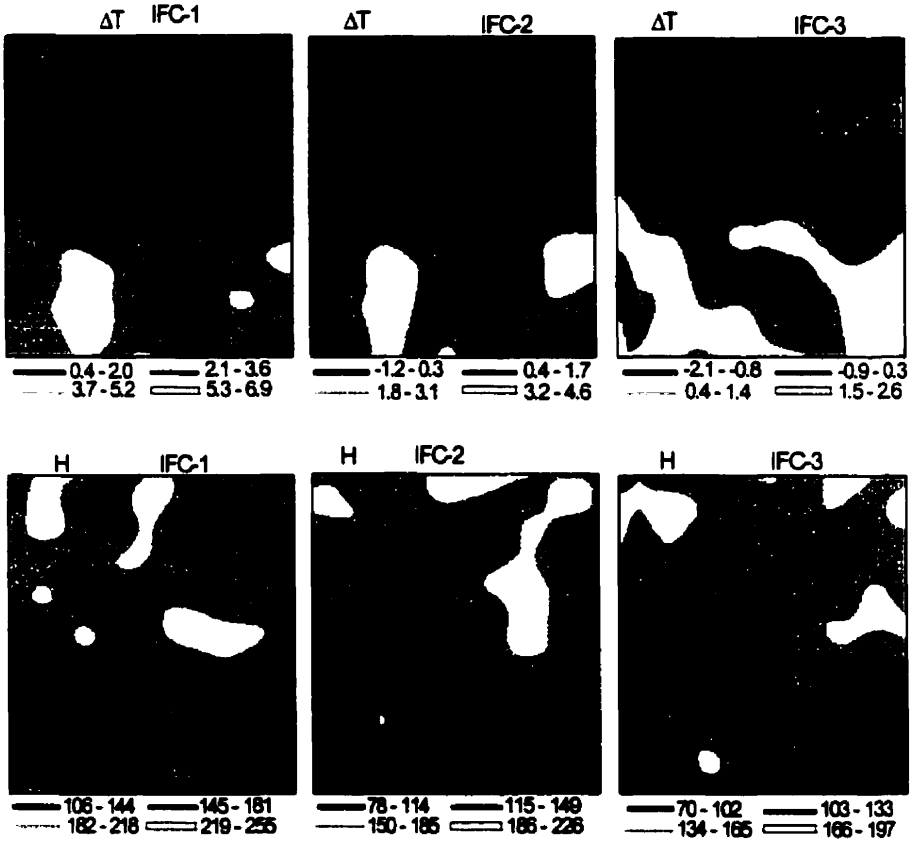

Figure 3.5 : Composite maps of surface temperature excess ΔT (°C) and sensible heat flux H (W m^{-2}) for the NSA grid, for the three IFCs'

The complete set of composite flux maps for the NSA grid, for fluxes of sensible heat (H) and CO_2 (C), are given in Figures 3.4 and 3.5, together with the appropriate surface characteristics of temperature and greenness. Apparent is a high degree of variability between spatial distributions observed during the different IFCs. To what degree this

variability represents real change in surface source and sink distributions rather than sampling fluctuations due to the above-mentioned factors cannot at this stage of analysis be determined with any degree of assurance. As seen in Figure 3.4, CO_2 fluxes reflect the greenness patterns, with a tendency towards higher fluxes on the W side of the unburned area, as well as a signature from the unburned stand near the S edge. The main persistent features in sensible heat maps (Figure 3.5) are a local maximum in the NW corner, around the dry OJP site, and a broader maximum over the mature black spruce stands (center-right). Strikingly absent is a signature from the relatively warm southern half of the grid, i.e. from the regenerating burn area, possibly because even areas with exposed rock were interspersed with shallow ponds and fen-like areas of high surface moisture. No characteristic patterns appeared to emerge from the LE maps (not shown), which are subject to spatially and temporally varying precipitation and drying rates.

The complete set of composite maps for the SSA grid is not shown, but averages of maps for all three IFCs are given in Figure 3.6 and 3.7 for both grids, in an attempt to examine the broadest and most persistent features of the two sites. They should be viewed against the averages of surface characteristics for all three IFCs, also shown in these Figures. The sensible heat flux patterns show the decoupling from radiometric surface temperature (or ΔT) more clearly at the NSA than at the SSA grid site. The dominance of the OJP and black spruce area in the maps of H of the NSA grid is also reflected in the Bowen ratio (BR = H/LE). Over the SSA grid, sensible heat and BR are highest in the northern part where the OJP sites and various clearings and regenerating stands affect the energy balance. OJP stands towards the NW corner also appear high in H and BR, in general agreement with findings in the NSA. The local maximum in LE emerging in these averaged patterns in the south eastern region of the burn may be associated with a relative abundance of shallow surface water during most of the IFCs in that area. The relatively high value of average LE at the SSA grid is largely due to high values (152 to 302 W m^{-2}) in the map for IFC-2 (not shown) associated with intensive precipitation prior to the start of IFC-2. Overall, the most clearly defined relationship between fluxes and surface features is that between GI and CO_2 flux.

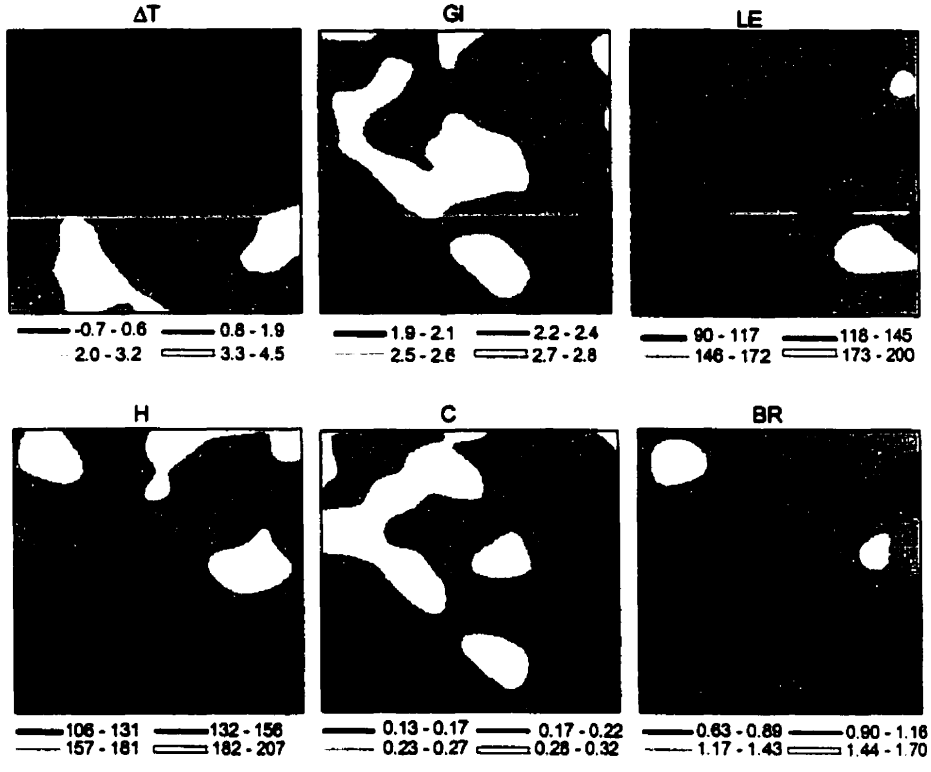

Figure 3.6 : Average maps (over all three IFCs) of surface characteristics, fluxes (H and C) and Bowen ratio (BR) for the NSA grid

The high sensible heat flux over the forest has already been the subject of study [e.g. *Hall et al.*, 1995; *Mahrt and Sun*, 1996). It may be explained both physically and physiologically, through the generally lower albedo of forests which provides more available energy [*Mahrt and Ek*, 1993], and stomatal control in the face of a rapidly drying boundary layer.

3.8.5 Similarity between flux maps and persistence features

Table 3. 3 shows the similarity coefficients (C_s) and correlation coefficients (R), for the flux distributions of H, LE and C between IFC-1 and IFC-2, IFC-1 and IFC-3, and IFC-2 and IFC-3, at both grid sites. Both show a similar trend but are not linearly related, and the low values of R underlines its questionable suitability to characterize spatial data measured

under different conditions. At the NSA grid, maps of H exhibit a consistent degree of similarity in terms of C_s values of about 0.68 in all cases, somewhat higher than the corresponding values for the SSA grid. Interestingly, values and trends for CO_2 flux are very

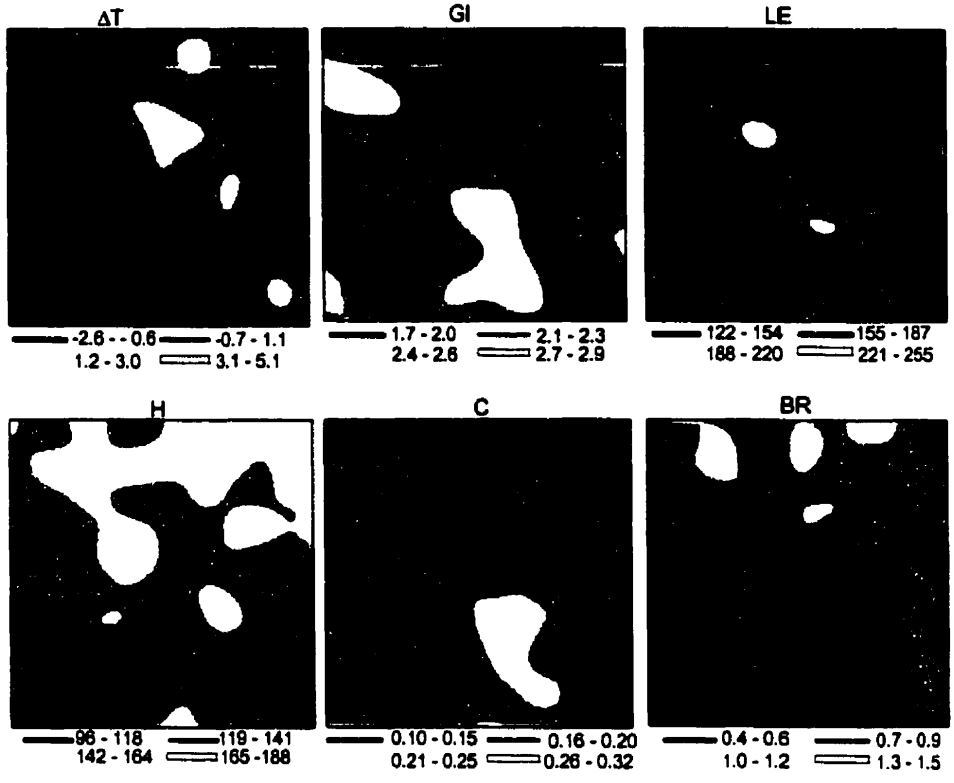

Figure 3.7 : Average maps of surface characteristics, fluxes (H, LE and C), and Bowen ratio (BR) for the SSA grid

similar for both grids, with highest C_s value for comparison between IFC-1 and IFC-3, followed by that between IFC-1 and IFC-2. Among the three fluxes, LE maps show the highest degree of variability in spatial pattern from one IFC to another, suggesting different control mechanisms, with more direct influence of non-physiological sources such as shallow surface water, compared to other scalars.

Delineating areas with persistent flux features is an important step in establishing a relationship between surface characteristics and surface fluxes. The maps shown in Figure 3.8 indicate areas of persistence for high and low values of sources and sinks throughout the three IFCs. The areas of high sensible heat flux in the northern half of both grids, associated

with high values of BR are quite consistent, as are the cooler areas in the southern part of the grids. As expected, LE patterns in the NSA grid show little persistence, but the relative maximum of LE diagonally across the SSA grid (Figure 3.7) appears persistent. The patterns of CO_2 flux in the NSA grid are consistent across the IFCs, while in the SSA grid the most persistent features are the high and low areas along a vertical axis slightly to the E of centre line. The similarity between persistence in C and the patterns of greenness (Figures 3.6 and 3.7) is apparent.

Table 3.3. Correlation coefficient (R) and similarity coefficient (C_s) of fluxes at SSA and NSA grid sites.

	Southern Study Area Grid						Northern Study Area Grid					
	IFC-1, IFC-2		IFC1, IFC-3		IFC-2, IFC-3		IFC-1,IFC-2		IFC-1,IFC-3		IFC2, IFC-3	
	C_s	R	C_s	R	C_s	R	C_s	R	Cs	R	C_s	R
CO_2	0.60	0.40	0.65	0.40	0.65	0.32	0.66	0.50	0.69	0.53	0.58	0.25
LE	0.53	0.21	0.54	0.08	0.56	0.19	0.56	0.35	0.49	-0.01	0.50	0.01
H	0.52	0.08	0.48	-0.02	0.61	0.31	0.67	0.54	0.68	0.47	0.68	0.47

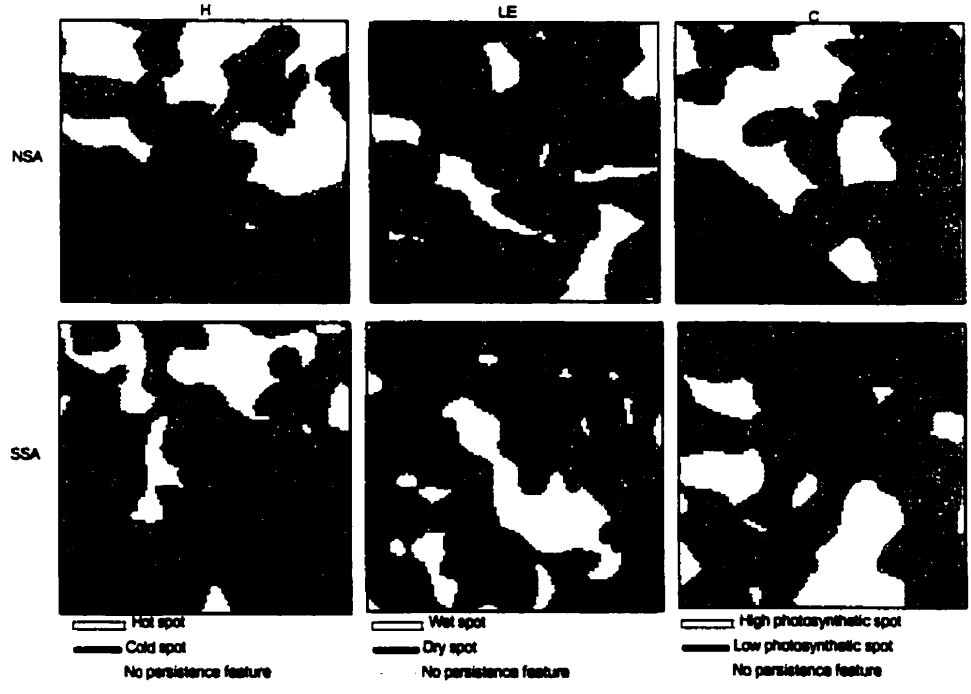

Figure 3.8 : Persistence maps for H, LE and C for the NSA and SSA grids

3.8.6 Flux correlation with surface characteristics.

Some correlation between fluxes and observed surface characteristics should be expected to the degree that the latter are indicators of the physical or biological processes that govern the exchange of energy and mass. We would expect, for example, a negative correlation between CO_2 flux (C) and greenness (GI) (considering the sign of the photosynthetic flux), or between moisture flux (LE) and (C), and a positive one between sensible heat flux (H) and surface temperature excess (ΔT). Observed correlations between these parameters, for IFC-1, are shown in Figure 3.9. As already shown by the maps of fluxes and surface characteristics, the clearest correlation is between GI and C. There is some suggestion of the expected negative correlation between LE and C, but H and (ΔT) appear largely uncorrelated or even negatively correlated, for reasons associated primarily with the black spruce stands, as discussed above. R values for analysis of the full set of grid flights are given in Table 3.4. When interpreting these results, it must be kept in mind that these preliminary estimates have not yet been footprint corrected, i.e. flux estimates over a run segment are correlated with surface characteristics directly under the flight path rather than within the upwind surface source or sink area. A more detailed analysis will have to use local observations on surface roughness, wind direction and stability to construct the upwind surface footprint whose surface characteristics (from satellite-based remote sensing observations) would then be correlated with the flux.

Table 3.4 Correlation coefficient between GI and C, C and LE, ΔT and H, and between C and H.

	Northern Site			Southern Site		
	IFC1	IFC2	IFC3	IFC1	IFC2	IFC3
GI and C	-0.80	-0.50	-0.79	-0.72	-0.21	-0.40
C and LE	-0.31	-0.43	-0.74	-0.53	-0.65	-0.33
ΔT and H	-0.43	-0.20	-0.24	0.36	-0.22	-0.28
C and H	-0.57	-0.14	-0.44	-0.28	-0.22	-0.30

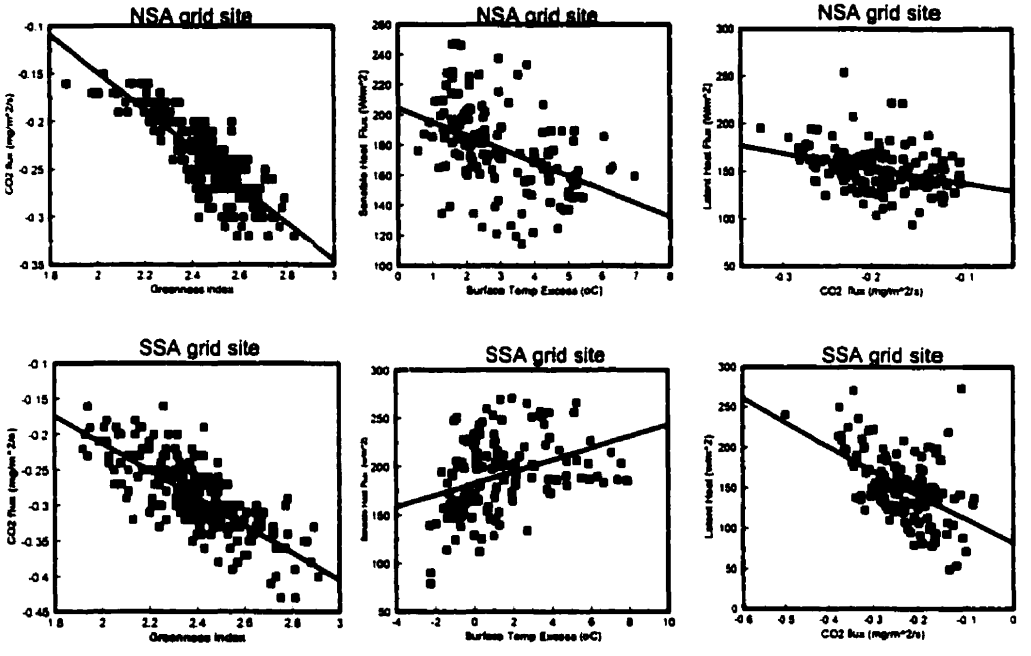

Figure 3.9 : Correlation between GI and C, C and LE, and ΔT and H for IFC-1

3.9 Conclusions

This study maps the spatial distributions of the fluxes of sensible heat, latent heat and CO_2 over the Twin Otter grid areas at the NSA and SSA, using data processing procedures that have been optimized for convective, daytime conditions. Footprint analysis for the flight trajectories across the grid sites have already shown that the areas effectively sampled by the aircraft are representative of the 16 km x 16 km grid surfaces, and the 288 km flight lines at an altitude of 30 m of each grid flight can be expected to provide convergent flux averages for the overall grids. However, the variability in spatial distribution between grids constructed from single flights is high due to varying radiation and boundary layer conditions and due to the presence of highly intermittent extreme flux events that may bias the mapping exercise of any given flight. For this reason, this paper focuses on composite flux maps for each grid and each IFC, on overall average grid patterns for all IFCs, and on persistence analysis for distribution patterns between IFCs. We presume that the general patterns of

averaged flux density and an outline of areas with persistence in flux density characteristics may provide the link-up point with geographically referenced, regional climate models, at the high resolution end of their spatial scales.

The dependence of flux patterns on the relative distribution of surface covers was exemplified by the differences between the SSA and NSA grids. Differences in flux patterns from one IFC to another were more likely due to changes in soil moisture distribution and plant physiological properties than to changes in radiant energy, although the latter had a greater influence on the magnitudes of the fluxes.

Comparison of fluxes against surface properties showed a higher correlation between CO_2 flux and greenness than might have been expected in this complex ecosystem, while a poor (and sometimes negative) correlation was observed between (ΔT) and sensible heat flux in the composite maps, in contrast to observations over agricultural canopies. This was associated with cool surface temperatures, visible to radiometric remote sensing of temperature, between trees that are aerodynamically and often biophysically decoupled from the surface. These observations imply that it will be easier to infer the regional carbon balance from satellite-based radiometric observations than the water or energy balance, at least for the growing season conditions covered by the BOREAS IFCs.

CONNECTING STATEMENT LINKING CHAPTERS 3 AND 4

The detrending scheme that was developed proved to be objective, and an effective tool for spatial averaging of scalar traces. The Twin Otter data from BOREAS 1994 have been used to study the spatial and temporal variation in the fluxes of sensible heat, latent heat and CO_2. The potential of using airborne data to map spatial variability in fluxes over heterogeneous surfaces and to relate the fluxes to the surface properties were demonstrated in Chapter 3. The next chapter focuses on the comparison between the 1994 and 1996 data. The spatial and temporal variation in the fluxes in both year are examined to determine areas where there have been changes in the flux patterns and area where patterns have remained consistent.

In view of the nature of this study, some of the procedures used in Chapter 4 are identical to those given in Chapter 3. In some cases, they have been summarised with reference to Chapter 3, but where it was found appropriate they are left in their original format to make the chapter as self-contained as possible.

The material presented in Chapter 4 is in press in the Journal of Geophysical Research [*Ogunjemiyo et al.*, 1999].

CHAPTER 4

COMPARISON OF THE SPATIAL AND TEMPORAL DISTRIBUTION OF FLUXES OF SENSIBLE HEAT, LATENT HEAT AND CO_2 FROM GRID FLIGHTS IN BOREAS 1994 AND 1996

4.1 Abstract

Analysis of airborne flux measurements of heat (H), moisture (LE) and CO_2 (C) over two 16 km x 16 km heterogeneous grid sites in BOREAS 1994 (IFC-2) and 1996 are compared in order to examine persistence and variability in the distributions of surface characteristics and fluxes between the two years. The data used were obtained in grid patterns flown at an altitude of 30 meters above ground, under generally clear sky and thermally unstable conditions. Fluxes were estimated by the eddy correlation method, and flux and surface characteristics maps were constructed by block averaging over 2-km windows along the flight lines. Maps were analyzed for similarities and used to quantify spatial variability of the fluxes. Sensitivity analysis suggested relatively minor effects of boundary layer variability and window size on the main features of the source/sink distributions. The correlation of incident radiation against the grid averaged values of C was found to be higher than that against H and LE. By comparing the coefficients of variation of the fluxes with those of net radiation, the dominant role of surface inhomogeneity, as opposed to local variations in solar energy input, on spatial variation of flux distributions was confirmed. Mesoscale motion was found negligible over the grid sites, probably due to the small sizes of homogeneous subareas with sufficient surface contrast to induce thermally generated motion. A high degree of correspondence was observed between CO_2 flux and greenness index; however, the correlation between them was site- and time-specific. The previously observed low correlation, due to decoupling between sensible heat flux and surface minus air temperature difference (ΔT) primarily over old black spruce, was confirmed. Analysis of the boundary layer profiles showed that the high Bowen ratio over the forest contributed to the growth and development of the observed deep boundary layers over the sites, but no clear correlation emerged between boundary layer depth and observed

near-surface fluxes.

4.2 Introduction

Models of biosphere-atmosphere interactions have been developed primarily for homogeneous surfaces. Extrapolation of such models to heterogeneous surfaces requires validation by data that integrate measurements over areas typical of the land surface and over an adequate period of time. The analysis of the data obtained by the Twin Otter aircraft [*Ogunjemiyo et al.*, 1997] during BOREAS 1994 suggests that the prospect of using boundary layer models to estimate surface fluxes depends on the scalar under consideration and the nature of the surface cover. This does not invalidate the previously demonstrated potential of grid flights to map temporal and spatial variations in surface fluxes and to relate the observed flux estimates to surface characteristics [*Desjardins et al.*, 1992; *Schuepp et al.*, 1992; Mitic *et al.*, 1995] in principle, but makes its application to the boreal landscape much more of a challenge.

The analysis presented in this chapter uses Twin Otter data from BOREAS 1994 IFC-2 and the 1996 IFC to compare the spatial distributions of fluxes of sensible heat (H), latent heat (LE) and CO_2 (C) at the two grid sites between these two observation periods. This involves identification of areas at the sites where significant changes in flux patterns occurred and their links to patterns of surface characteristics. The statistical stability of flux maps derived from the sampling and analysis procedure used are also discussed.

4.3. Data acquisition and processing

4.3.1 Sites

The two grid sites, the NSA and SSA grids, where the data were collected, have already been described in the previous chapter. Briefly stated, the sites were heterogeneous, with different size patches of surface cover, and plant species at different stages of growth. The northern half of the NSA grid, which included the old jack pine (OJP) and old black spruce (OBS) tower sites, was covered by wet and dry conifers and the southern half by a former burn area in various stages of regeneration, with one centrally located unburned 'pocket'. The SSA grid, which includes the OJP, young jack pine (OJP) and fen sites, was

dominated by wet conifer mixed with fen, below the NW-SE diagonal, with drier conifer, logged and regenerating areas above it.

4.3.2 Sampling and weather conditions

The 1994 (IFC-2) data set consisted of eight grid flights, four at each site, flown during July and August, and the 1996 set nine grid flights, four in the SSA and five in the NSA, also flown during July and August. As seen from Table 4.1 the SSA flights preceded the NSA flights in both years, and all flights at each site were flown within ten days, except the 1996 flights in the SSA, which were spread over twenty days. The airborne data were collected by the Canadian Twin Otter (TO) atmospheric research aircraft [*MacPherson*, 1990 and 1996] in a grid pattern, flown at approximately 30 m agl, at a mean air speed of 60 m s^{-1}. A detailed description of the grid flight patterns is given in Chapter 3.

Data were digitized at 16 Hz. Observed data used in this study include air temperature (T_a), surface temperature (T_s), incident solar radiation, reflected red (R) and near infrared (NIR) radiation, and mixing ratios of CO_2 and H_2O. Parameters derived from measured variables include net radiation, R_n, greenness index, GI (from the Simple Ratio SR = NIR/R), difference between surface and air temperature ($\Delta T=T_s-T_a$) and potential temperature (θ). More information about the instrumentation is given by *MacPherson* [1996].

The general weather conditions during the flights are summarized in Tables 4.1 and 4.2. All flights were flown around solar noon. Except for Julian day 211 in 1996, when the sky was overcast, the flight periods were characterized by mainly sunny conditions. The wind at the SSA was generally stronger in 1994 than 1996, with average values of 4.4 m s^{-1} and 3.5 m s^{-1}, respectively. The reverse is the case in the NSA where average wind speed was 3.5 m s^{-1} in 1994 and 4.1 m s^{-1} in 1996. The average air temperatures in 1994 and 1996 were 19.7 °C and 21.1 °C, respectively, at the NSA site, and 22.5 °C and 18.7 °C, respectively, at the SSA. Thermal stratification, as defined by z/L, where L is the Obukhov length, was unstable (negative z/L) in all cases. Values of L are given in Tables 4.2a,b.

Table 4.1. Twin Otter grid flight summary.

Year	Date	Day	Flight No	Flight Dir	Time (GMT)	Site	General weather conditions
1994	Jul. 20	201	21	E-W	1704-1859	SSA	Clear, smoke from fire, North winds
1994	Jul. 21	202	22	N-S	1700-1854	SSA	Mostly clear, few Cu, SW winds
1994	Jul. 24	205	26	E-W	1653-1844	SSA	Clear, North winds
1994	Jul. 26	207	30	N-S	1705-1856	SSA	Mostly clear, few Cu, SW-W winds
1994	Jul. 28	209	33	N-S	1617-1810	NSA	Clear, NE winds
1994	Aug.01	213	35	N-S	1547-1752	NSA	Some Ci, South Winds
1994	Aug. 04	216	37	N-S	1546-1749	NSA	Clear with some smoke, NW winds
1994	Aug. 08	220	39	N-S	1526-1748	NSA	Few Str Cu, West winds
1996	Jul. 09	191	58	E-W	1705-1906	SSA	Generally clear and sunny, SSW winds
1996	Jul. 20	202	68	E-W	1605-1810	SSA	Mostly clear, few Cu, SE winds
1996	Jul. 27	209	71	N-S	1722-1908	SSA	Overcast skies, SE winds
1996	Jul. 29	211	72	E-W	1631-1818	SSA	Clear, small Cu across grid, SSE winds
1996	Jul. 31	213	76	E-W	1456 1645	NSA	Generally clear, South winds
1996	Aug. 02	215	79	N-S	1447-1638	NSA	Clear, SW winds
1996	Aug. 03	216	80	N-S	1615-1801	NSA	Clear with some smoke, East winds
1996	Aug. 05	218	81	E-W	1615-1810	NSA	Few Str Cu, South winds
1996	Aug. 08	221	83	E-W	1450-1640	NSA	Clear, North winds

4.3.3 Data processing

Vertical turbulent fluxes of sensible heat, latent heat and CO_2 at the flight level were computed from the time-averaged covariance ($w'\rho'$) between fluctuations of vertical wind (w') and the scalar of interest (ρ'). Potential temperature (θ) was used to compute H, and the

use of mixing ratios for H_2O (q) and CO_2 (c) obviated the need for density correction (MacPherson, 1990). Turbulent fluctuations were computed as the difference between instantaneous and mean scalar quantities, with means determined by applying detrending techniques developed by *Ogunjemiyo et al.* [1997] (Chapter 3). Fluxes were estimated along each of the flight lines, and averaged over all the flight lines to obtain the grid average fluxes.

The mapping procedure adopted for creating the flux maps was the same as that used by *Ogunjemiyo et al.* [1997]. Flux estimates were averaged over 2 km segments, and the estimates for the two repeated passes averaged into 2 km windows, with 1 km overlap between adjoining windows. This generates a matrix of 135 data points per grid, with 4-km average sampling per data point. Using cubic spline interpolation, the gridded data were smoothed and used as input to GIS-based IDRISI software to produce the flux maps of the grid sites. The same procedures were adopted to produce maps of surface characteristics (surface temperature excess over air temperature, ΔT, and greenness index, GI). Local variations in surface emissivity were not taken into account. Given the fact that the PRT-5 sensor has internal calibration assuming green vegetation canopies with emissivities approaching unity (≥ 0.98), the associated potential error in emissivity of 1 to 2% is not likely to be significant. Also, no atmospheric corrections were made on the surface temperature measurements, since *Perry* and *Moran* [1994] found such corrections to be generally less than 0.5 degrees for aircraft data acquired for their (higher) flight levels at 100 m agl.

The significance of any given factor, such as radiation, in the complex relationships that affect flux magnitudes, can only be deduced indirectly by comparing the variability in its estimates to that in the flux estimates. We used this approach based on the normalized variances in the flux maps, V_f, and in the radiation maps, V_r, i.e.

$$V_f = \frac{\frac{1}{NM}\sum_{j=1}^{j=M}\sum_{i=1}^{i=N}[F(i,j)-\bar{F}]^2}{\bar{F}}, \quad V_r = \frac{\frac{1}{NM}\sum_{j=1}^{j=M}\sum_{i=1}^{i=N}[R(i,j)-\bar{R}]^2}{\bar{R}} \qquad (4.1)$$

where F(i,j) and R(i,j) are the grid data matrix in the two maps, with M rows and N columns, and the overbar indicates average of all the map data.

Table 4.2a. Northern study area grid average parameters.

Year	Flight No	Julian day	Wind $m\ s^{-1}$	T_a °C	T_s* °C	Gi*	Rn Wm^{-2}	-L m
1994	33	209	3.4	21.7	23.9	2.73	549.3	64.5
	35	213	1.6	22.1	22.5	2.74	465.2	22.4
	37	216	4.0	18.5	19.5	2.75	496.5	125.6
	39	220	3.1	16.1	16.7	2.74	482.8	68.7
1996	76	213	4.0	23.8	26.5	2.49	474.7	129.7
	79	215	5.0	24.2	25.2	2.49	539.2	325.6
	80	216	3.4	25.5	29.8	2.49	585.2	72.8
	81	218	4.1	22.6	26.1	2.39	486.5	116.4
	83	221	4.1	9.6	15.3	2.19	327.4	134.3

* Please note: Shifts in instrument sensitivity might have caused minor changes in absolute values between, but not in relative distributions within, the two years.

Table 4.2b. Southern study area grid average parameters.

Year	Flight No	Julian day	Wind $m\ s^{-1}$	T_a °C	T_s* °C	Gi*	Rn Wm^{-2}	-L
1994	21	201	5.7	21.5	19.3	2.71	525.9	414.2
	22	202	5.1	26.5	24.7	2.70	622.9	204.5
	26	205	4.9	19.2	20.1	2.84	611.4	146.3
	30	207	1.8	22.9	22.7	2.77	553.8	128.4
1996	58	191	5.0	19.6	25.8	2.3	691.5	151.5
	68	202	2.9	18.4	22.9	2.28	601.1	41.6
	71	209	4.2	17.0	19.6	2.20	291.2	412.2
	72	211	1.9	19.9	23.4	2.26	573.9	14.6

* see note in Table 4.2a.

Data from serial upper-air soundings [*Barr and Betts*, 1994, 1997] released on each of the flight days were used for boundary layer analysis. Because the release time was about 5-10 minutes before, or after each flight, with a two-hour spacing, two successive soundings coinciding approximately with start and end time of the grid flight, can be considered to document the boundary layer conditions during each flight. Estimated parameters include the mixed layer depth, z_i, taken as the depth over which the potential temperature is essentially constant, average boundary layer moisture and changes in boundary layer height, Δz_i, moisture mixing ratio, Δq, and potential temperature, $\Delta\theta$, that occurred during the flight period. Other parameters estimated include the convective velocity scale w_*, convective time scale t_*, temperature scale θ_* and humidity scale q_* in the mixed layer according to *Stull* [1988] as:

$$w_* = \left[\frac{g z_i}{\overline{\theta}} \overline{(w'\theta')}\right]^{1/3}, \quad t_* = \frac{z_*}{w_*}, \quad \theta_* = \frac{\overline{(w'\theta')}_s}{w_*}, \quad q_* = \frac{\overline{(w'q')}_s}{w_*} \quad (4.2)$$

4.4 Results And Discussions

4.4.1 Grid-averaged fluxes

Figure 4.1 illustrates the temporal variations of the grid averaged fluxes at the sites for the 1994 and 1996 observation periods. Each value represents sampling over a 288 km distance, which is expected to provide area-averaged flux estimates with a relative error of $\leq$ 5% [*Lenshow and Stankov*, 1986; *Mahrt*, 1998]. Temporal variability was greater at the SSA than at the NSA; it depended on the nature of the scalar and reflects site-dependent weather effects. The composite, grid-averaged value of H was the same in both years at the SSA, but 24% lower in 1996 than in 1994 at the NSA. Averaged LE was the same in both years at the NSA, but 19% lower in 1996 at the SSA. Averaged C was 18% higher in 1996 than in 1994 at the SSA, but 4% lower at the NSA site. The observed temporal variability in the fluxes was mainly due to variation in incident solar radiation and, to a lesser degree, to changes in flux footprints and boundary layer structure.

The net radiation, R_n, was generally higher at the SSA than at the NSA, with less than 6% difference between the years at each site. It is interesting to observe that the highest

values of C are associated with lowest solar insolation, resulting from haze or cloud cover, and the lowest values of C associated with highest insolation from clear skies. This is tentatively associated with physiological response to high vapour pressure deficits of coniferous trees. In so far as correlations could be established between R_n and fluxes in such small data sets, they were higher for C than for H and LE, and the observed trends between C and R_n are consistent with results from other studies [e.g. *Hollinger et al.*, 1994; *Baldocchi et al.*, 1997] which showed ecosystem uptake of CO_2 enhanced under cloudy skies, when the incoming sunlight is isotropic.

Examination of the boundary layer profiles of mixing ratio (q) and temperature (θ) at the start of the grid flights showed that the timing of the flights coincided with the growing phase of the boundary layer, when the residual layer decays as a result of turbulent mixing triggered by surface heating. The shape of the profiles, nearly constant θ and decreasing q with height within the mixed layer, are characteristic signatures of convective mixed layer turbulence. The averaged values of w_*, t_*, θ_* and q_* (Table 4.3) are typical for a deep mixed layer with vigorous surface heating [*Stull*, 1988; *Betts and Ball*, 1994]. The average growth of the boundary layer during the flight was greater in each year at the NSA than SSA, just as the average values of the mixed layer height, z_i, were higher at the NSA (1056 m in 1994 and 1082 m in 1996) than at the SSA (902 m in 1994 and 976 m in 1996). The structure and growth of the boundary layer is known to be related to H and LE; a change in one of the variables may be explained partly by a change in the other. However, conclusive inferences could not be drawn from the linear regression of z_i against H and LE in our data set.

Difference in atmospheric stability between flight days could also cause variation in the grid average fluxes. As a major component of the flux footprint function, the stability parameter, -z/L, defines the zone within which surface cover significantly contributes to the measured fluxes. Unlike in 1994, the averaged value of L was the same for both sites in 1996, with a wider range of values at the SSA than at the NSA (Table 4.2). This, as well as the fact that the footprint analysis of *Kaharabata et al.* [1997] showed that the various components of the two grid surfaces were sampled adequately even at a more constrained footprint at L = -100 m, makes stability-related variations in the footprint an unlikely contributor to the flux variability.

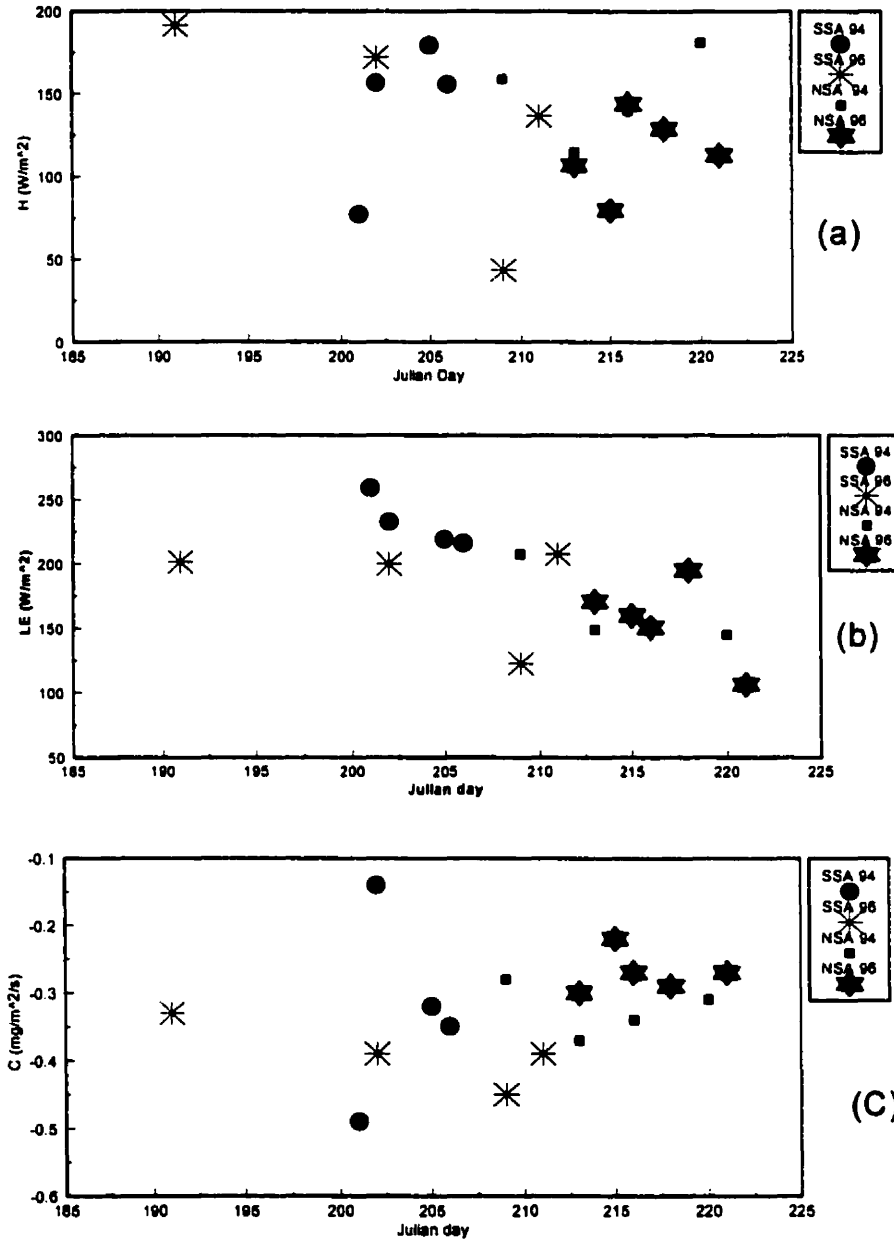

Figure 4.1 : Plots of the grid average fluxes of (a) sensible heat, (b) latent heat and (c) CO_2

Table 4.3. Boundary layer parameters.

Flt No	z_i (m)	Δz_i (m)	W_* m s^{-1}	t_* s	θ_* K	q_* g kg^{-1}
21	746	180	1.2	636	0.06	0.08
22	1180	170	1.7	688	0.08	0.05
26	777	150	1.6	497	0.10	0.05
30	1045	710	1.7	633	0.08	0.05
33	928	644	1.6	577	0.08	0.04
35	800	820	1.4	579	0.07	0.03
37	1116	937	1.6	674	0.07	0.03
39	1227	1034	1.8	657	0.08	0.03
58	1214	65	1.9	576	0.09	0.04
68	1191	973	1.8	666	0.08	0.04
71	714	252	1.0	750	0.04	0.05
72	785	614	1.5	546	0.08	0.05
76	1227	851	1.6	790	0.06	0.04
79	678	688	1.2	591	0.06	0.05
80	977	725	1.5	616	0.08	0.04
81	1660	684	1.8	907	0.06	0.04
83	872	248	1.4	607	0.07	0.03

4.4.2 Maps of surface characteristics

The maps of excess of surface temperature over air temperature (ΔT) and greenness (GI) are shown in Figures 4.2 and 4.3. Since a calibration problem might have affected absolute values of ΔT and GI in 1996, introducing possible bias rather than noise in the data set, and since the emphasis is on relative spatial variability, different scaling was used for these maps. The spatial distribution of ΔT reflects the pattern of absorption and partitioning of energy between the different components of the surface cover, and the distribution of GI documents their physiological status.

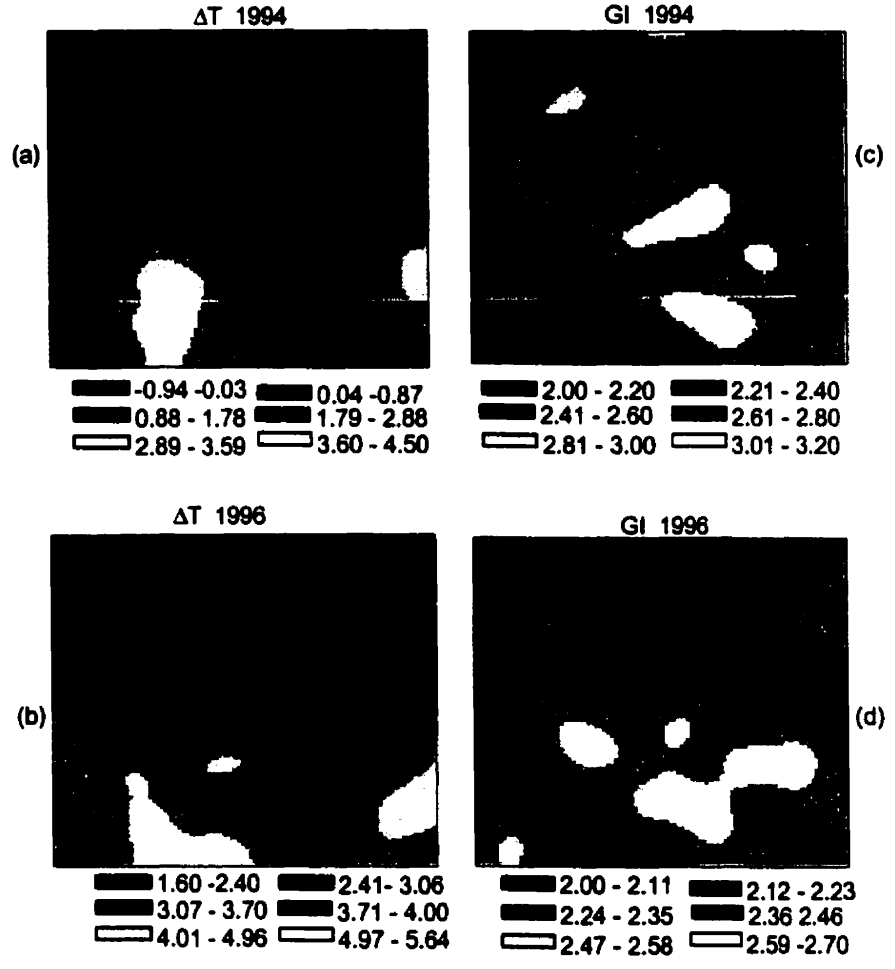

Figure 4.2 : Maps of surface minus air temperature, ΔT (°C) and greenness index (GI) at the NSA grid in 1994 and 1996

The NSA ΔT maps (Figures 4.2a & b) exhibit the contrast in surface temperature between the northern and southern halves of the site. The areas with low ΔT were dominated by tall and closed-canopy conifers, while the areas with high ΔT were primarily covered by shrubs, short and open canopy trees, with an often dry underlying surface that is typical of a regenerating burn area. The correspondence between 1994 and 1996 patterns is very strong, with coefficient of similarity, C_s, of 0.94, and correlation coefficient, R, of 0.84, in spite of some local differences, such as the relatively high values of ΔT over black spruce (around 55.9 N/98.45 W) and over old jack pine (top left corner) in 1996. To what degree such differences may be associated with flight orientation (predominantly N-S in 1994 and E-W in 1996), leading to potential differences in the sampling of anisotropic surface patches, is

not yet clear. A dependence of the spatial extent of mapped temperature anomalies on the orientation of flight lines is suggested by the comparison of temperature maps from N-S and E-W lines in the 1994 data [*Ogunjemiyo et al.*, 1997].

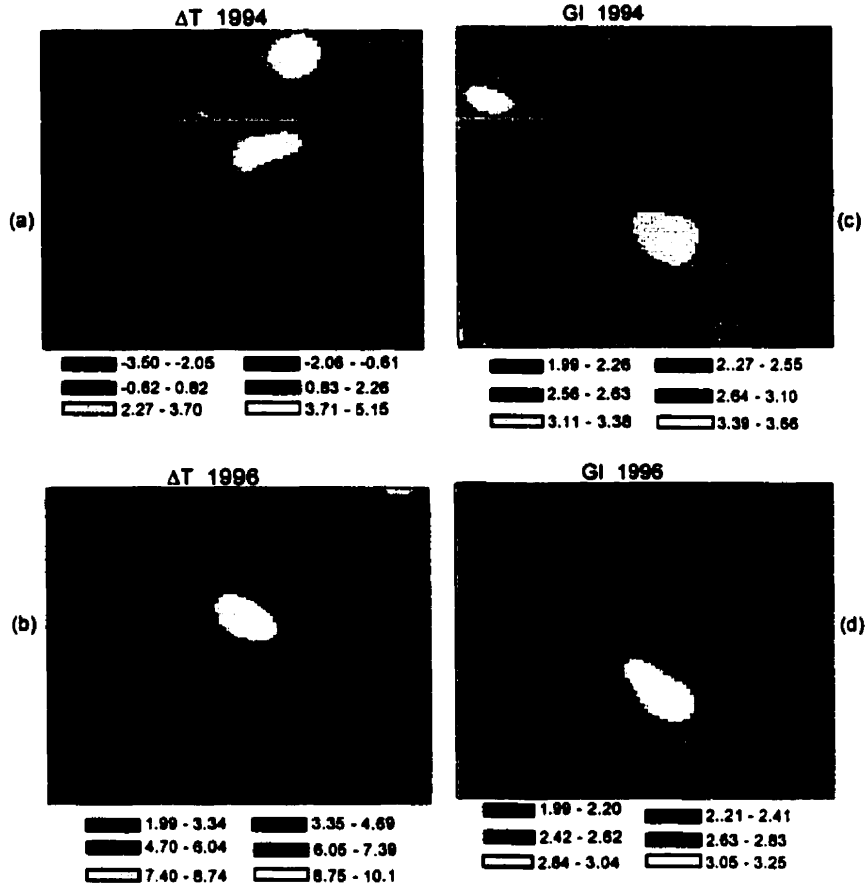

Figure 4.3 : Maps of surface minus air temperature, ΔT (°C) and greenness index (GI) at the SSA grid in 1994 and 1996

At the SSA (Figures 4.3a & b), the NW-SE diagonal separates the site into a warm area above the line and a cool area below it. The high ΔT around the middle of the site to the NE edge, corresponds to the logged and regenerating areas, while low ΔT values are associated with predominantly wet conifers interspersed with fen. The similarity and correlation coefficients between 1994 and 1996 maps are 0.92 and 0.90, respectively. The viewing angle problems with respect to observed ΔT have been addressed before [e.g. *Vining and Blad*, 1992], with low ΔT over the forested area explained by the fact that over partially

covered canopies, the radiance measured by the vertical radiometer is a combination of emissions from the top of the canopy and the underlying surface [*Sun* and *Mahrt*, 1995], which was cooler at the forested area than at the disturbed areas. There is some evidence for the expected inverse relationship between ΔT and GI, though the sharp distinction between the forested and the regenerating areas is absent from the GI maps.

There is higher persistence of GI patterns between the two years at the SSA site (Figures 4.3c & d; C_s and R, of 0.94 and 0.90, respectively) than at the NSA site (Figures 4.2c & d); C_s and R 0.84 and 0.64, respectively), partly associated with the rapid regeneration in the northern part of the burn area.

4.4.3 Flux maps

(a) Spatial distribution of fluxes

The NSA and SSA maps of C, H and LE are shown in Figures 4.4a-f and 4.5a-f, respectively. In the NSA grid, both 1996 and 1994 maps show high values of H over the forest, and comparatively low values over the regenerating former burn areas. Estimated C_s and r between the 1994 and 1996 maps of H are 0.84 and 0.5, respectively. In the SSA, the region of maximum H was more developed in 1994 than in 1996, extending from the NE edge of the site, over the disturbed and logged areas, and through the OJP site into the forested area west of the NW-SE diagonal. The low values in H occur at the SE corner, in the vicinity of the OJP and fen sites, and at the SW corner, where fens dominate the forest floor species. Comparison between 1994 and 1996 maps gives C_s value of 0.80 and R value of 0.43.

There are obvious similarities and differences in the C patterns for the NSA. The differences between the two maps include an increase in relative importance of the southern half of the grid for CO_2 absorption, consistent with changes in the GI maps, and a well defined pattern of low CO_2 absorption over the OJP in 1996. Estimated C_s and R for these maps are 0.34 and 0.23, respectively. The similarity between the C maps for the SSA (C_s=0.48 and R=0.52) is somewhat closer than that for the NSA, with a high-flux 'pocket'

(possibly linked to regenerating aspen from visual observation) along the E edge as a main area of difference. There is a good correspondence between the patterns of C and GI at the SSA.

The LE maps for the NSA show some features common to both years (C_s = 0.81), particularly the area with high LE at the SE corner. The SSA LE maps show fewer obvious similarities (but C_s is still 0.76). The significance of the observed differences in the spatial variation of the fluxes is discussed in section 4.4.3(f).

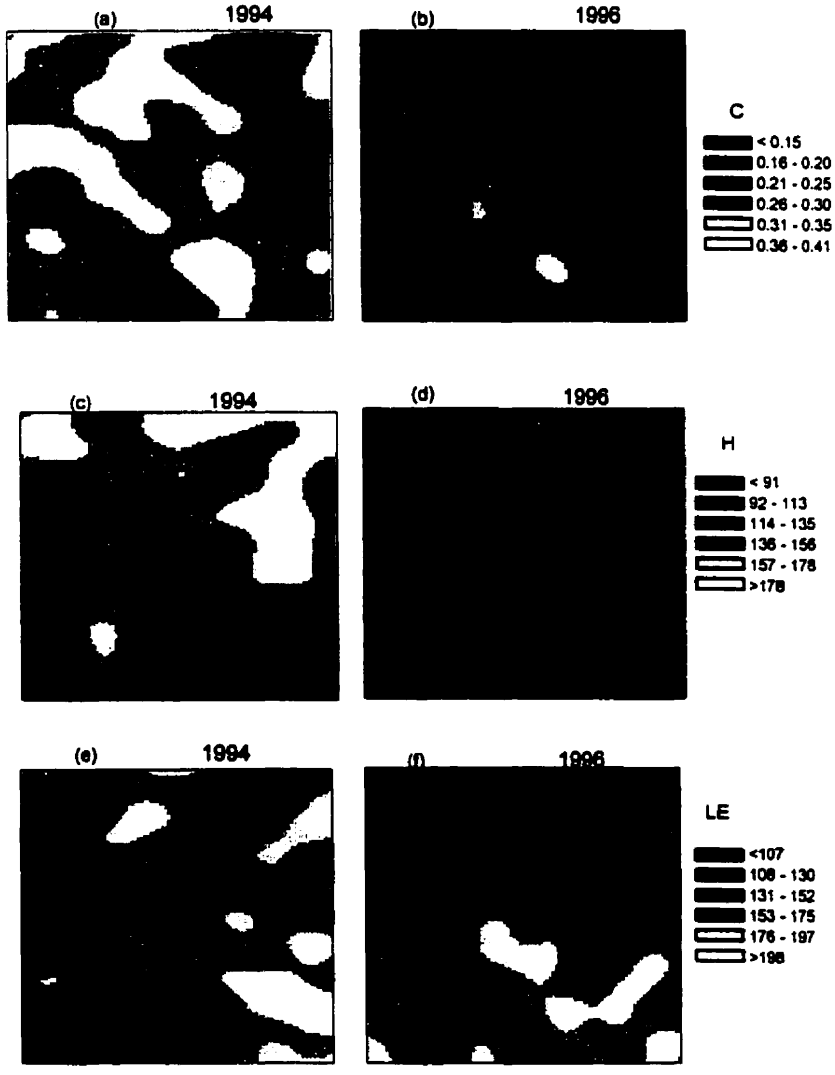

Figure 4.4 : Maps of CO_2 flux, C (mg m^{-2} s^{-1}), sensible heat flux, H (W m^{-2}) and latent heat flux, LE (W m^{-2}) at the NSA in 1994 and 1996

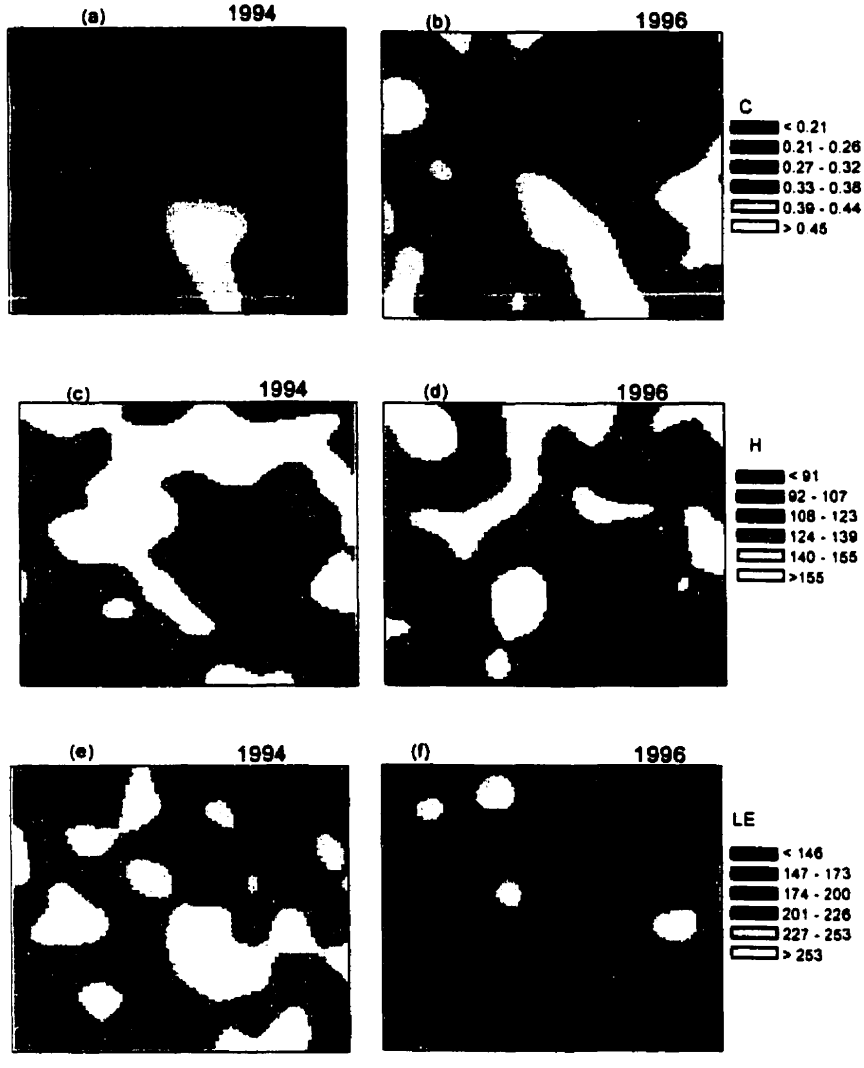

Figure 4.5 : Maps of CO_2 flux, C (mg m^{-2} s^{-1}), sensible heat flux, H (W m^{-2}) and latent heat flux, LE (W m^{-2}) at the SSA in 1994 and 1996

(b) Factors affecting flux variability

Where soil moisture is a limiting factor, its effects on surface fluxes can be dramatic [*Verma et al.*, 1995]. However, root zone moisture content is difficult to determine in heterogeneous terrain and information about it is rarely available. During BOREAS 1994, root zone moisture levels did not get low enough to exert a major control on the surface energy balance [*Sellers et al.*, 1995]. This is corroborated by the weak dependence of

photosynthesis on soil moisture found by *Baldocchi et al.* [1997] at the SSA OJP site. We will, therefore, base our discussion on the assumption that flux variability at the sites was primarily due to non-uniform distribution of the incoming energy, and the inhomogeneity of surface covers, which react differently to this incoming energy.

We attempted to quantify the relative importance of these two factors by comparing the coefficient of variation of the incoming radiation, V_r, against the coefficients of variation of the fluxes, V_l (for LE), V_h (for H), and V_c (for C). The coefficients for the fluxes showed noticeable differences between grid flights and little or no difference in the average values between the two years. At the NSA site, average values of V_l, V_h, and V_c are, respectively, 0.31, 0.27, and 0.30 for 1994; and 0.30, 0.27 and 0.32 for 1996. In the same order, the coefficients are 0.26, 0.27, 0.36 for 1994, and 0.37, 0.28 and 0.36 for 1996 at the SSA site. The reduced value of V_l at the SSA in 1994 is most likely associated with extensive precipitation across the site at the start of IFC-2, which would have reduced difference in evaporation due to variations in surface types (see discussion of Bowen ratio below). This means that except for LE at the SSA site, the biophysical differences at the sites between the two years were insufficient to significantly modify the source and sink configurations of the scalars. By contrast, incoming radiation was somewhat more uniformly distributed in 1996 than 1994, with average values of V_r 0.05 in 1994 and 0.10 in 1996 at the NSA, and 0.04 in 1994 and 0.12 in 1996 at the SSA. The values of the ratios V_l/V_r, V_h/V_r and V_c/V_r against V_r are plotted in Figure 4.6. (Given the small number of the data used, any relationship between the variables is more easily detected through their ratios). The best-fit relationship between the ratios and V_r shows an exponential decay with increasing V_r. The influence of radiation on the variability of the fluxes appeared greater in 1996 than in 1994, which is also corroborated by statistical tests (see below). From the values of these ratios (most of which are ≥ 5) it is apparent that surface inhomogeneity was more significant than radiation in inducing variability in the surface fluxes. This is not surprising given the fact that most of the flights were conducted under clear sky conditions.

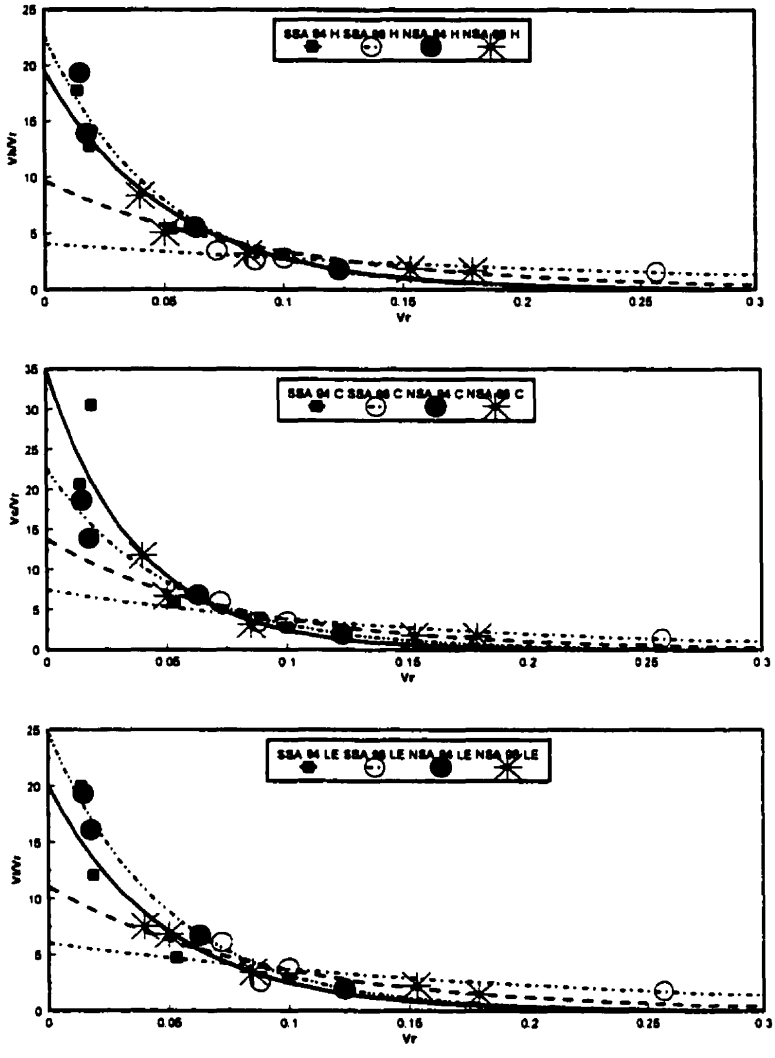

Figure 4.6 : The plot of the ratio of V_f/V_r against V_r

(c) Direct mesoscale fluxes

Vertical transport of scalars at scales greater than turbulent eddies may be an important component of the total surface flux. Transport by mesoscale motion is generally small at low observation levels, but can be important at the aircraft level of 30 m [*Sun* and *Mahrt*, 1994]. Furthermore, the partition between cool forests and warm disturbed areas at the grid sites and the associated variations in surface radiation temperature (10-15 °C) and air temperature (2.0-3.0 °C) are similar to those responsible for the mesoscale motions reported in *Segal et al.*, [1989], *Mahrt et al.*, [1994], and *Doran et al.*, [1995].

The influence of surface-induced mesoscale fluxes across the grid was examined by estimating mesoscale fluxes from segment averages and composited over repeated runs of a flight line. These line estimates, symbolized here as F_{ml}, are influenced by transient events such as changes in wind speed and cloud cover and showed significant variation across flight lines. Highest values of F_{ml} were associated with moisture transfer, and could be $\leq$ 20% of the turbulent fluxes. The mesoscale flux averaged over the grid, F_{mg}, is primarily related to surface heterogeneity, although it may still include some influence of nonstationarity. As expected, the observed value of F_{mg} were much smaller than those of F_{ml} and, for all the grid flights and flux types, F_{mg} did not exceed 10% of the turbulent flux, and was far less when composited over an IFC. The low observed values of the mesoscale fluxes at the site, even in the presence of a well developed gradient in surface thermal properties, especially at the NSA grid, suggest that the spatial scale of surface heterogeneity is not large enough to enhance mesoscale motion.

(d) Stability of flux map estimates

The flux maps presented above are from gridded data composited over four or more flights under similar weather conditions, with each grid line sampled twice per flight. We have examined the reliability of the maps, in the face of boundary layer variability, by analyzing the magnitude of variation in flux estimates obtained from six or more repeated passes of the Twin Otter under uniform radiation conditions, over the OBS site at the NSA. Flux averages over adjoining, non-overlapping 2-km segments produced five data points for each of the 10 km runs. Segment values were combined over two consecutive passes such that if N is the number of pairs of passes over M segments in the data set, F(m,n) can be considered as the segment averages along a grid flight line flown on N different days under the same conditions. The standard errors expected for each segment M, SE(m), is then estimated as

$$SE(m) = \frac{\sigma(m)}{\sqrt{N}} \qquad (4.3)$$

where σ(m) is the standard deviations of the pixels between flights, given as

$$\sigma(m) = \sqrt{\frac{1}{N-1}\sum_{n=1}^{N}[F(m,n) - \bar{F}(m)]^2} \qquad (4.4)$$

and the overbar is used to indicate average of F(m,n) over N.

Estimated average standard error, in percent of total flux, was 8.5 for H and 10 for LE and C. To demonstrate the impact of errors of this magnitude on the flux patterns, the flux map pixels for the 1994 NSA maps presented in the preceding section were then randomly perturbed by these error estimates, and the resulting matrix used to produce new maps. These maps, shown in Figure 4.7 must be compared to those in Figures 4.4a,c and e. It is interesting to see that the main features of the maps are unaffected by the perturbation. This suggests that the observed flux patterns are primarily a reflection of surface characteristics rather than boundary layer variability. The coefficients of similarity between the original and the perturbed maps are 0.88, 0.87 and 0.86 for H, LE and C, respectively.

(e) Effect of mapping scale on flux patterns

Scale is a crucial aspect of spatial heterogeneity. Shifts of scale, for an ecological entity, may lead from perceived homogeneity to heterogeneity, and vice versa. The sensitivity of the map features to mapping procedures were examined by comparing maps (not shown) produced from different data averaging windows, based on the 1994 NSA grid flights. Grid matrix data were created from 1 km and 2 km data windows without overlap between adjoining windows, and the resulting maps (X and Y respectively) were compared with those from 2 km windows with 1 km overlap (Z). For each of the variables no major difference in the map patterns was observed. The comparison of the summary statistics of the flux maps are given in Table 4.4, while Table 4.5 shows the correlation coefficient and coefficient of similarity between the maps. The maps resemble each other in patterns, as shown by the high coefficients, as well as in magnitude.

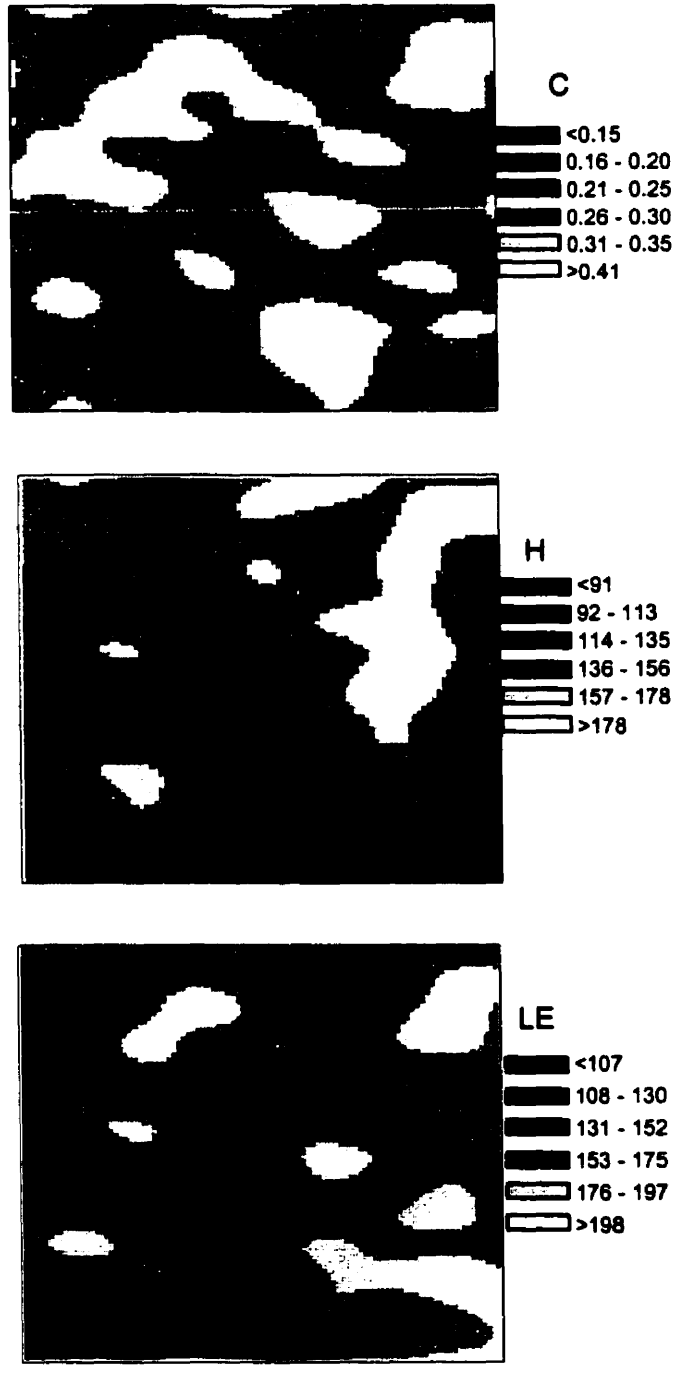

Figure 4.7 : Maps of (a) H, (b) C and (c) LE produced from perturbed gridded 1994 NSA data

Table 4.4. Summary statistics of flux maps produced from 1 km (X), 2 km (Y) and 2 km with 1km overlapping windows (Z).

	H			LE			C		
	X	Y	Z	X	Y	Z	X	Y	Z
Min.	80	89	78	79	83	82	-0.17	-0.20	-0.19
Max	223	221	192	226	226	229	-0.47	-0.48	-0.47
Avg.	150	149	150	164	163	163	-0.32	-0.32	-0.32
Std.	28	22	23	26	24	24	0.05	0.05	0.05

Table 4.5. Correlation coefficient (R) and coefficient of similarity (Cs) between X,Y and Z

	Correlation Coefficient			Coefficient of Similarity		
	R_{XY}	R_{XZ}	R_{YZ}	Cs_{XY}	Cs_{XZ}	Cs_{YZ}
ΔT	0.89	0.95	0.97	0.88	0.90	0.93
H	0.83	0.89	0.94	0.83	0.88	0.91
LE	0.70	0.85	0.89	0.75	0.85	0.90
C	0.70	0.86	0.90	0.79	0.84	0.92
GI	0.80	0.86	0.92	0.80	0.86	0.90

(f) Significance of the spatial variation

Two statistical tests, comparisons between the means and comparisons between the variances, were carried out to assess the strength of the differences in the spatial variation of the fluxes between the two years. All test were done at 5% significance level using *paired t-test* for comparison between the means and *F test* for comparison between variances.

At the SSA grid, the mean LE was significantly higher in 1994 than in 1996, but no significant difference was observed in the mean values of C and H between the years. The variability of LE was significantly higher in 1996 than in 1994, while the inverse is true of C, and the variability of H remained essentially unchanged. High moisture availability probably accounts for the high values but low variability of LE in 1994, associated with the

heavy rainfall just prior to IFC-2 in 1994 (see section 4.4.4a), which reduced moisture stress at the transpiring surface and horizontal moisture gradients across the grid. The non limiting moisture condition, combined with the plentiful available energy, enhanced evaporation rates from the wet canopy to approach and exceed potential rates of evaporation [*Baldocchi et al* , 1997]. The lower variability in C in 1996 probably reflects the increasing strength of CO_2 uptake by regenerating (particularly deciduous) plants at that site.

At the NSA grid the values of H, LE and C were found to be statistically different between the two years, with the means significantly greater in 1994 than in 1996. The spatial variability in H was significantly greater in 1994, while that of C was greater in 1996, and no significant difference was observed for that of LE. The high variability in the 1996 C data may be attributed to the pronounced gradient in the CO_2 uptake between the regenerating plants and the more mature forests stands.

4.4.4 Energy Partitioning

(a) Bowen Ratio

Estimated grid averaged Bowen ratio (β=H/LE) gave higher values at the NSA than at the SSA, especially in 1994. The composite averages of β at the NSA were 0.92 in 1994 and 0.75 in 1996, compared to 0.62 and 0.70, respectively, at the SSA. As shown in Figure 4.8, the NSA distribution of β gives lowest values (0.45-0.70) over the regenerating areas and highest values over the mature forests, with local maxima (1.20-1.45) over the Old jack pine and Old black spruce. The high values of β over the forests have been attributed to significant stomatal control by mature vegetation [*Sellers et al.*, 1995]. The development of areas with lowest values from a localized spot at the SE corner of the site in 1994 to a well developed belt cutting across the regenerating area in 1996, agrees well with the observed changes in the relative distribution of GI between the two years. This is probably due to the presence of growing and young transpiring plants that have visually appeared to have increased in density in the area over the time interval. The difference in magnitude of β between 1994 and 1996 at the SSA is largely attributed to differences in surface wetness and

- to a much smaller degree - to changes in energy partitioning at the surface. The first grid flight in 1994 at the SSA was preceded by heavy precipitation (62 mm of rainfall on July 19) which, coupled with the above normal July rainfall recorded at the site (165 mm compared to climate normals which ranged from 66-87 mm), produced high soil moisture that favoured low values of β.

The magnitude of β is known to be related to the depth of the boundary layer [*Avissar and Pielke*, 1991], i.e., the higher β, the greater the warming rate of the lower atmosphere, and hence the growth and depth of the mixed layer. In 1994, as might be expected, the higher value of β at the NSA, compared with that from the SSA, corresponds to the higher boundary layer depth over the NSA (Table 4.3). However, this was not the case in 1996, where averages and ranges of the Bowen ratio over the NSA and SSA were comparable in magnitude, while boundary layer depths were still higher at the NSA than the SSA, suggesting a more complex link between Bowen ratio and boundary layer heights under our experimental conditions.

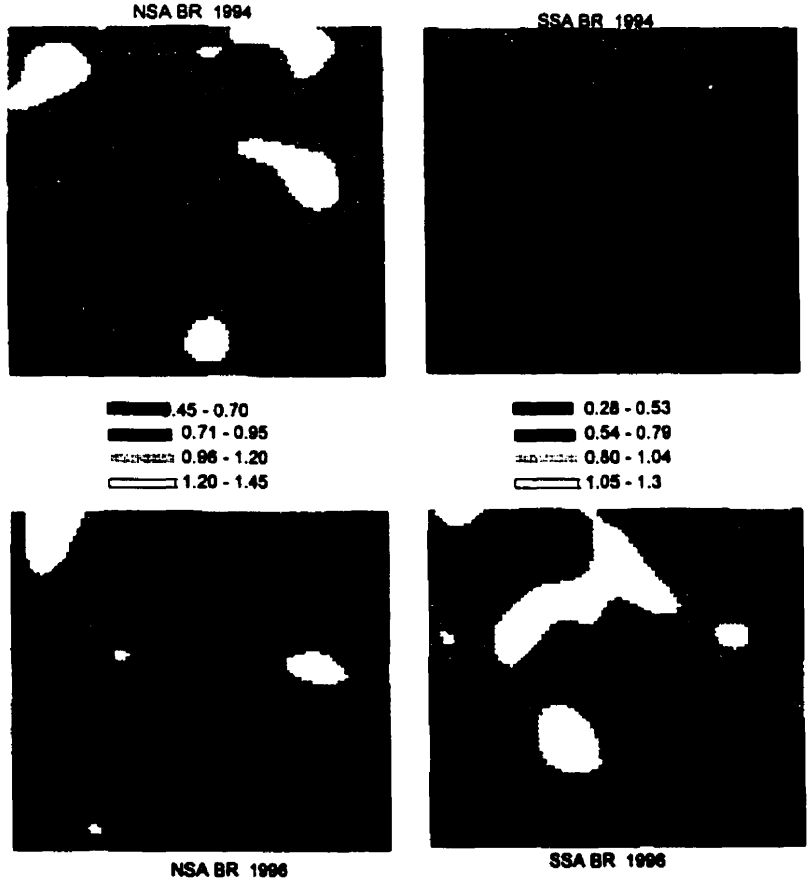

Figure 4.8 : Maps of Bowen ratio (β) for the NSA and SSA in 1994 and 1996

(b) Surface energy balance closure

The energy balance equation at the sites, in the absence of horizontal advection, is

$$R_n - G = H + LE \tag{4.5}$$

where G is the sum of the minor energy balance terms (ground flux and storage). The fractional surface energy balance closure can then be represented as

$$\delta = \frac{H+LE}{(1-\kappa)\,R_n} \tag{4.6}$$

where κ is the ratio G/R_n. Reliability in the determination of δ depends on the degree of error associated with the estimation of κ, which requires a network of point measurements at homogeneous subareas in a heterogeneous environment. By integrating the values of κ for the different surface covers at the NSA and SSA in 1994, *Barr* and *Betts* [1997] obtained identical lower (0.17) and upper (0.23) estimates of the mean κ value for both study areas. To examine the spatial distribution of δ, we used the average of these limits (0.20) in Eq. (4.6), which we assumed to be representative for the grid areas, and further assumed that κ remained constant between 1994 and 1996. The resulting composite grid averaged values of δ were somewhat higher at both sites in 1994 (0.80 at SSA and 0.77 at NSA) than 1996 (0.73 at SSA and 0.71 at the NSA), with a range from 0.57 to 0.96. The distributions lacked the distinct patterns produced by surface temperature and more closely resembled those of LE, but local maxima occurred over the old black spruce and old jack pine at the NSA. Local maxima were observed at the SSA over the disturbed areas.

A value of δ lower than unity implies underestimation of the aircraft measured H+LE. The failure of the eddy correlation to close the energy balance was not unique to the Twin Otter. Similar underestimation of flux was reported by other BOREAS flux aircraft and at the BOREAS flux towers [*Desjardins et al.*, 1997; *Dobosy et al.*, 1997]. Using eddy

correlation over a Douglas-fir stand, *Lee* and *Black* [1993] obtained values of δ that varied from 0.66 to 0.88, with an average value of 0.74. The underestimation of H+LE by eddy correlation has been attributed to factors such as a loss of longwave contributions to the eddy flux [*Kelly et al.*, 1992], flux divergence near the surface [*Lenschow and Delany*, 1987] and significant mesoscale transfer [*Betts et al.*, 1990; *Sun and Mahrt.*, 1995], neither of which is significant in this case. In general, the observation that the overall measured fluxes of sensible heat and latent heat may not balance the available energy locally is not unexpected over heterogeneous surfaces, where small-scale advection may prevent closure by vertical fluxes and local storage terms. However, it is difficult to see how such effects could lead to systematic underestimation in H and LE estimates. More likely, such underestimation would be expected to be associated with large-scale advection and/or underestimated storage terms in the warming of often waterlogged near-surface layers. Analysis of grid flight data showed no evidence for persistent gradients in temperature or moisture in the along-wind direction, but average radiometric surface temperatures between the first and last grid line (flown 2 hrs apart) differed typically by about 4 degrees in the NSA grid and 2 deg in the SSA grid. This indicated a warming up of the surface at a rate of 1 to 2 degrees per hour. Combined with the fact that the near-surface frozen soil is melting at this time of year, this suggests that the ground flux may have been significantly underestimated, leading to expectation of a κ values in excess of 0.2. However, considering that there is little evidence that any of the factors mentioned above were more significant in one year than the other, we assume that errors in the energy balance will have little effect on our analysis of relative spatial distributions between the two years.

4.6 Conclusions

Spatial and temporal variations in the surface fluxes of heat, (H), moisture, (LE), and CO_2, (C) were examined by comparing the 1994 and 1996 airborne data obtained at the two 16 km x 16 km BOREAS grid sites. A sensitivity test showed that the dominant features of the composite flux maps used in our study are relatively insensitive to boundary layer variability. A comparison of the coefficient of variation of the fluxes with those of available

energy showed that variability in surface fluxes at the site was associated more with heterogeneity of the surface cover than with variations in available radiant energy. Analysis of the maps indicated some noticeable changes in the biophysical properties of the surface covers over the two year period, but the changes were not enough to significantly modify the source and sink configurations of the scalars that were examined. The maps of surface characteristics showed greater similarity in spatial patterns between 1994 and 1996 than the flux maps. Spatial distributions of C showed the highest variation between the two years, especially in the NSA, where a southward shift in greenness matched a similar shift in CO_2 absorption.

Correlation between greenness index, GI, and C was significant in both years (R values typically between 0.6 and 0.8), and higher at the SSA than NSA. The significant values of H in spite of a low surface temperature excess over the forest, and the resulting decoupling between ΔT and H (R values < 0.2, negative at the NSA and positive at the SSA), was also observed in both years. The high Bowen ratio over the forest, attributed to physiological control of the stomatal opening of plants, should favour the development of deep boundary layers over the forests. However, we could not establish, on the basis of our observations, a clear relationship between boundary layer heights and flux characteristics.

This study underlines the importance of the role of the surface mosaic in forest-atmosphere exchange. It is hoped that the observations reported here will provide clues and reference points for the development and validation of surface-vegetation-atmosphere models over the BOREAS landscape, including those based on remote sensing observations. They should convey to the potential user our estimates of the confidence limits applicable to the given maps when used as "test patterns" for high-resolution modeling, and caution against oversimplification in the assumption of relationships between radiometric surface features and energy or gas exchange, which appear to be site- and time specific. To what degree the use of more refined surface descriptions (currently under development) may help to elucidate the parameters that define such relationships, remains to be seen.

CONNECTING STATEMENT BETWEEN CHAPTER 4 AND 5

In Chapter 4, the spatial and temporal variations in the measured fluxes at both grid sites were compared. The comparison showed evidence of land cover changes, primarily changes in the proportions of regenerating plants within the grids between the two years. These changes were not significant enough to alter the main source and sink configurations of the scalars. The study confirmed the dependence of the fluxes on the species composition of the land cover. In the next chapter (Chapter 5) attention will be focused on establishing relationship between the fluxes and the cover types found within the flux footprint. The goal is to obtain an expression from which flux estimates could be made simply from the fractions of cover types, an essential step in scaling up from local to regional observations on the basis of remote sensing observations of surface characteristics.

Some of the results given in Chapter 5 were presented at the 23rd Conference on Agricultural and Forest Meteorology of the American Meteorological Society, Albuquerque, New Mexico, November 2-6, 1998.

CHAPTER 5

CORRELATION BETWEEN SATELLITE BASED LAND COVER TYPES AND AIRBORNE MEASUREMENTS OF LATENT HEAT, SENSIBLE HEAT AND CO_2 FLUXES IN BOREAS.

5.1. Abstract

The previously described airborne observations included flux measurements of CO_2, sensible heat and latent heat. In this chapter, an attempt is made to establish quantitative relationships between the airborne observed fluxes at two heterogeneous grid sites at the Northern Study Area (NSA) and Southern Study Area (SSA), and the cover types within the flux footprint. To this purpose, the satellite observations bands 1 through 5 and band 7 of the Landsat TM scene of the study areas were acquired, and were used to produce the land cover classification of the study areas. Using a footprint function developed from tracer gas release experiments in the boreal forest, the fractions of cover types within the footprint were determined, and used in a regression analysis against the observed fluxes. The results showed that, depending on the flux types, as much as 80% to 92% of the variations in the fluxes were explained by the cover types that contributed to them. Model validation using a set of independent data showed high correlations between the observed and predicted estimates. The study provided a first step in extrapolating areally averaged fluxes from local to regional scales, based on land cover characteristics.

5.2. Introduction

Remotely sensed data are a logical source of information related to spatio-temporal variation of land surface properties. Although surface fluxes cannot be directly estimated from remotely sensed data alone, this data source does provide excellent information on spatial variability in land surfaces and, by extension, in surface energy balance. For example, because vegetation indices such as the normalized difference vegetation index (NDVI), greenness index (GI) or simple ratio (SR) are related to surface state variables such as vegetation structure and density, they are also generally indicative of

important land surface variables with potential impact on climate, such as leaf area index and canopy resistance [*Avissar et al.*, 1986; *Sellers et al.*, 1992; *Townsend and Justice*, 1995]. In addition, surface radiative temperature T_s reflects the combined effects of surface energy balance, atmospheric state, and the character of the local land surface [*Diak* 1990; *Carlson et al.*, 1995; *Norman and Becker*, 1995]. The combined use of these remotely sensed variables has been widely suggested as a possible mechanism for land surface energy balance inversion modeling from satellites [*Goward and Huemmrich*, 1992; *Nemani et al.*, 1993]

Numerous investigators have examined the use of remotely sensed data to infer surface sensible heat flux on a regional scale. For land surfaces composed of either dense vegetation or bare soils, remote-sensing-based land surface energy balance models have been shown to estimate surface energy balance components with reasonable accuracy [*Kutsas et al.*, 1989; *Diak*, 1990; *Abareshi and Schuepp*, 1998]. Over areas with incomplete canopy cover, however, less satisfactory results have been reported. This is because observations made over such areas do not support the assumption of coupling between sensible heat flux and radiative temperature, which is the basis for the development of these models. Preliminary results from the analysis of the grid flight data [*Ogunjemiyo et al.*, 1997 & 1998; see also the Appendix] revealed a poor agreement between the aircraft-based estimates of sensible heat flux and surface radiative temperature, and also between these flux estimates and those obtained from satellite derived surface temperature. This is mainly attributed to the viewing angle problem of the radiometer, a problem that was also identified by *Hall et al.* [1992], and *Sun and Mahrt* [1995].

Vegetation, climate, soil and topography together define land cover. Because land cover represents the combined result of these component parts of the landscape, some form of relationships should be expected between it and airborne measured fluxes of sensible heat, latent heat and CO_2. The development of a land cover based model from which surface fluxes could be estimated will provide an alternate procedure to flux estimation based on remotely sensed surface characteristics, which have been shown to give inconsistent results. No work has been done in this area for complex, heterogeneous terrain, due to the specific requirements for establishing a relationship between fluxes and land cover: (a) high-resolution land cover data, which are rarely available; (b) large scale flux measurements,

which are difficult to execute; (c) flux density measurements of the cover types, which are difficult to accomplish especially in a heterogeneous area; and (d) a mechanism for delineating the cover types that contribute significantly to the measured flux.

The methods of data acquisition in BOREAS were designed to meet some of these problems. The project produced Landsat TM based land cover data of the BOREAS study areas, and airborne flux data of the area on a regional scale. The development of the footprint concept (see section 5.4 and 5.5.2) provided a refined method for relating eddy fluxes to areas upwind of the measurement platform. A footprint function for the BOREAS grid sites was developed by *Kaharabata et al.* [1997]. It is used on the land cover and flux data to establish relationships between the land cover types within the grids and the observed fluxes of heat, water and CO_2. With these tools, the main question to be addressed in this chapter is: How much information about the fluxes can be infrared from the distribution of the cover types, as described by the land classification data of the study sites? The subject is approached by using multiple regression analysis. The objective of this regression analysis was to establish relationships between the airborne measured fluxes and the cover types that contributed to the flux. The main goal was to obtain a set of regression equations, from which flux estimates can be deduced from the fractions of cover types that were within the flux footprint, under the given meteorological conditions.

5.3 Data Description

5.3.1 Land Classification Data

(a) Data sources and image projections

The description of the cover types used the land classification maps based on Landsat TM derived data, and species abundance maps derived from videographic information obtained by the Twin Otter aircraft. The TM based imagery in BOREAS was classified with two classification schemes by the Terrestrial Ecosystem (TE-18) team and one by the Remote Sensing Science (RSS-15) team. These data sets are henceforth identified as TE-1, TE-2 and RSS, respectively. The data set from the videographic information is identified as

VDD. TE-1, TE-2 and RSS images were obtained from the BOREAS Information System (BORIS) database. They were stored in the BOREAS grid projection based on the ellipsoidal version of the Albers Equal Area Conic Projection (AEAC). The projection has North American Datum of 1983 (NAD83), Geodetic Reference System of 1980 (GRS80), standard parallels of 52° 30' N and 58° 30'N and a lower left origin of 51° N and 111° W. The spatial coverage of TE-1 and TE-2 for the NSA, and TE-1 for the SSA was approximately 129 km x 86 km, and TE-2 for the SSA covered an area that was approximately 144 km x 114 km. The RSS imagery covered a smaller area, but large enough to encompass most of the tower sites and the Twin Otter grid sites. Each pixel in the images represents a 30-meter by 30-meter area on the ground. Subsets of the images, representing the 16 km x 16 km TO grid site were produced from the bigger images and georeferenced into a latitude and longitude reference system in a GIS software (IDRISI).

TE-1 and TE-2 classifications were based solely on TM data, while a combination of Shuttle Imaging Radar-C (SIR-C) and TM data were used for RSS classification. The TM imagery scene consisted of bands 1 through 5 and band 7 with Path 33, Row 21 for the NSA, and Path 37, Row 22-23(shifted) for the SSA, in the Landsat Worldwide Reference System (WRS). The solar elevation angle at the time of image acquisition was 40.1 degrees. The solar azimuth angle was 146 degrees. The scene for TE-1 data set was acquired on August 20, 1988 for the NSA, and on August 6, 1990 for the SSA. For TE-2 data set, the imagery scene was acquired on June 21, 1995 for the NSA, and September 2, 1994 for the SSA. The scene for RSS data set was acquired on September 2, 1995, and on April 13, 1994 for the NSA. The videographic information of the forest cover, which was used for VDD classification, was obtained during the grid flights flown in 1996. Video images of the cover types were made during the flights using a downward looking camera that was installed under the aircraft nose, tilted at a 30 degree angle to the horizontal. A global position satellite (GPS) system was integrated into the recording system to provide on-screen time, altitude, latitude and longitude.

(b) Classification methods and cover classes

The standard maximum likelihood supervised classification technique was adopted in classifying TE-1 and RSS. For TE-1 classification, forest cover maps of the area, which included species composition for various stands, were acquired to identify and select training fields for various land cover types. Statistics were derived from these training sites and used to classify the image. Pixels that did not fall into any of the classes using maximum likelihood were classified using a minimum distance classifier. A detailed description of the data and the procedure used to classify RRS data are given by *Ranson et al.* [1997], who identified training set locations on the images for forest and nonforest classes. GPS-derived site coordinates and aerial photography were used to determine site location. Spectral signatures were extracted from the transformed images and used as inputs for the classifier to produce a forest type map. The technique used to produce TE-2 classification is described in *Hall et al.* [1997]. In this technique, end member reflectances of canopy, background, and shadow are used with a geometric canopy model to compute simulated pixel reflectances for increasing amounts of canopy cover. These simulated reflectances can be plotted as a continuous trajectory for each class (e.g. wet conifer, deciduous, etc.) from 0% to 100% canopy cover. The imagery pixels were classified based on their proximity to the trajectories, with the pixel being assigned to the class of the closest trajectory.

VDD classification was made by estimating species abundance based on the information derived from viewing the video tape of the grid forest landscape. The video tape was viewed on a television screen. At every five seconds the tape was paused, and information about the latitude, longitude and the abundance of each recognised vegetation class was recorded. The combined East-West and North-South oriented flights produced adequate data that were stored in a vector format. For each cover type, a map was made by distance-weighted interpolation of its species abundance data, according to the expression

$$\hat{Z}=\frac{\sum_{i=1}^{i=n}\frac{1}{d_i^p}Z_i}{\sum_{i=1}^{i=n}\frac{1}{d_i^p}} \qquad (5.1)$$

where $\hat{Z}$ is the interpolated Z-value (species designation), d is the distance from known point i, n is the number of points to be included in the search (six on average), and p is the distance weight exponent taken to be 2. The maps for all the cover types were integrated using the MDCHOICE module in the IDRISI GIS software to produce a land cover map for the grid.

(c) Sources of error in the classifications

Similarity in spectral signatures of different species, variations in tree density, and spectral mixing of various features that fall within a 30 meter pixel are considered as the major sources of error in the TM based data. In the TE-1 classification, it was possible in some areas that regenerating conifer can be confused with fen, depending on canopy density. Also, age classes within the deciduous or conifer classes can be confused because of minor variations in background. In the RSS classification, sources of error include natural stand variations, measurement errors due to radar backscatter from atmospheric particles, and location errors. In addition, this classification does not explicitly deal with mixed forest classes. Mixtures of conifers and aspen species are common in the boreal forest and are a potential source of error for forest classification.

Several factors were recognised as possible sources of error in VDD classification. One possible limitation of the approach is the subjectivity in the identification of the vegetation types and density of cover. It was often hard to distinguish between shrubs and small trees, and the definition of a shrub was likely different whether it was surrounded by herbs or by large trees. Variation in the brightness of the video due to changes in the orientation of the sun may also have affected the perception of the different tree species.

5.3.2 Aircraft-Based Data

The aircraft based data were acquired in 1994. The data were collected by the Twin Otter aircraft in a grid pattern, flown at an approximate altitude of 30 m agl at a mean air speed of 60 m s^{-1}, as described in Chapter 3 of thesis. Each grid flight consisted of nine parallel straight lines, spaced two km apart, with each line sampled twice in a time-centered sequence. Flight trajectories (East-West or North-South) were chosen for closest approach to crosswind conditions. Detailed descriptions of the data, including the weather conditions

under which the flights were flown, are given by *Ogunjemiyo et al.*[1997, 1998] and *MacPherson et al.*[1997] (see Chapter 3).

5.4 Data Processing

Vertical turbulent fluxes of sensible heat (H), latent heat (LE) and CO_2 (C) at the flight level were computed from the time averaged covariance between fluctuations of the vertical wind and the scalar of interest. The flux events were averaged over 2 km data windows along each of the runs, and the segment values averaged over the two repeated passes of each of the grid lines, creating a matrix, F_{ij}, of 72 data points per grid . We may then assume that the segment averaged fluxes are due to flux density contributions from all the cover types within the flux footprint, i.e.,

$$F_{ij} = \sum_{k=1}^{k=K} \psi_{ijk} d_{ijk} \tag{5.2}$$

where d_{ijk} is the spatially averaged flux density and ψ_{ijk} the weighting function for cover type k in segment i of grid line j. The parameter d_{ijk} is difficult to measure even in a homogeneous area because of its dependence on ecophysiological factors and biophysical properties of the cover types. In the absence of independent information on this parameter, a relationship was developed between F_{ij} and ψ_{ijk} through a multiple regression model of the form

$$F_{ij} = \beta_o + \beta_1 \Psi_{ij1} + \eta_1 \Psi_{ij1}^2 + ... + \beta_k \Psi_{ijk} + \eta_k \Psi_{ijk}^2 + \epsilon \tag{5.3}$$

where β is the coefficient for the linear term, η the coefficient for the quadratic term for each of the independent variable, and ϵ the error associated with this model. Estimated values of ψ_{ijk} were checked for possible colinearity or multicolinearity. A backward elimination procedure was adopted in selecting the best model. This procedure of selecting variables for inclusion in the regression model starts with all independent variables in the model and then eliminates those variables that do not make any significant contribution to prediction.

Meteorological variables were purposely excluded from this regression analysis, not only because meteorological conditions were similar within the data base for each IFC, but in order to highlight the role of surface cover on spatial flux distribution.

The definition of the distributions of surface characteristics within the upwind footprint is based on the consideration of rows of 30 m pixels perpendicular to the flight track. If α_x is the weight given to the pixel at upwind horizontal distance x from the pixel corresponding to the flight path (x=0), and I_{xmk} is an indicator for the presence or absence of cover type k for the pixel at distance x and row m on the cover map, then

$$\psi_{ijk}=\frac{1}{P}\sum_{m=1}^{m=P}\sum_{x=0}^{x=X} I_{mxk}\alpha_x \tag{5.4}$$

where P is the number of rows in the segment, X is the maximum upwind extent of the footprint which contributes 98% of the measured flux. The value of I_{mxk} is 1 if cover type k is represented by the pixel at distance x and column m, otherwise I_{mxk} is 0. The weight of the pixels, α_x, was determined from the flux footprint function (FP) developed for the grid sites by *Kaharabata et al.* [1997], i.e.,

$$\alpha_x = \frac{\int_{x_n}^{x_{n+1}} FP\,dx}{\int_{x=0}^{x=X} FP\,dx} \tag{5.5}$$

where x_{n+1} and x_n are up- and downwind distances, respectively, of the pixel in the nth column, and the integrations were done numerically.

The stability component in the FP was represented by the Monin-Obukov length, L(m), which was estimated as

$$L = -\frac{u_*^3}{k\left(\frac{g}{T}\right)\left(\frac{H}{\rho C_p}\right)} \tag{5.6}$$

where k is the von Karman constant (0.4), T is the air temperature (K) at the aircraft height, H is the sensible heat flux in (Wm^{-2}), ρ is the air density ($kg\ m^{-3}$), g is acceleration due to gravity (9.8 $m\ s^{-2}$), and C_p is the specific heat (1005 $J\ kg^{-1}K^{-1}$). The friction velocity, u_* ($m\ s^{-1}$) was estimated according to *Stull* [1988]

$$u_* = [\overline{u'w'}^2 + \overline{v'w'}^2]^{\frac{1}{4}} \tag{5.7}$$

where u',v'w' are the fluctuations of the the x,y and z components of the wind in $m\ s^{-1}$.

5.5 Results And Discussion

5.5.1 Comparison Between the Classifications

The land cover maps for the NSA and SSA grids are shown in Figures 5.1 and 5.2, respectively. As seen from the maps, TE-1, TE-2, RSS and VDD classify the grid sites into 11,13,7 and 9 cover types, respectively. The TE-1 and TE-2 maps have seven identical classes, (see their descriptions in Table 5.1 and 5.2) and the main difference between them is in the subdivision of the regeneration classes, which is more refined in TE-2 than in TE-1. This difference may be more likely due to the year of data acquisition than to the classification techniques. The seven years separating the two data sets at the NSA, and four years at the SSA, may have produced phenological changes in the vegetation, as well as other temporal differences due to clear cutting and other man-induced change, making it possible to distinguish between regenerating conifers and deciduous.

The description of RSS classes is given in Table 5.3. The spruce, pine and shrub classes are similar to conifer (wet), conifer (dry) and the regeneration classes in TE-1 and TE-2. The RSS classification is differentiated from others by the absence of a mixed conifers (spruce and pine) or mixed trees (conifer and deciduous) class, which were known to be present at the sites. This appears as the main weakness of this classification. VDD maps, classifying the study area into nine cover classes, are presented mainly to examine the potential of using videographic information for classifying surface cover.

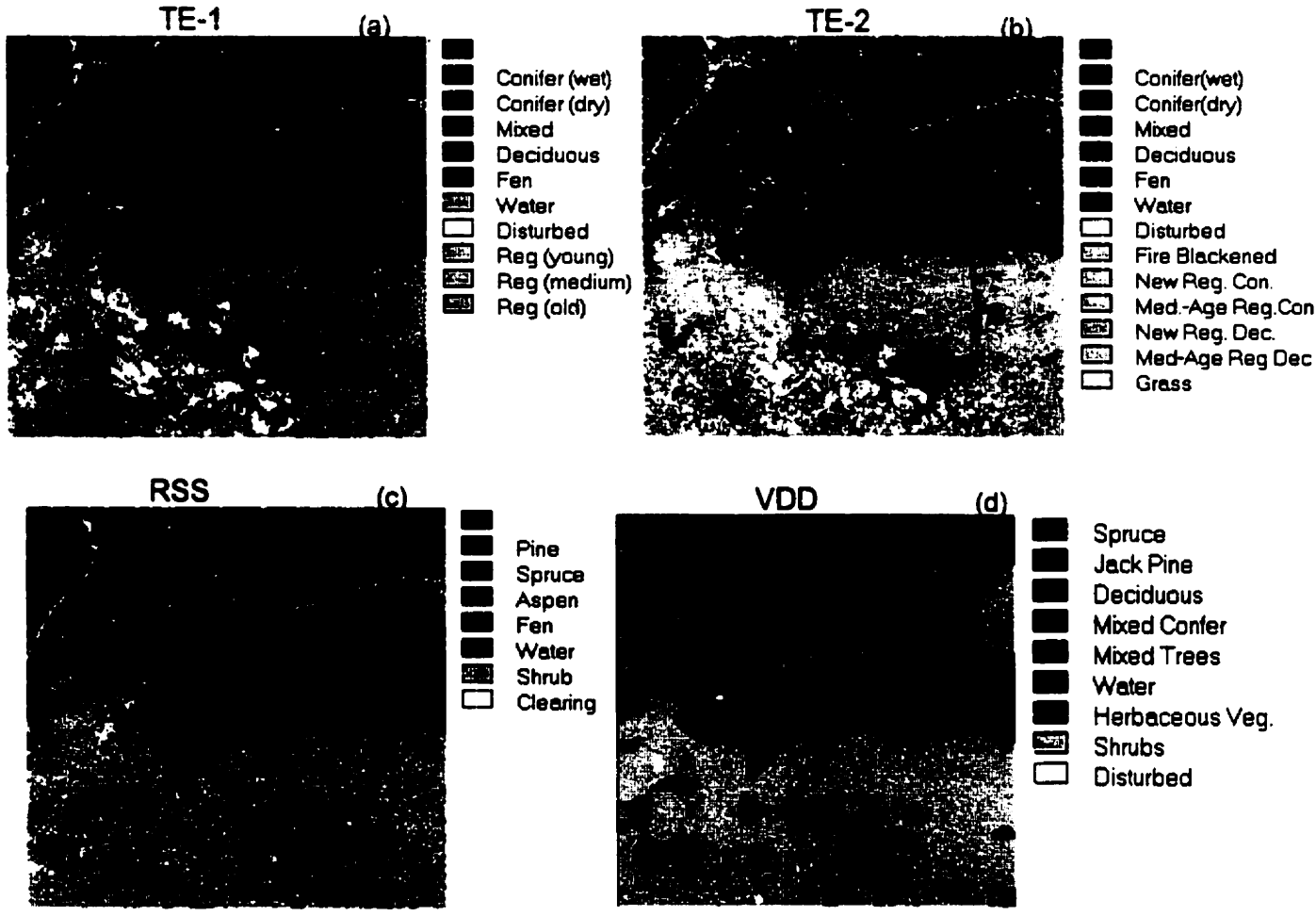

Figure 5.1 : Cover maps for the NSA grid based on (a) TE-1, (b)TE-2, (c) RSS and (d)VDD classifications

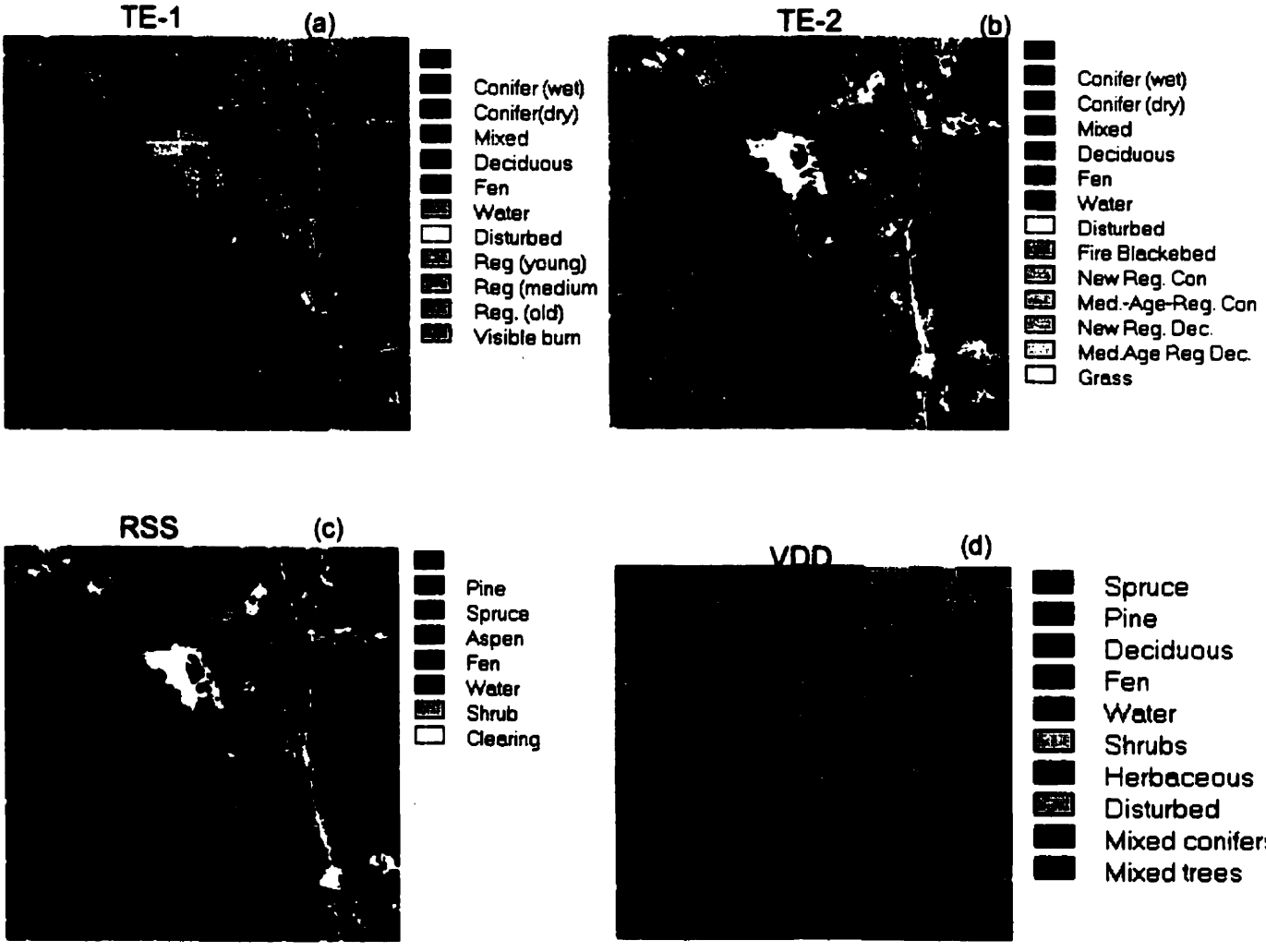

Figure 5.2 : Cover maps for the SSA grid based on (a) TE-1, (b)TE-2, (c) RSS and (d)VDD classifications

Despite the different classification methods with their associated errors, and the variation in the class definitions, some noticeable agreements can be observed in the vegetation distribution pattern. For example, at the NSA grid the maps show a well defined contrast in biophysical properties between the northen half and the southern half. The southern half exhibits the signature of an area recovering from fire events. The area is dominated by regenerating plants, mainly deciduous (aspen), which are interspersed with bare soils and rock outcroppings. In the center of this area is a pocket of unburned mature stands. On the other hand, the northern half of the grid is typical of a mature temperate forest, i.e. tall conifers with closed canopy. The species in this area occur in mixtures, and in patches of pure stands, as is the case with the jack pine and black spruce. The most distinct distribution patterns common to all the SSA maps are the occurrence of fen at the SW quadrant of the grid, the cluster of deciduous patches along the NW-SE diagonal, the regenerating areas and jack pine that are confined to the north of the diagonal, and the black spruce which appears to be everywhere in the grid, but with highest concentration in an elongated strip below the diagonal.

The major discrepancy between the maps is evident from the comparison of the percentage composition of their classes. For example, at the NSA grid the composition of regeneration class varies from 24% in TE-1 to 52% in TE-2; the fen class varies from 0 in VDD to 14% in TE-2, and the spruce or conifer (wet) class varies from 3.3% in TE-2 to 37% in TE-1. There is better agreement between the maps at the SSA than the NSA.

5.5.2 Footprint Function and Estimates

Over heterogeneous terrain, the turbulence characteristics may not be in equilibrium with the local surface but will reflect the conditions some distance upwind. This problem is particularly relevant in the case of flux observations and flux mapping by aircraft. In order to relate aircraft measured fluxes to satellite derived vegetation indices or cover types, it is therefore important to identify the areas (pixels) upwind that actually contributed to the fluxes, i.e. the flux footprints. Flux footprint have been studied extensively [*Leclerc* and *Thurtell*, 1990; *Schuepp et al.*, 1990 & 1992; *Horst and Weil*, 1992 & 1994; *Schmid*, 1994; *Baldocchi*, 1997; *Kaharabata et al.*, 1997; *Amiro*, 1998].

Table 5.1 Description of cover classes based on TE-1 classification.

Image Value	TE-1 classification	Description
1	Conifer wet	an area that contains coniferous trees, dominated by Black spruce (*picea mariana*) or Jack pine (*pinus banksiana*) growing on peat or poorly drained mineral soils.
2	Conifer dry	a well drained area with sandy soils that contains coniferous trees, primarily Jack pine, with a lichen (*cladina*) background.
3	Mixed	areas that contained coniferous and aspen/birch (*poupulus tremuloides/betula papyrifera*) trees, with the dominant species less than 80%
4	Deciduous	contains primarily aspen/birch, with composition greater than 80% deciduous trees
5	Fen	Fen/Bog class is characterized by areas with a water table very near or at the surface
6	Water	water bodies such as ponds, lakes and streams
7	Disturbed	areas such as roads, urban centers, that are dominated by bare soil, recently logged areas, or rock outcrops
8	Regeneration (Young)	areas that have been logged or burned but have been regenerating or regrowing for 3 to 8 years since the disturbance and can contain aspen or jack pine replanted following logging
9	Regeneration (Medium)	areas that have been burned or in some cases logged. These areas have typically been regrowing for up to 7 to 8 years since the disturbance and are usually immature or jack pine
10	Regeneration (older)	areas that burned and have been regenerating for about 12 to 20 years, and has features indicating the area is becoming recognizable as deciduous vegetation
11	Recent Burn	this class consists of aspen that is starting to regrow after being burned or cleared

The footprint model used in this study [*Kaharabata et al.*, 1997] was based on a tracer gas experiment conducted at the sites, and had input parameters which include: the Obukhov Length, L, friction velocity u_*, roughness length, z_o and the displacement height, d. The sensitivity test of the model by *Kaharabata et al.*[1997] showed the model was less sensitive to u_* than to z_o, such that less than 1% average difference was observed in the footprint for changes in u_* from 0.53 m s^{-1} to 1.0 m s^{-1} for both neutral and unstable stratification, while the footprint was found to increase fairly uniformly by about 23% for the unstable and 17% for the neutral case as the roughness length changed from 0.7 to 0.4 m. To examine the impact of this sensitivity on the cover types, footprint functions based on values of L=-100, u_*=0.50 m s^{-1}, and z_o[0.4, 0.7,1.0 m], typical for BOREAS noontime, clear-sky conditions, were applied to TE-1 data for N-S grid flight trajectory with west wind in the NSA grid, and E-W grid flight trajectory with south wind in the SSA grid.

Figures 5.3a,b shows the footprint functions for the specified values of z_o and the corresponding weighted, cumulative footprint estimates. To discuss the significance of the estimates, X_{98} and X_{max} are defined as the upwind distances corresponding to a cumulative 98% of the FP, and local maximum contribution, respectively, for the measured flux. For z_o values of 0.4, 0.7 and 1.0 m, X_{98} values were 739, 614 and 534 m, and the Xmax values were 72, 58 and 49 m, respectively. The impact of the changes in the footprint on cover types is demonstrated in Figure 5.4, which represents the ratio of the proportion of the cover types within the footprint to the grid average values. One can see that a change in the footprint from 534 m to 739 m had little effect on the proportion of the cover types contributing to the flux. One other important observation that can be made from Figure 5.4 is that the area effectively sampled by the aircraft was representative of the grid, with the exception of class 6, which is open water. However, since the surface coverage of that class is < 0.3%, this discrepancy is irrelevant for the purpose of this analysis.

Table 5.2 Description of the cover classes based on based on TE-2 classification.

Image Value	TE-2 classification	Description
1-7	Same as in TE-1	same as in TE-1 classification
8	Fire Blackened	same as in class 11 of TE-1 classification
9	New Regeneration Conifer	consists primarily of conifers that are regrowing after a burn, and may also include conifer stands where there are few remaining trees after a low to medium intensity burn
10	Medium-Age Regeneration Conifer	areas that are predominantly young jack pine or young black spruce, and typically occurs in stands that were cleared or burned and have been growing back for approximately 10 years
11	New Regeneration Deciduous	consists of aspen that is starting to regrow after a recent clearing, and may also include grasses or other herbaceous vegetation
12	Medium-Age Regeneration Deciduous	consists of areas that were cleared or burned and have been growing back as aspen, with stands typically containing 10 year old aspen where the background is almost completely obscured and thining has not yet taken place
13	Grass	consists primarily of grasses, agricultural fields that have been planted, or shrub-like vegetation

Table 5.3. Description of cover classes at the grid sites based on RSS classifications.

Image Value	RSS Class	Description
1	Pine	stands of predominantly jack pine, includes regenerating jack pine on a recently disturbed areas
2	Spruce	stands of predominantly black spruce or white spruce, also includes areas of very low biomass treed muskeg
3	Aspen	stands of predominantly immature or mature aspen
4	Shrubland	treeless areas of willow and other deciduous shrubs, includes very young aspen regeneration
5	Clearing	areas of recent logging activity where tree cover is removed
6	Fen	treeless wetlands mostly covered with bog birch or other low shrubs
7	Water	Lakes, ponds and larger rivers

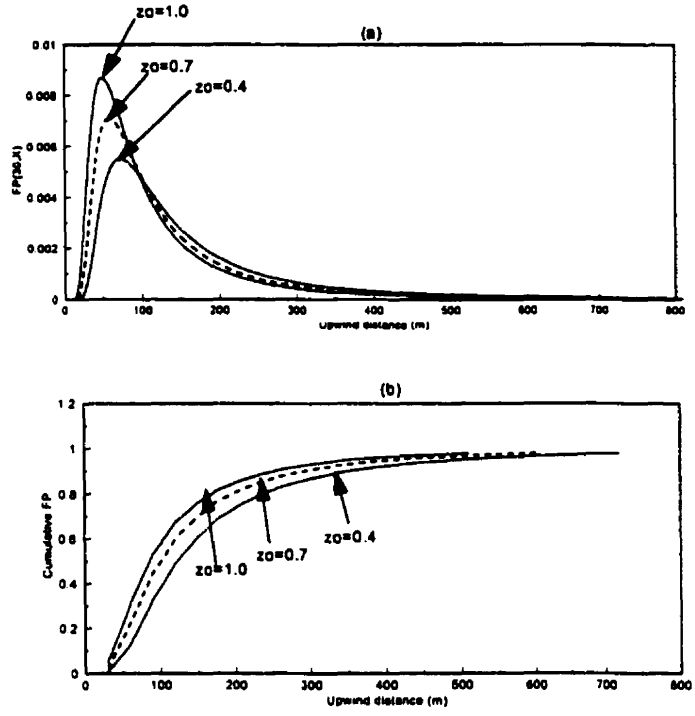

Figure 5.3 Footprint function for specified values of z_o (a) and the corresponding cumulative footprint (b)

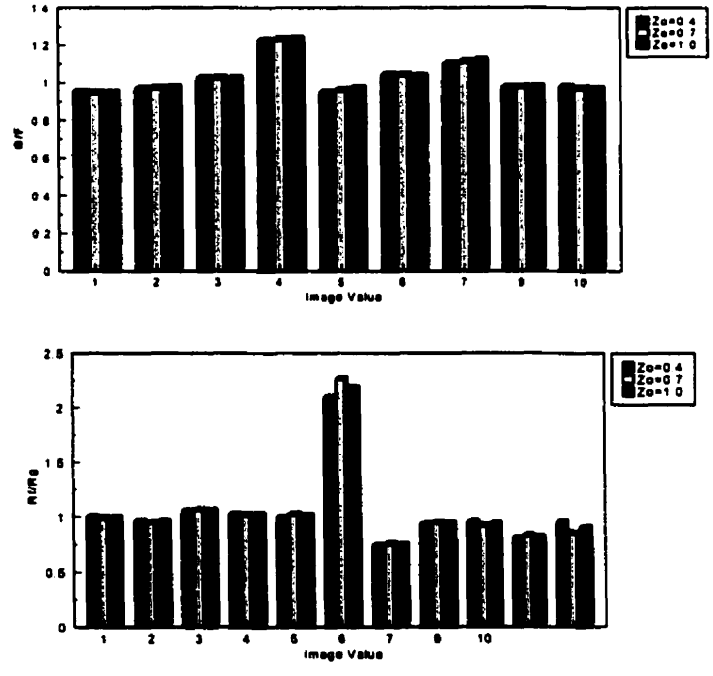

Figure 5.4 : Ratio of the proportion of the cover types within the footprint to the grid average value

5.5.3 Choosing the most appropriate cover map

It is not easy to decide which classification technique best describes the grid landscape, and which should be used for creating data for the regression analysis. While all the maps revealed the basic cover patterns, as discussed above, visual inspection suggests some systematic bias in some of the classes for the various classifications. For example, the fen class in TE-2 appeared over-represented while the conifer (wet) class appeared under-represented. To ensure the best results from the regression model, it is important that the cover map adequately reflects the actual condition at the surface.

To chose the best map, a footprint function based on z_o=0.65 m, d = 8 m, u_*=0.56 m s^{-1} and L=-100, was applied to TE-1, TE-2 and RSS using N-S grid flight trajectories. The estimates of each of the cover types within the FP of the 2 km window along the flight lines were used to produce maps of class abundance. Such maps for the NSA, showing the abundance for regeneration (shrub), conifer wet (spruce) and conifer dry (pine), are shown in Figure 5.5. As seen from this figure, the regeneration class within the flux footprint showed equal strength for all the maps, though with greater spatial extent in RSS and TE2 compared to TE-1. However, the conifer (wet) or spruce class, and the conifer(dry) or pine class, within the flux footprint in TE-2 appeared non-representative of the grid. This is because their percentage composition which occurred around the old black spruce tower and the old jack pine tower are 21 % and 5%, respectively, compared to 87% and 78% for RSS, and 69% and 65% for TE-1. One of the criteria for locating the flux towers was the presence of a (>60%) single vegetation type in an area. For this reason, TE-2 was rejected for the analysis. Either RSS or TE-1 could be used for the analysis, but RSS was chosen over TE-1 based on the more representative year of data acquisition. The species composition maps for the SSA grid (Figure 5.6) are shown for the regeneration, conifer (wet) and fen classes. In this case, all the data sets were found appropriate for the analysis, but TE-2 was chosen because of its more detailed surface description.

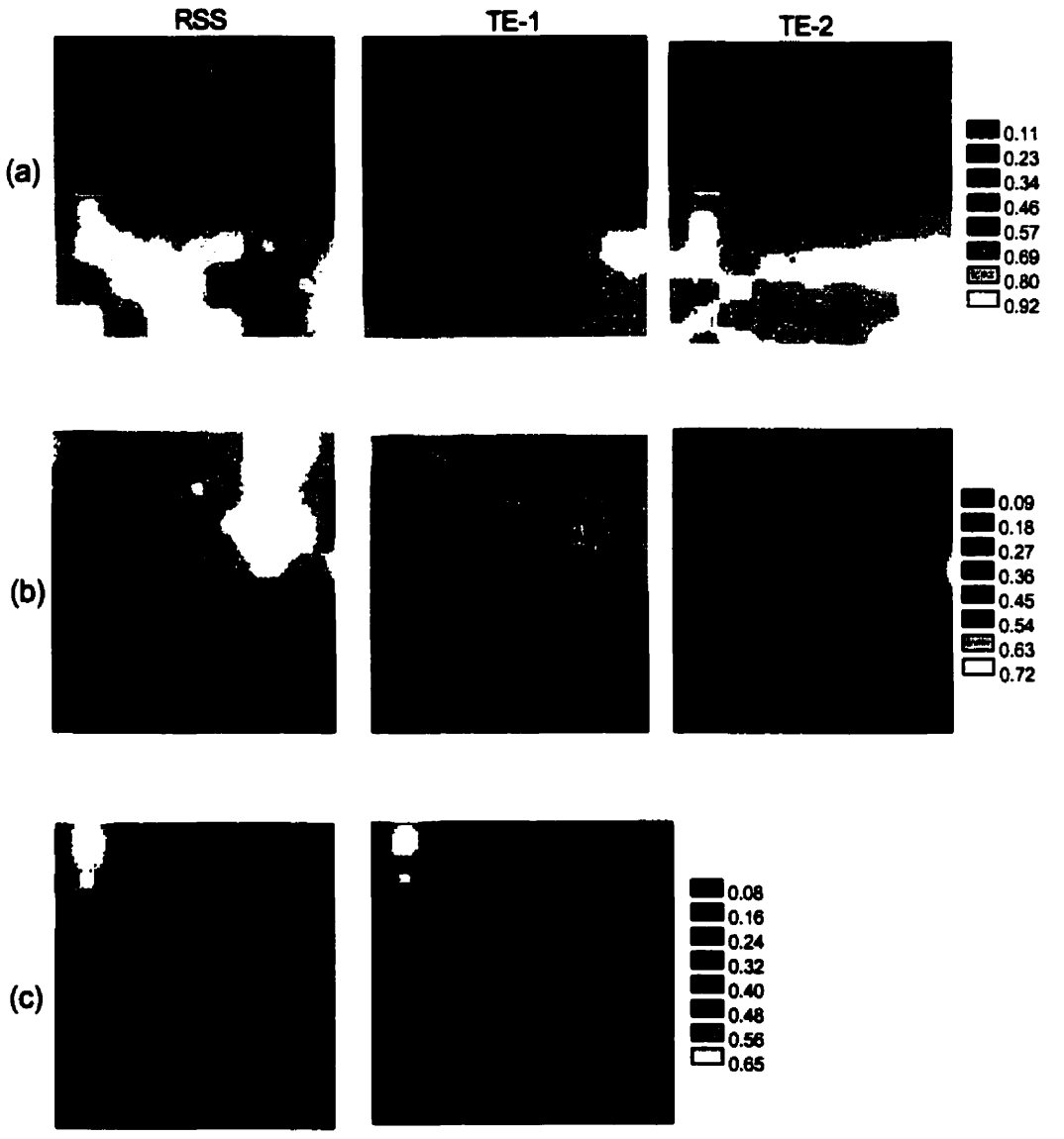

Figure 5.5 : Maps showing abundance of (a) regeneration or shrub, (b) conifer (wet) or spruce and (c) conifer (dry) or pine

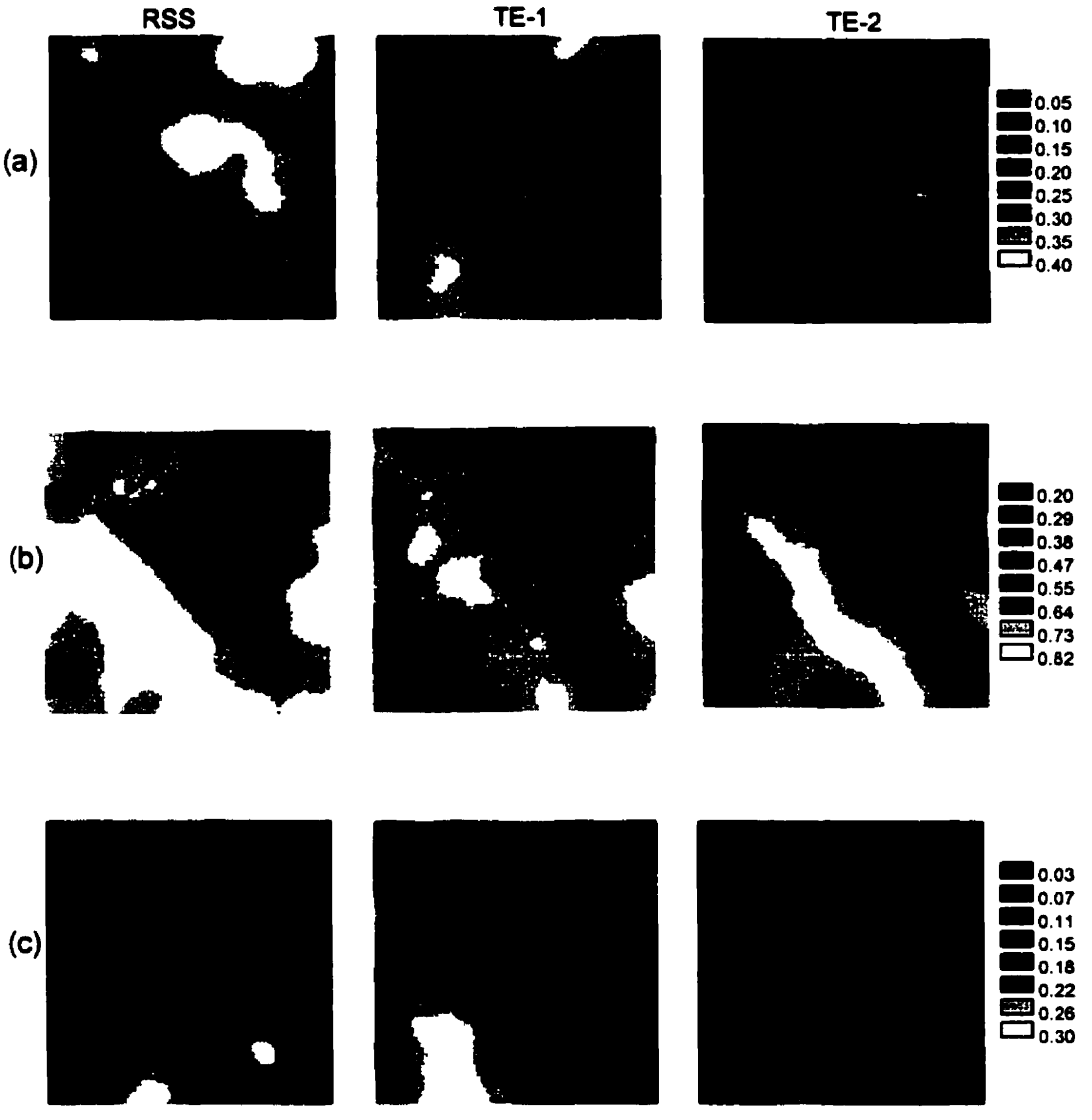

Figure 5.6 : Species composition maps for the SSA grid, showing the (a)regeneration, (b)conifer (wet) or spruce, and (c) fen classes

5.5.4 Regression Analysis: SSA grid

Airborne data from IFC-1, IFC-2 and IFC-3 were used to formulate regression models for sensible heat, latent heat and CO_2 fluxes, for each IFC, at the SSA. Spatially averaged value of z_0 and d, were obtained by spatial aggregation based on the weighted value of the individual cover types, using values of z_0 and d for different cover types at the grids as given in *Kaharabata et al.* [1997] and *Mahrt et al.* [1997]. The weight of the pixels, α_x, were determined for all pixels within 98% of the flux footprint, and were applied on the TE-2 cover map. The choice of X_{98} was made to ensure that the cover types that contributed to the flux were adequately represented.

The values of u_* and L for the grid flights in the three IFCs are given in Table 5.4. Also given in the table are the values for X_{max} and X_{98}. Averaged values of u_* for each of the IFC was typical for mature forest stands. Highest variation in the values of L occurred during IFC-2. On the average, the minimum distance from which contribution was made to the measured flux, X_{min}, was about 20 m, while the local maximum contribution was from cover types located about 70 m from the flight path. About 28 pixels on the cover maps (based on TM spatial resolution of 30 m) contributed 98% of the measured flux.

For the purpose of the regression analysis, in order to prevent undue fragmentation of the impact of the various types of regeneration, classes in TE-2 were reclassified. New regeneration conifer and medium-age regeneration conifer classes were merged, and the new class named conifer regeneration. Also the new regeneration deciduous and medium-age regeneration deciduous classes were merged, and the new class named deciduous regeneration.

The following abbreviations were used for the cover classes : Conifer (wet) (*Cw*), Conifer (dry) (*Cr*), Mixed (*Mi*), Deciduous (*De*), Fen (*Fe*), Disturb (*Di*), Conifer regeneration (*Cr*), Deciduous regeneration (*Dr*). The fire blackened, water and grass classes were not used in the regression analysis because of their small composition in the grid (each less than 0.3%), and the fact that their estimated values in the flux footprint were often not representative of the grid average.

The regression models for CO_2 flux are given in Eq. 5.8. In each of the IFCs, a significant relationship was observed. The coefficients of determination, R^2, were 0.70 for

IFC-1 (C_{ifc1}), 0.89 for IFC-2 (C_{ifc2}), and 0.91 for IFC-3 (C_{ifc3}). Four cover classes in IFC-1, five in IFC-2 and four in IFC-3 made significant contributions to the flux.

Table 5.4 SSA grid flight conditions and footprint estimates

Year	Date	Flight No	Flight Dir	Cross Wind	u_* ($m\ s^{-1}$)	-L (m)	X_{min} (m)	X_{max} (m)	X_{90} (m)
IFC-1	05/31/94	07	N-S	West	0.74	183.0	21	74	846
	06/04/94	09	N-S	West	0.71	176.0	20	73	823
IFC-2	07/20/94	21	E-W	North	0.72	415.6	28	100	1242
	07/21/94	22	N-S	West	0.71	202.7	22	78	884
	07/24/94	26	E-W	North	0.66	141.2	19	66	730
	07/26/94	30	N-S	West	0.41	45.1	10	34	365
IFC-3	09/13/94	49	E-W	South	0.65	187.0	21	75	850
	09/16/94	53	N-S	West	0.72	258.0	24	85	998

$$
\begin{aligned}
C_{ifc1} &= -1.05 + 249.01Di^2 + 18.03Dr^2 + 10.19Fe - 23.04Fe^2 - 3.14Cw^2 \\
C_{ifc2} &= 7.65 + 5.74De - 894.93Di^2 - 27.38Dr - 134.54Fe^2 - 67.97Mi + 176.85Mi^2 \\
&\quad + 17.26Cw - 29.22Cw^2 \\
C_{ifc3} &= -2.38 + 28.57De - 58.24Fe - 115.46Mi + 238.61Mi^2 + 65.15Cw
\end{aligned}
\tag{5.8}
$$

The regression model for the latent heat flux (LE) is given in Eq. 5.9. In IFC-1, no significant relationship was found between the latent heat flux and the cover types. This is not very surprising because the surface hydrology, which often has dominant effects on the amount of water exchanged at this time of the year between the ecosystem and the atmosphere, was not accounted for by the cover map. The R^2 values for LE_{ifc2} and LE_{ifc3} were 0.92 and 0.87, respectively. All the cover types used, except *Cd* made a significant contribution to LE in IFC-2.

$$LE_{ifc2} = 3776.26 - 6701.9840Cr - 13685.108De + 30182.0397Di + 14425.197Dr - 22598.95Fe + 126857.87Fe^2 + 28657.20Mi - 106068.61Mi^2 - 22747.8674Cw + 36355.28Cw^2$$
$$LE_{ifc3} = 1455.7942 - 1291.19De + 47474.16Cd - 11891.75Fe - 5188.33Mi + 13610.03Cw^2 \quad (5.9)$$

The regression model for sensible heat flux (H) is given in Eq. 5.10.

$$H_{ifc2} = -1834.22 + 4988.85De^2 + 10474.21Dr^2 + 9990.60Fe - 27888.5077Fe^2 + 7254.16Cw - 11743.44Cw^2$$
$$H_{ifc3} = 3834.3225 - 7453.248De - 24900.66Mi^2 + 7729.74Mi - 17619.1654Cw + 18411.96Cw^2 \quad (5.10)$$

As in the case of LE, no significant linear relationship was observed between H and the cover types in IFC-1. The R^2 values for H_{ifc2} and H_{ifc3} were 0.84 and 0.93, respectively. The apparent difference in the regression coefficients from one IFC to another is an indication of the complex nature of the forest ecosystem. In all cases, the relative contributions to the fluxes due to each cover type vary between the IFCs. The nonlinear nature of the relationships between the fluxes and the cover types is depicted by the quadratic terms in the models. The variation in the number of cover types between IFCs that made a significant contributions to the fluxes even when almost the same average number of pixels were within the flux footprint, indicates the dependence of the fluxes on biophysical and phenological properties of the cover types.

5.5.5 Evaluation of model estimates: SSA

To evaluate the model, an independent dataset from the 'Candle Lake run' [*MacPherson, 1996*] was used. The flight trajectory of the run is given in Figure 5.7. The run was approximately 115 km in length, and was flown at an altitude of about 40 m. The data used for model evaluation are from flights executed either overlapping or within up to 8 days from the timing of the grid flights used in the regression model. The track was chosen to

cover significant heterogeneity; it crossed aspen and black spruce forests, a partially logged area, an old burn and three lakes (Halkett, Candle and White Gull). The track was divided into nine segments (Table 5.5), over which the mean fluxes were calculated. Also, the values for z_o, d, u_* and L were calculated for each segment. The description of the segments from west to east is given in Table 5.5.

Table 5.5 Description of the segments along the candle Lake Run

Segment	Approximate Length, km	Description
A	19	aspen
B	2	Halkett L.
C	14	mostly aspen
D	17	mostly burn
E	17	mixed logged
F	11	Candle Lake
G	12	spruce
H	4	White Gull Lake
I	18	spruce

The fraction of cover types within the aircraft FP, calculated for the segments, are given in Table 5.6. To include the seasonal trend in the fluxes, one run from each of the three IFCs was used. The predicted fluxes for each segment, based on the regressions in Equations 5.8, 5.9 and 5.10, are compared in Figures 5.8, 5.9, and 5.10 against the observed fluxes from the Twin Otter aircraft.

Results are generally very encouraging, since they represent (to the author's knowledge) the first successful demonstration of the potential to scale up from local (grid) observations to larger areas. The correlation coefficients for C are 0.79, 0.89 and 0.90 for IFC-1, IFC-2 and IFC-3, respectively. In IFC-2 and IFC-3, the coefficients are 0.92 and 0.90 for LE, 0.88 and 0.93 for H, respectively. Both LE and C displayed a similar trend that is related to the growth cycle of vegetated plants. The results highlight the significance of aspen in the CO_2 uptake and moisture exchange in the boreal forest. In spring (May 25), when few

leaves were on the aspen trees, C estimates were lower over the aspen than over the spruce. In the summer (July 25), when leaves are fully developed, C and LE estimates over the aspen were higher than over the spruce, and in the Fall (Sept. 12), C estimates over the aspen were comparable to those over spruce. Estimated H values gave highest values over the spruce (on July 25 and Sep. 12).

Table 5.6 Fraction of cover types in the flux footprint along the Candle Lake run

	Fraction of cover types								
	Date	*Cw*	*Cd*	*Mi*	*De*	*Fe*	*Di*	*Cr*	*Dr*
C (Aspen)	05/25/94	.02	0.01	0.15	0.51	0.03	0.02	0.04	0.18
	07/25/94	0.03	0.01	0.18	0.49	0.02	0.01	0.04	0.18
	09/12/94	0.04	0.01	0.19	0.49	0.02	0.01	0.04	0.17
D (Mixed)	05/25/94	0.20	0.01	0.28	0.12	0.05	0.01	0.10	0.19
	07/25/94	0 .24	0.00	0.26	0.12	0.05	0.00	0.09	0.19
	09/12/94	0.24	0.00	0.26	0.12	0.05	0.03	0.09	0.18
E (Mixed)	05/25/94	0.25	0.00	0.21	0.17	0.07	0.03	0.13	0.11
	07/25/94	0 .23	0.00	0.19	0.18	0.07	0.02	0.16	0.14
	09/12/94	0.22	0.00	0.18	0.17	0.07	0.01	0.16	0.14
G (Spruce)	05/25/94	0.33	0.00	0.10	0.05	0.22	0.00	0.27	0.00
	07/25/94	0.34	0.00	0.12	0.05	0.19	0.00	0.25	0.01
	09/12/94	0 .35	0.00	0.13	0.05	0.19	0.00	0.24	0.01
I (Spruce)	05/25/94	0. 30	0.00	0.06	0.06	0.22	0.00	0.32	0.02
	07/25/94	0.30	0.01	0.06	0.06	0.22	0.00	0.32	0.03
	09/12/94	0.30	0.01	0.07	0.06	0.21	0.00	0.31	0.03

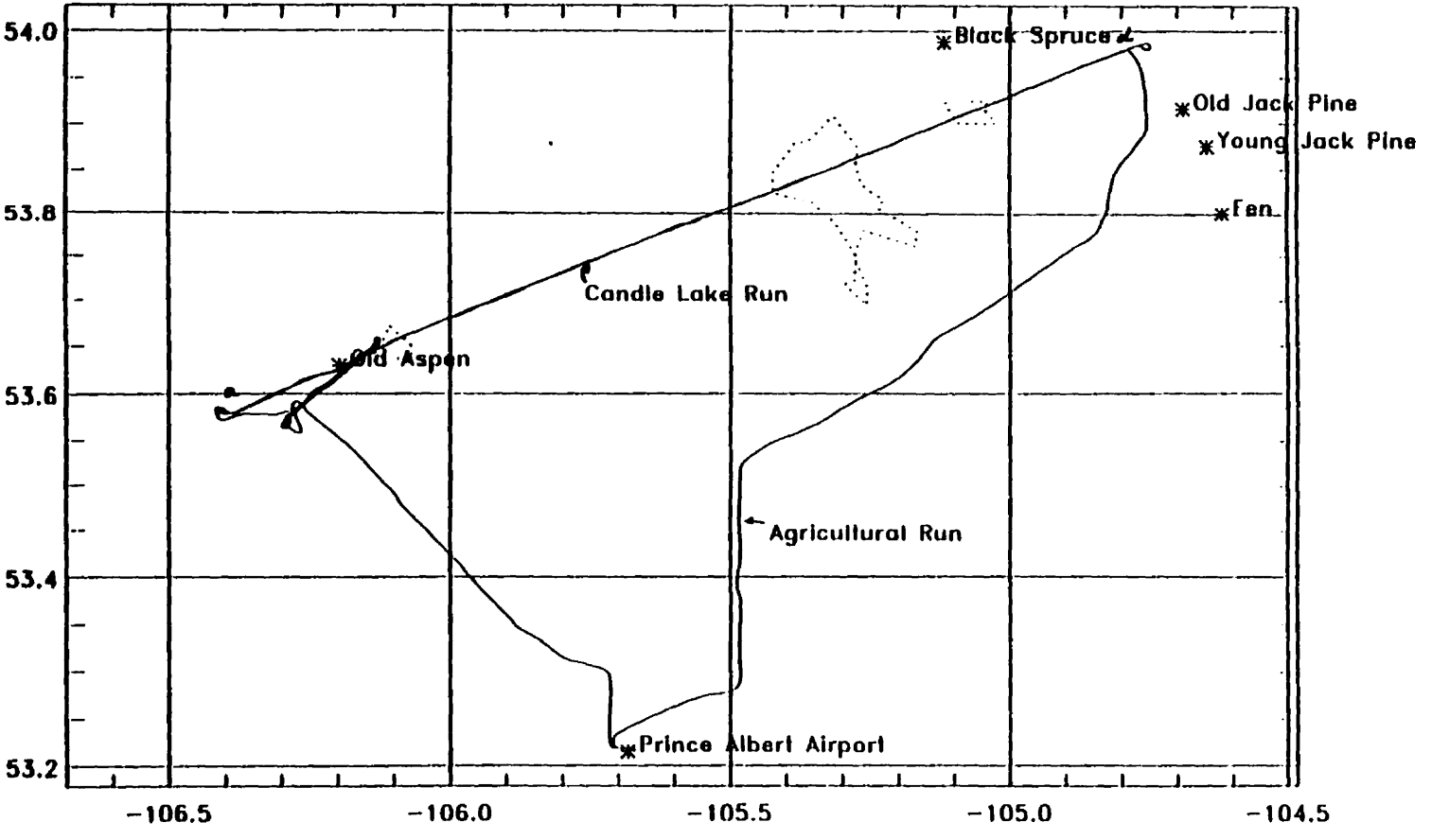

Figure 5.7 : The flight trajectory for the Candle lake run

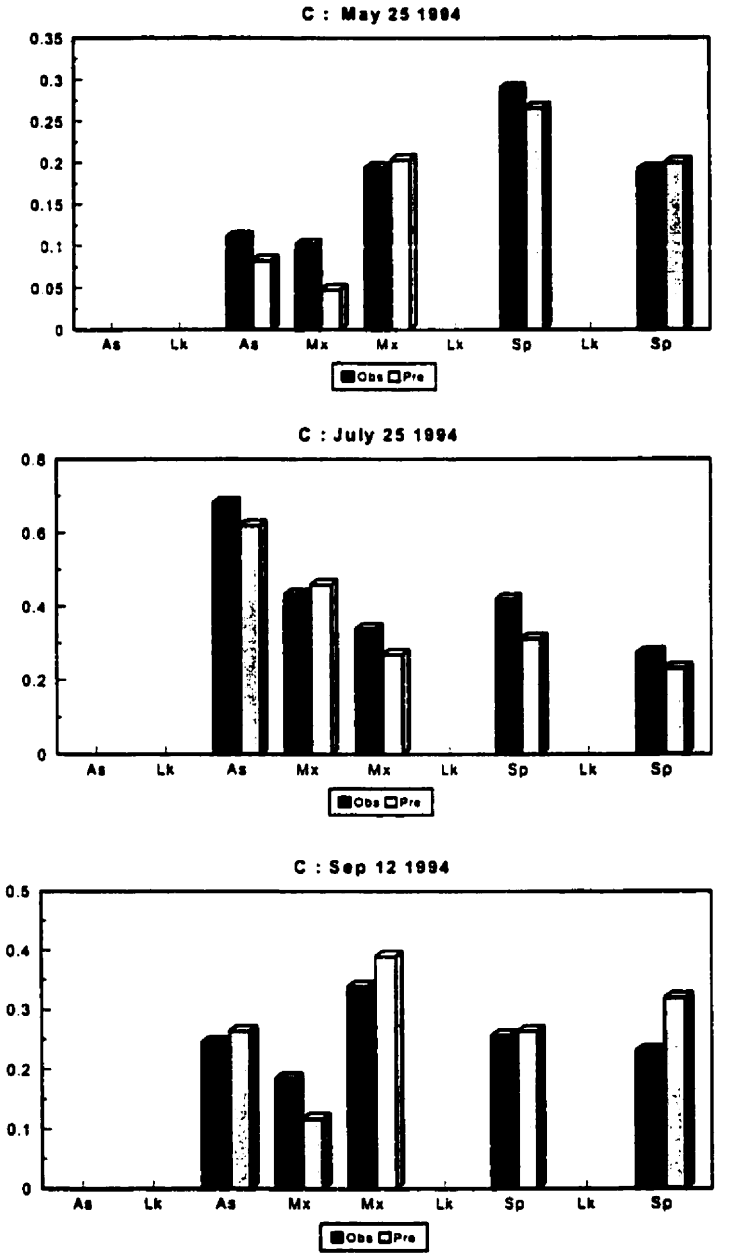

Figure 5.8 : Comparison of the airborne observed CO_2 fluxes along the Candle lake run against the regression model estimates

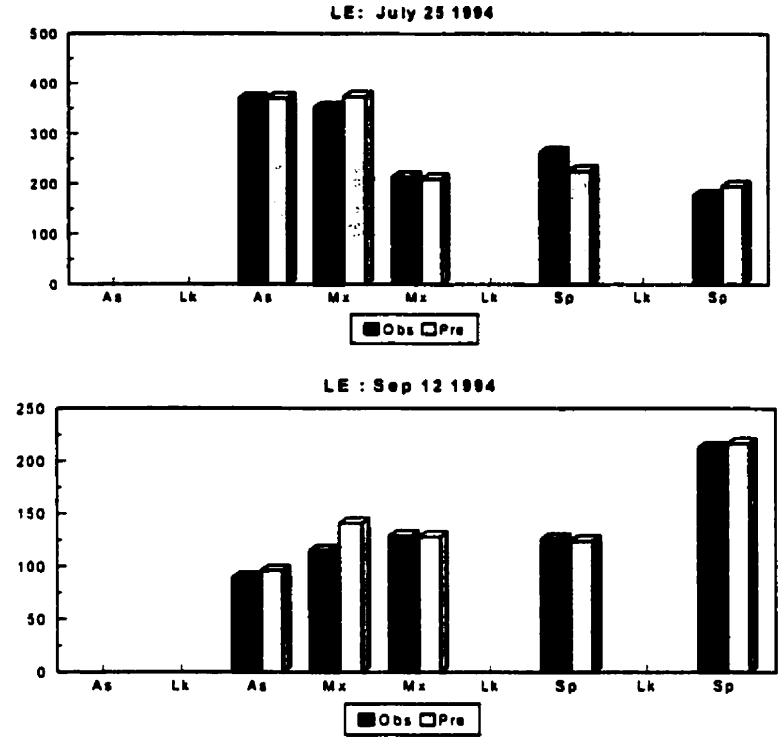

Figure 5.9 : Comparison of the airborne observed latent heat fluxes along the Candle Lake run against the model predictions.

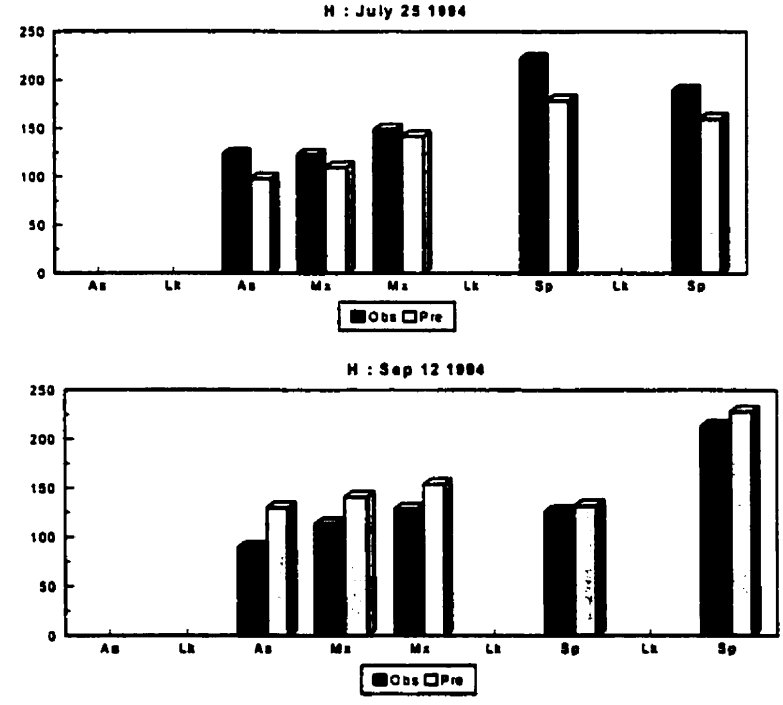

Figure 5.10 : Comparison of the airborne observed sensible heat fluxes along the Candle Lake run against the model predictions.

5.5.6. Regression Analysis: NSA grid

The purpose of the regression analysis for this site was to explore its potential in a situation where a single cover type (viz. old black spruce or regenerating burn) dominated each half of the grid area. Two sets of regression equations were developed from grid data, one set for the closed canopy (predominantly black spruce) forested area in the northern half of the grid, and the other set for the sparse and open canopy regenerating area in the southern half of the grid. The flux data used were from IFC-2. The conditions for the grid flights and the associated footprint parameters are shown in Table 5.7. The regression equations for the northern and southern halves (differentiated by subscripts n and s) are given by Eqs. 5.11 and 5.12. Abbreviated class name used are Aspen (*As*), Fen (*fe*), Spruce (*Sp*), Pine (*Pi*), Clearing (*Cl*), Shrub(*Sh*), and Water (*Wt*).

The main difference between the two sets of equations is obvious from the contributions due to *Sp* and *Fe*. At the northern half of the site there was no significant contribution due to *Fe*, and each of the flux type has a non linear relationship with *Sp*. However, at the southern half of the grid *Fe* contributions to all the fluxes were significant, and its relationship with the fluxes of moisture and CO_2 is quadratic.

Table 5.7 Northern study area grid flight conditions and the associated footprint parameters.

Year	Flight No	Flight Dir	Cross Wind	u_* ($m\ s^{-1}$)	-L (m)	X_{min} (m)	X_{max} (m)	X_{end} (m)
1994	33	N-S	West	0.49	67.6	13	45	475
	35	N-S	West	0.31	25.2	6	30	247
	37	N-S	West	0.72	245.2	23	84	975
	39	N-S	West	0.51	65.8	12	44	467

$$
\begin{aligned}
C_s &= 0.469 - 13.482Fe^2 - 2.21Pi - 1.03Sh + 2.19Sp \\
H_s &= -746.74 + 2447.97Fe + 1012.90Sh - 1568.65Sp \\
LE_s &= -309.29 + 7674.28Fe^2 - 16744.86Pi^2 + 666.094Sh \\
&\quad -5763.30SP^2
\end{aligned}
\tag{5.12}
$$

$$C_n = 7.49 - 4.49Pi - 9.917Sh - 14.08Sp + 6.67Sp^2$$
$$H_n = 1195.58 - 16738.79As - 6846.78Pi + 10575.02Sp - 12832.68Sp^2 \quad (5.11)$$
$$LE_n = -2088.27 - 3926.18As + 3337.20Sh + 6636.83Sp - 4760.34Sp^2$$

5.5.7 Evaluation of model estimates: NSA

To validate C_n, H_n and LE_n, data from the site-specific old black spruce run [*MacPherson*, 1996] were used. The run was divided into four segments (A, B, C and D), whose coordinates are given in Table 5.8, and fluxes were averaged over each of the segments. Three flights flown on 29 July, 2 August and 8 August were used to test the regression models. Each of the flights consisted of at least six passes. The fraction of cover types within the flux footprint of the segments are given in Table 5.9 and Figure 5.11 shows the plots of the observed fluxes against the flux estimates based on these cover fractions. For all the fluxes, a good agreement was observed between the predicted and observed estimates. The correlation coefficients, *R*, for C, H, LE were 0.8, 0.82 and 0.91, respectively.

Table 5.8 Coordinates of the segments along the old black spruce run

	A		B		C		D	
	Lat.	Long.	Lat.	Long.	Lat.	Long.	Lat.	Long.
Start	55.8826	-98.5232	55.8803	-98.4917	55.8809	-98.4600	55.8783	-98.4276
End	55.8803	-98.4914	55.8801	-98.4600	55.8783	-98.4286	55.8752	-98.3972

To validate C_s, H_s and LE_s, data from the site-specific burn run (MacPherson, 1996) were used. The data, from two flights flown on 29 July, and 02 August, consisted of five and six passes, respectively. The flight length was divided into five segments (A, B, C, D and E), whose coordinates are given in Table 5.10, and fluxes were averaged over the segments. Table 5.11 shows the cover fractions of the cover types within the footprint of the segments. The plots of the observed flux estimates against predictions from Eq. (5.12) are shown in Figure 5.12 As observed for the northern half of the grid, the regression models for the southern half gave very encouraging results. The model outputs compared very well with the observed fluxes, with *R* values for C, H, and LE of 0.94, 0.84, and 0.93, respectively.

Table 5.9. Fraction of cover types within the footprint of the old black spruce run segments.

	Fraction of cover types					
	Date	*Pi*	*Sp*	*As*	*Sh*	*Cl*
A	07/29/94	0.25	0.43	0.09	0.19	0.01
	08/02/94	0.25	0.48	0.09	0.16	0.0
	08/08/94	0.25	0.43	0.09	0.19	0.01
B	07/29/94	0.21	0.76	0.01	-	-
	08/02/94	0.19	0.77	0.02	-	-
	08/08/94	0.21	0.76	0.01	-	-
C	07/29/94	0.16	0.74	0.04	0.03	-
	08/02/94	0.19	0.77	0.02	-	-
	08/08/94	0.16	0.74	0.04	0.03	-
D	07/29/94	0.28	0.60	0.05	-	-
	08/02/94	0.25	0.63	0.04	-	-
	08/08/94	0.28	0.60	0.05	-	-

Table 5.10 Coordinates of the segments along the burn site run

	A		D		C	
	Lat.	Lon.	Lat.	Lon	Lat.	Lon
Start	55.8546	-98.4749	55.8527	-98.4590	55.8486	-98.4431
End	55.8527	-98.4585	55.8486	-98.4426	55.8468	-98.4236

	D		E	
	Lat	Lon	Lat	Lon
Start	55.8468	-98.4272	55.8443	-98.4113
End	55.8443	-98.4108	55.8435	-98.3949

Table 5.11 Fraction of cover types within the footprint of the segments along the burn run.

	Fraction of cover types							
	Date	*Pi*	*Sp*	*As*	*Sh*	*Cl*	*Fe*	*Wt*
A	07/29/94	0.02	0.01	0.01	0.93	-	-	-
	08/02/94	0.05	0.04	0.01	0.86	-	0.1	-
	05/25/94	0.03	0.03	0.01	0.90	-	-	-
B	07/25/94	0.04	0.05	-	0.87	-	-	-
	05/25/94	0.01	0.06	-	0.74	0.03	0.06	0.07
C	07/25/94	0.01	0.03	-	0.72	0.03	0.05	0.13
	05/25/94	-	0.07	-	0.55	-	0.18	0.18
D	07/25/94	0.01	0.10	-	0.53	-	0.18	0.16
	05/25/94	-	0.15	0.01	0.64	0.01	0.18	-
E	07/25/94	-	0.15	0.10	0.63	-	0.18	-

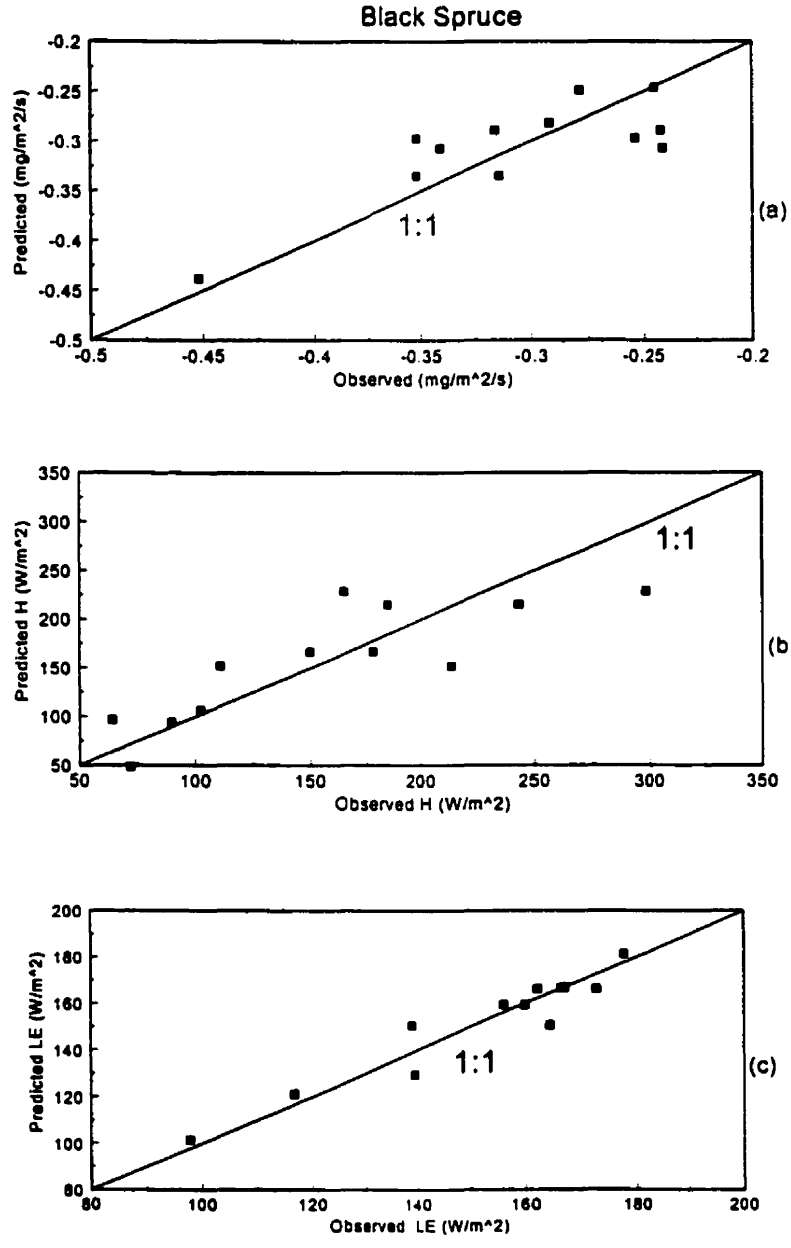

Figure 5.11: Plots of the observed against the regression estimates of (a) C, (b) H and (c) LE, for the black spruce run

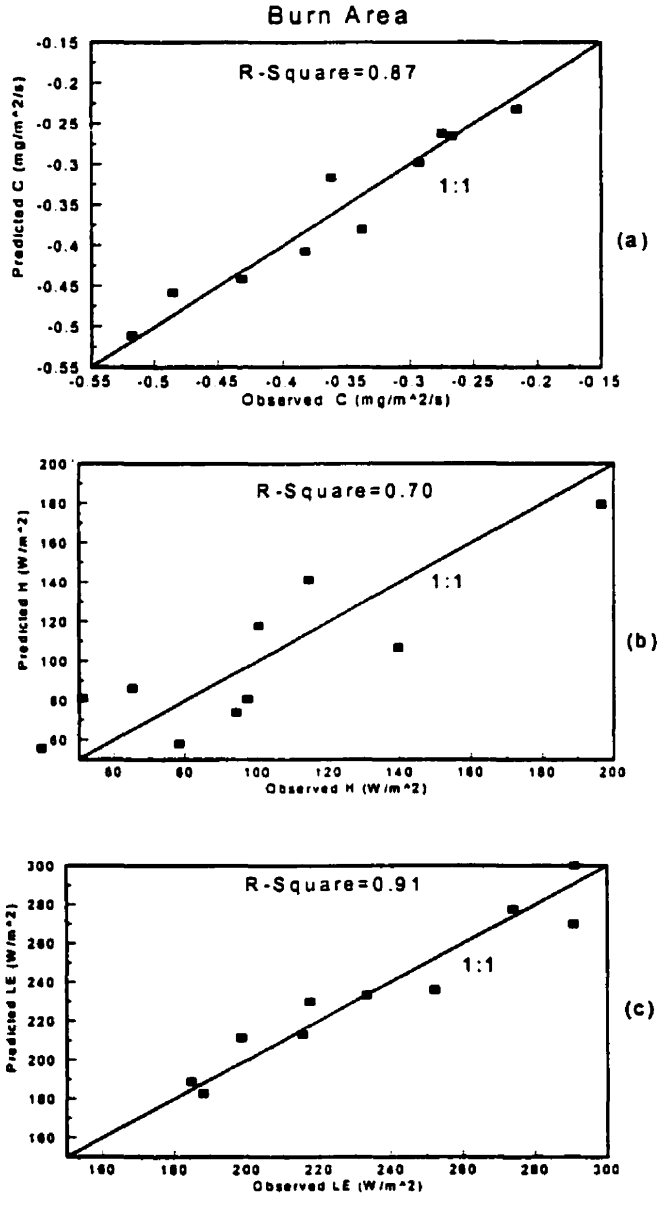

Figure 5.12 : Plots of the observed against the regression estimates of (a) C, (b) H, and (c) LE, for the burn run

5. 6 CONCLUSIONS

The analysis in this section focused on the description of the grid sites by satellite and videographic based observations of cover types, and establishing relationship between the cover types and the airborne measured fluxes. There were some agreements between the satellite and videographic land cover maps of the given BOREAS grid sites, which were characterised by a mosaic of broad-leaved deciduous (aspen, *Populus*, birch, *Betula*), evergreen conifer(black spruce, *Picea mariana*; jack pine, *Pinus banksiana*; and larch, *Larix)*forests, fens and scattered ponds. Site descriptions showed a well developed closed canopy forest in the northern half and predominantly regenerating plants in the southern half of the NSA grid site. The SSA grid was dominated by black spruce with highest concentration below the NW-SE diagonal, decreasing towards the SW quadrant where fen occurred in abundance.

Previous studies (Chapters 3 and 4) demonstrated links between the flux distribution patterns at the grid sites and the surface configuration of the land cover. These findings were further investigated in this study with the objective of establishing quantitative relationships between cover types and airborne measured fluxes, based on multiple linear regression. The results showed that at the SSA in 1994 IFC-2, the cover types within the flux footprint accounted for 89%, 84% and 95% of the variations in the measured airborne fluxes of CO_2, sensible heat and latent heat, respectively. In the same order, R^2 values were 0.94, 0.96 and 0.87 in IFC-3. Similar results were obtained for the NSA grid. The results from the validation of the regression models, where flux estimates over regional transects outside the grid area (SSA) or site-specific runs within the grid area (NSA), based on fractional distributions of surface cover types, were compared against observed fluxes, were very encouraging. They showed the potential for extrapolating models that were developed for a given location to another location, based simply on the fractions of cover types, at least for similar land cover types. Such extrapolation would - of course - be limited by the dependence of the regression equations on phenological status and physical condition (e.g. surface wetness) of the land cover. However, considering that until now no consistent results have been reported from the use of boundary layer models in predicting fluxes over heterogeneous

areas, and how little effort has been made by modelers to relate fluxes to cover types in these areas, the results from this study will hopefully stimulate further research on this problem.

GENERAL CONCLUSIONS

The boreal forest represents one of the world's largest yet poorly understood ecosystems. The BOREAS project, a field-based experiment, provided data that should help to improve our understanding of the exchange of radiative energy, sensible heat, water vapour, CO_2 and trace gases between the boreal forest and the lower atmosphere. The uniqueness of the project lies in the incorporation of a multi-disciplinary approach ranging from terrestrial ecology to remote sensing and multiscale measurement strategies spanning leaf- to regional scale.

This thesis focused on the analysis of two-dimensional patterns of surface atmospheric boundary layer coupling for multiple grid flights in two study areas of BOREAS. Strong correlations were observed between CO_2 flux and greenness index, a very encouraging results for modelers trying to estimate large-scale surface fluxes of carbon over the boreal zone based on remote sensing observations. At the same time, sensible heat fluxes were noticeably decoupled from the atmosphere-surface temperature difference, particularly over black spruce, signaling the problems that modelers will have to face in attempts to estimate the energy balance from boundary layer models. The successful efforts in BOREAS in delineating the surface source zones sampled by airborne flux systems provided a basis for correlating the airborne fluxes, which are highly dependent on the nature of the forest landscape, with surface cover types. The results from this study suggest not only that knowledge of the proportion of cover types in a heterogeneous areas is necessary for the prediction of the strength of scalar fluxes, but also gives some indirect insight into spatial scales that are of importance for such estimates.

The BOREAS project, and in particular this study, demonstrated the paramount difficulty of airborne observations in boundary layer modeling of mass and energy. It is generally believed that the most effective way of estimating surface energy fluxes over very large areas is through the use of satellite data, particularly in heterogeneous areas and/or areas of limited accessibility for direct flux observation in the field. However, since surface fluxes arise from low level gradients of temperature and humidity that cannot be measured from space-based remote sensing instrument, estimation of fluxes from satellite data rely on

boundary layer models, which in many cases can only be validated by airborne measured data.

The growing concern about global warming and its impact on the environment requires that more large scale experiments such as BOREAS be conducted to provide data that will help to understand the exchange processes over ecosystems that are perceived to affect global circulations, but whose real influences are not yet understood. The Canadian component of the ongoing GEWEX (global energy and water exchange experiment) program, for example, consists of a series of large-scale hydrological and related atmospheric and land-atmosphere studies being conducted over the Mackenzie Basin. It is believed that this experiment will provide an improved understanding of high latitude hydrological and meteorological processes, and their role in the global climate system. It will provide a large-scale opportunity to test coupled hydrological and atmospheric models. However, since a large part of the areas are inaccessible to ground-based measurements, airborne observations are required. Under this condition, the usefulness of the acquired data, and their extrapolation to larger areas for intercomparison against models, would depend on the ability to relate the observed surface fluxes to the cover types of the area. The results from this thesis should prove useful in that regard.

REFERENCES

Abareshi, B., and P.H., Schuepp, (1998) : Sensible heat flux estimation over the FIFE site by Neural Networks. *J. Atmos. Sc.* **55**,1185-1197

American Geophysical Union (AGU), (1992) : First International Satellite Land Surface Climatology Project (ISLSCP) Field Experiment (FIFE), *J. Geophys. Res.*, **97**(D17), 18,343-19,109

Amiro, B.D., (1998) : Footprint climatologies for evapotranspiration in a boreal catchment, *Agric. For. Meteorol.* **90**, 3,195-201

André, J. C, J.P. Goutorbe, and A. Perrier, (1986) : HAPEX-MOBILHY - A hydrological atmospheric pilot experiment for the study of water budget and evaporation flux at the climatic scale, *Bull. Am. Meteorol. Soc.*, **67**, 138-144

Antonia R. A., (1981) : Conditional sampling in turbulence measurement. *Ann. Rev. Fluid Mech.* **13**, 463-469

Avissar, R., and R. A. Pielke, (1991): The impart of plant stomatal control on mesoscale atmospheric circulation. *Agric. For. Meteorol.*, **54**, 353-372

Baldocchi, D. and C. A. Vogel (1997). Seasonal variation of energy and water vapour exchange rates above and below a boreal jack pine forest canopy. *J. Geophys. Res.* **102**(D24), 28,939-28,951

Baldocchi, D. D., C. A. Vogel., and B. Hill, (1997) : Seasonal variation of carbon dioxide exchange rates above and below a boreal jack pine forest. *Agric. For. Meteorol.*, **83**, 147-170

Baldocchi, D., (1997) : Flux Footprints within and above forest canopy. *Boundary Layer Meteorol.* **85**: 273-292.

Barr, A.G., and A. K. Betts, (1994) : Preliminary summary of BOREAS upper-air soundings. Technical report, Atmospheric Environment Service, Saskatoon

Barr, A.G., and A. K. Betts, (1997) : Radiosonde boundary layer budgets above a boreal forest. *J. Geophys. Res.* **102**(D24), 29,205-29,213

Betts, A. K., and J. H. Ball, (1994) : Budget analysis of FIFE sondes. *J. Geophys. Res.* **99**: 3,655- 3,666

Brutsaert, W., (1992) : *Evaporation Into The Atmosphere.* Kluwer Academic Publishers, Dordrecht, The Netherlands.

Bonan, G. B., and H. H. Shugart (1989) : Environmental factors and ecological processes in boreal forest, *Ann. Rev. Ecol. Syst.*, **20**, 1-28

Caramori P., P.H Schuepp, R. L. Desjardins, and J. I MacPherson (1994) : Structural analysis of airborne fluxes estimates over a region. *J. Climate*, **7**, 627-640

Carlson, T. N., Gillies, R. R. and Perry, E. M. (1995) : A Method To Make Use of Thermal Infrared Temperature and NDVI Measurements To Infer Surface Soil Water Content and Fractional Vegetation Cover, *Remote Sens. Rev.*, **9**, 161-173

Desjardins, R. L., I. J. MacPherson, P. H. Schuepp, and F. Karanja, (1989) : An evaluation of airborne eddy flux measurements of CO_2, water vapour, and sensible heat, *Boundary-Layer Meteorol.*, **47**, 55-69

Desjardins, R. L., P. H. Schuepp, J. I. MacPherson, and J. Buckley, (1992) : Spatial and

temporal variations of the fluxes of carbon dioxide and sensible heat over the FIFE site, *J. Geophys. Res.* **97**(D17), 18,467-18,475

Desjardins, R. L., P. H. Schuepp, J. I. MacPherson and D. J. Buckley, (1992) : Aircraft- and Tower-based fluxes of carbon dioxide, latent, and sensible heat. *J. Geophys. Res.* **97**(D17), 18,477-18,485

Desjardins R.J., J. I. MacPherson, L. Mahrt, P. H. Schuepp, E. Pattey, H. Neumann, D. Baldocchi, S. Wofsy, D. Fitzjarral, H. MacCaughey, and D. W. Joiner, (1997) : Scaling up flux measurements of the boreal forest using aircraft-tower combinations. *J. Geophys. Res.* **102**(D24)29,125-29,135

Diak, G. R., (1990) : Evaluation of heat flux, moisture flux and aerodynamic roughness at the land surface from knowledge of the PBL height and satellite derived skin temperature. *Agric. For. Meteor.* **52**, 181-198

Duncan, M. R. and P. H. Schuepp, (1992) : A method to delineate extreme structures within airborne flux traces over the FIFE site. *J. Geophys. Res.* **97** (D17), 18,487-18,475.

Dobosy, R. J., T. L. Crawford, J. I. MacPherson, R. L. Desjardins, Kelly, S. Oncley, and D. H. Lenshow, (1997) : Intercomparison among four flux aircraft at BOREAS in 1994, *J. Geophys. Res.* **102**(D24)29,101-29,101

Doran, J. C., W.J. Shaw, J. M. Hube, (1995) : Boundary layer characteristics over areas of inhomogeneous surface fluxes, *J. Appl. Meteorol.*, **42**, 559-571

Gao , W., R. H . Shaw, and K.T. Paw U, (1989) : Observation of organised structure in turbulent flow within and above a forest canopy, *Boundary-Layer Meteorol* **47**, 349-377

Garratt, J. R., (1992) : *The Atmospheric Boundary Layer*. Cambridge University Press, Cambridge.

Glooschenko, W.A., N.T. Roulet, L.A. Barrie, H.I. Schiff, and H.G. McAdie, (1994) : The Northern Wetlands Study (NOWES): An overview, *J. Geophys. Res.*, **99**(D17), 1423-1428

Goward, S. N., and Huemmrich, K. F., (1992) : Vegetation canopy PAR absoptance and the normalized difference vegetation index: An assessment using the SAIL model. Remote Sens. Environ., **39**, 119-140

Grant R. H., G. E. Bertolin, and L. P. Herrington, (1996) : The intermittent vertical flux over a spruce forest canopy. *Boundary-Layer Meteorol,*. **35**, 317-330

Grossman R. L.(1992) : Sampling errors in the vertical fluxes of potential temperature and moisture measured by Aircraft during FIFE. *J. Geophys. Res.* **97**(D17), 18,439-18,443

Hall F. G., Huemmrich, K. F. Goetz, S. J. Sellers, P. J. and Nickeson J. E. (1992) : Satellite remote sensing of surface energy balance: success, failures, and unresolved issues in FIFE. *J.Geophys. Res.*, **97**(D17), 19,061-19,089

Hall, F. G., D. Knapp and K. F. Huemmrich, (1997) : A physically based algorithm for integrated classification and biophysical parameter estimations, *J. Geophys. Res.*, **102** (D24), 29,567-29,580

Hall, F. G., Y. E. Shimabukuro, and K. F. Huemmrich, (1995) : Remote sensing of forrest biophysical structure using mixture decomposition and geometric reflectance models, *Ecol. Appl.*, **5** (4), 993-1013.

Hogg, E. H., and P. A. Hurdle (1995) : The aspen parkland in Western Canada: A dry climate analogue for the future boreal forest, *Water Soil Pollut.*, **82**, 391-400

Hollinger, D.Y., F. M. Kelliher, J. N. Byers, J. E. Hunt, T. M. McSeveny, and P. L. Weir, (1994) : Carbon dioxide exchange between an undisturbed old-growth temperate forest and the atmosphere. *Ecology*, **75**, 134-150

Horst, T. W. and J.C., Weil, (1992) : Footprint estimations for scalar flux measurements in the atmospheric surface layer. *Boundary Layer Meteorol.* **59**, 279-296

Horst, T. W. and J.C., Weil, (1994) : How far is far enough? The fetch requirements for micrometeorological measurement of surface fluxes. *J. Atmos. Ocean. Tech.*, **11**, 1018-1025

Houghton, J.T., L.G. Meira Filho, J. Bruce, H. Lee, B.A. Callander, E.Haites, N.Harris, A. Kattenberg, and K. Maskell (eds.) (1996) : *Climate Change 1995 : The science of climate change*, Cambridge University press, Cambridge.

International Panel on Climate Change (1990) : *Climate Change: The IPCC Scientific Assessment*, edited by J.T. Houghton, G. J. Jenkins and J.J. Ephraums, 365 pp., Cambridge Univ. Press, New York

International Panel on Climate Change (1995) : *Climate Change 1994: Radiative Forcing of climate Change and Evaluation of the IPCC IS92 EmissionScenario*, Edited by J. T. Houghton et al., 339 pp., Cambridge Univ. Press, New York

Issaks, E. H., and R. M. Srivastava , (1989) : Applied geostatistics. Oxford University Press, Oxford

Jackson, D., K. Somers, H. Harvey, (1989) : Similarity coefficient : Measure of co-

occurrence and association or simply measure of occurrence, *Amer. Naturalist*, **133**, 436-453

Kaharabata S. K., P. H. Schuepp, S. O. Ogunjemiyo, S. Shen, M. Y. Leclerc, R. L. Desjardins, J. I. MacPherson, (1997) : Footprint considerations in BOREAS, *J. Geophys. Res.* **102**(D24), 29,113-29,125

Kaimal, J.C and J.C., Finnigan, (1992) : *Atmospheric Boundary Layer Flows - Their Structure and Measurement*. Oxford University Press, Oxford.

Kelliher, F.M., R. Leuning, and E.D. Schulze, (1993) : Evaporation and canopy characteristics of coniferous forests and grasslands, *Oecologia*, **95**, 153-163.

Kelly, R. D., E. A. Smith, and J. I. MacPherson, (1992) : A comparison of surface sensible and latent heat fluxes from aircraft and surface measurements in FIFE 1987, *J. Geophys. Res.* **97**(D17), 18445-18453.

Kustas, W. P., B. J. Choudhury, M. S. Moran., R. J. Reginato, R. D. Jackson, L. W. Gay, and H. L. Weaver, (1989) : Determination of sensible heat flux over sparse canopy using thermal infrared data, *Agric. For. Meteorol.*, 44, 197-216.

Lawrence, B., J. Flanagan, R. Brooks, J. R., Ehleringer, (1997) : Photosynthesis and carbon isotope discrimination in boreal forest ecosystem: A comparison of functional characteristics in plants from three mature forest types. *J. Geophys. Res.*, **102**(D24), 28,861-28,869.

Leclerc, M.Y. and G.W. Thurtell, (1990). Footprint prediction from scalar fluxes using a Markovian analysis, *Boundary-Layer Meteorol.*, **52**, 247-258

Lee, X and T. A. Black, (1993) : Atmospheric turbulence within and above a douglas-fir

stand, Part II: Eddy fluxes of sensible heat and water vapour. *Boundary-Layer Meteorol.*, **64**, 369-389

Lenschow, D. H, and P. L. Stephens, (1980) : The role of thermals in the convective boundary layer. Boundary-Layer Meteorol., **35**, 317-330

Lenshow, D. H. and B. B. Stankov, (1986) : Length scales in the convective atmospheric boundary layer, *J. Atmos. Sci.*, 43.1198-1209, 1986

Lenschow, D.H., (1995) : Micrometeorological techniques for measuring biosphere-atmosphere trace gas exchange. *Biogenetic Trace Gases: Measuring Emissions from Soil and water*, 126-163, P.A. Matsom and R.C. Harriss Eds., Blackwell Science, 394 pp.

Leuning, R., and I.J. Foster, (1990) Estimation of transpiration by single trees: comparison of a ventilated chamber, leaf energy budgets and a combination equation. *Agric. For. Meteorol.*, 51:63-86

Lloyd C. R., (1995) : The effect of heterogeneous terrain on micrometeorological flux measurements: a case study from HAPEX-SAHEL. *Agric. For. Meteorol.*, *73*, 200-216

MacPherson, J.I., (1990) : Wind and Flux Calculations on the NAE Twin Otter. *Rep. LTR-FR-109*, Natl. Res. Counc., Ottawa. Ontario, Canada

MacPherson, J.I. and A. K. Betts, (1995) : Aircraft encounters with strong coherent vorteces over the boreal forest. 11th Symp. on Boundary Layers and Turbulence, *Amer. Meteorol. Soc.*, Charlotte, NC., March 27-31

MacPherson, J.I., (1996) : NRC Twin Otter Operations in BOREAS, *Rep. LTR-FR-129*,

Natl. Res. Counc., Ottawa, Ontario, Canada

MacPherson, J. I., and A. K. Betts, (1997) : Aircraft encounters with strong coherent vortices over the boreal forest. *J. Geophys.Res.* **102**(D24)29,231-29,235

Mahrt, L., (1998) : Flux sampling errors for aircraft and towers. *J. Atmos. Oceanic* Tech., **15**, 416-429

Mahrt L., and M. Ek, (1993) : Spatial variability of turbulent fluxes and roughness lengths in HAPEX-MOBILHY. *Boundary-Layer Meteorol.*, **65**, 381-400

Mahrt, L., J. I. MacPherson, and R. Desjardins, (1994) : Observations of fluxes over heterogeneous surfaces, *Boundary-Layer Meteorol.*, **67**, 345-367

Mahrt, L. and J. Sun, (1996) : Formulation of heat flux over the boreal forest. Proc. 22nd Conf. on Agric. and Forest Meteorol., *Amer. Meteorol. Soc.*, Atlanta, GA, Jan. 28 - Feb. 2, 1996, pp. 114-117

Manabe, S., and R. J. Stouffer, (1980) : Sensitivity of global climate change to an increase of CO_2 concentration in the atmosphere. *J. Geophys. Res.*, **8**, 5529-5554

Mann, J., and D. Lenschow, (1994) : Errors in airborne flux measurements. *J. Geophys. Res.* **99**(D7)14,519-14,526

McCumber, M.C. and R.A. Pielke, (1981) : Simulation of the effects of surface fluxes of heat and moisture in a mesoscale numerical model. Part1: Soil layer. *J. Geophys. Res.*, **86**, 9929-9983

Merriam D.F., and P. H. Sneath, (1966) : Quantitative Comparison of Contour Maps. *J. Geophys. Res.*, **71**, 1105-1115

Middleton, E. M., J. H. Sullivan, B.D. Bovard, A.J. Deluca, S.S. Chan, and T.A. Cannon (1997) : Seasonal variability in foliar characteristics and physiology for boreal forest species at the five saskatchewan tower sites during the 1994 Boreal Ecosystem-Atmosphere Study. *J. Geophys. Res.*, 102(D24), 28,831-28,844

Monteith, J.L., (1990) : Porometry and baseline analysis : the case for compatibility. *Agric. For. Meteorol.*, **49**, 155-167

Mitic, C. M., P. H. Schuepp, R. L. Desjardins, and J. I. MacPherson, (1995) : Spatial distribution and co-occurence of surface-atmosphere energy and gas exchange processes over the code grid site, *Atmos. Environ.*, **29**(21),3169-3180

NASA Goddard Space Flight Center (GSFC) (1995) : Boreal Ecosystem Atmosphere Study (BOREAS) experiment plan. Version 3.1, Greenbelt, Md.

NASA Goddard Space Flight Canter (GSFC), (1996) : Global warming, *NASA Facts*, NF-222

Nemani, R., Pierce, L., Running, S., and Goward, S. (1993) : Developing satellite derived estimates of surface moisture status, *J. Appl. Meteorol.*, **32**, 548-557

Norman J. M. and Becker, F. : 1995, 'Terminology in Thermal Infrared Remote Sensing of Natural Surfaces', *Agric. For. Meteorol.*, 77, 153-166.

Ogunjemiyo, O. S, P. H. Schuepp, J. I., MacPherson, R.L. Desjardins, (1997) : Analysis of flux maps vs. surface characteristics from Twin Otter grid flights in BOREAS 1994. *J. Geophys. Res.* **102**(D24), 29,135-29,147

Ogunjemiyo, O. S, N. Bussières, P. H. Schuepp, R. L. Desjardins, J. I MacPherson, (1998) : Comparaisons entre les cartes des flux d'humidité et de chaleur derivées de

mesures aeroportées et satellitaries pour un ecosystéme forestier boreal. *Le Climat*, **16**(01)11-32

Pederson, J. R., (1995) : California Ozone Deposition Experiment, methods, results and opportunities, *J. Atmos. Environ.*, **29**,3115-3132

Perry, E. M. and M. S. Moran, (1994) : An evaluation of atmospheric corrections of radiometric surface temperature for a semiarid rangeland watershed. *Water Resour. Res.*, **30**, 1261-1269

Ranson, K.J., G. Sun., R. H. Lang, N.S. Chauhan, R. J. Cacciola, and O. Kilic, (1997) : Mapping of boreal forest biomass from spaceborne synthetic aperture radar. *J. Geophys. Res.* **102**(D24)29,599-29,610

Salvage, K., T. R., Moore, and P. M. Crill, (1997) : Methane and carbon dioxide exchanges between the atmosphere and northern boreal forest soils. *J. Geophys. Res.* **102**(D24)29,279-29,288

Schuepp, P.H., J. I. MacPherson, and R. L, Desjardins, (1992) : Adjustment of footprint correction for airborne flux mapping over FIFE site, *J. Geophys., Res.*, **97**, 18,455-18,466

Schuepp, P.H., M.Y., Leclerc, J. I. MacPherson, and R. L, Desjardins, (1990) : Footprint prediction of scalar fluxes from analytical solutions of the diffusion equation. *Boundary Layer Meteorol.* **50**, No 3, 293-313

Schmid, H. P., (1994) : Source Areas for Scalars and Scalar Fluxes, *Boundary-Layer Meteorol.* **67**, 293-318.

Segal, M., R. Avissar, M. C. McCumber, and R. A. Pielke, (1989) : Evaluation of vegetation effects on the generation and modification of mesoscale circulations, *J. Atmos. Sci.*

45(16)2268-2294

Sellers , P.J., F. G . Hall, G. Asrar, D. E. Strebel, and R. E. Murphy, (1989) : The first ISLSCP field experiment (FIFE). *Bull. Amer. Meteorol. Soc.*, **69**(1), 22-27

Sellers, P., F. Hall, H. Margolis, B. Kelly, D. Baldocchi, G. den Hartog, J. Cihlar, M. G. Ryan, B. Goodison, P. Crill, K. J. Ranson, D. Lettenmaier, and D. E. Wickland, (1995) : The Boreal Ecosystem-Atmosphere Study (BOREAS): An Overview and Early Results from the 1994 Field Year', *Bull. Amer. Meteorol. Soc.*, **76** (9) , 1549-1577.

Shaw R. H., (1985) : On diffusive and dispersive fluxes in forest canopies. In *The Forest-Atmosphere Interaction* (edited by Hutchison B.A. and Hicks B. B), pp. 407-419. Reidel, Dordrecht

Shaw, R. H, K. T. Paw U, and W. Gao, (1989) : Detection of temperature ramps and flow structures at a deciduous forest site , *Agric. For. Meteorol.*, **47**, 123-138

Shuttleworth, W.J. (1989) : Micrometeoroloy of temperate and tropical forests, *Philos. Trans. R. Soc. London, Ser. B.*, **324**, 299-334

Stull, R. B., (1988) : An Introduction to Boundary Layer Meteorology, 666 pp., Kluwer Academic, Boston, Mass.,

Sud, Y.C., J. Shukla and Y. Mintz, (1988) : Influence of land surface roughness on atmospheric circulation and precipitation, a sensitivity study with a general circulation model. *J. Appl Meteorol.* **27**, 103-1054

Sun J., and L. Mahrt, (1994) : Spatial distribution of surface fluxes estimated from remotely sensed variables. *J. Appl. Meteorol.*, **33**, 1341-1353

Sun J., and Mahrt L., (1995) : Relationship of surface heat flux to microscale temperature variations: Application to BOREAS. *Boundary-Layer Meteorol.*, **76**, 291-301.

Swinbank, W. C., (1963) : Long-wave radiation from clear skies, *Quart. J. Roy. Met. Soc.* **89**, 339-348

Sykes, M.T., and I.C. Prentice, (1995). Boreal forest future : Modelling the controls on tree species range limit and transient responses to climate, *Water Soil Pollut.*, **82**, 45-48

Tans, P. P., I. Y. Fung, and T. Takahashi, (1990). Observational constrains on the global atmospheric CO_2 budget, *Science* **247**, 1431-1438

Townshend J. R. G. and C.O. Justice, (1995) : Spatial variability of images and the monitoring of changes in the normalized difference vegetation index, *Int. J. Rem. Sens.*, **16**, (12)2187-2195

Verma, S. B., J. Kim, R. J. Clement, N. J. Shurpail, and D. P. Billesbach, (1995): *Trace gas and Energy Fluxes: Micrometeorological perspectives* - In Soils and Global Climate Change Ed. J. Kimble, B.A Stewart, Lewis Publishers London.

Vining, R.C., and B. L. Blad, (1992) : Estimation of sensible heat flux from remotely sensed canopy temperatures. *J. Geophys Res.* **97**(D17), 18,951-18,954

Webb, E.K., G.I., Pearson, and R. Leuning, (1980) : Correction of flux measurements for density effects due to heat and water vapour transfer. *Quart. J. R. Met. Soc.* **106**, 85-100

Wyngaard J. C.,(1988) : Flow distorsion effects on scalar flux measurements in the surface layer - implications for sensor design, *Boundary-Layer Meteorol.*, **42**, 19-26

Wyngaard, J. C. (1990) : Scalar Fluxes in the planetary boundary layer -theory, modeling and measurement. *Boundary-Layer Meteorol.*, **50**, 49-75

Wyngaard, J. C. (1991) : On the maintenance and measurement of scalar fluxes. In : Schmugge T.J and André, J. C. (Eds) *Land Surface Evaporation: Measurement and Parameterization*, pp. 199-229. Springer-Verlag, New York.

APPENDIX

The material in the appendix is the English version of the paper that was published in French. It is not included in the main body of the thesis because, while related to the thesis, the topic was not the major theme of the thesis.

COMPARISON OF AIRBORNE AND SATELLITE-DERIVED MAPS OF HEAT AND MOISTURE FLUXES OVER A BOREAL FOREST ECOSYSTEM

I Abstract

Data from two grid flights flown on July 21 and July 26 1994, over a 16 km x 16 km heterogeneous site in the boreal forest were used to map spatial distributions of latent heat (LE) and sensible heat (H) fluxes at the site. The data were collected under convective atmospheric instability conditions, characterised by growing, warm and dry boundary layers. These data were compared against patterns in H and LE maps constructed from AVHRR satellite data acquired on both days. Analysis of the aircraft data showed H and surface temperature excess (T_s-T_a) were in poor agreement. Variation in surface cover was found to have a somewhat larger effect than radiation on the inhomogeneity of the surface fluxes at the site. Comparison of aircraft flux estimates to satellite estimates revealed discrepancies between the two data sets. Such discrepancies are attributed to the errors inherent in the linear conversion of T_s-T_a into H, and where T_s from satellite data are composite of canopy and soil temperatures.

II Introduction

The need to improve process model predictions of surface-atmosphere exchange has become a subject of great concern in recent years. Lower atmospheric processes are driven by surface related phenomena, whose large range of temporal and spatial scales, coupled with the heterogeneous nature of the earth surface, have made them difficult to be quantified. Flux density measurements are an effective way of integrating gas exchange and physiological processes on a field scale. Surface flux measurements from fixed point and airborne platforms have been used to estimate surface-atmosphere exchange processes. These methods have been compared in different studies in an effort to understand the nature of flux variation in the region between the surface and the lowest level of the aircraft as well as to lend credence to both methods of measurement [e.g. *Kelly et al.*, 1992]. Although direct flux measurements over relatively small areas can be made with available techniques in many

cases, obtaining good estimates at regional scales is much more demanding. The surface resistance to exchange, which is the limiting factor in the exchange of many gases at vegetated surfaces, is difficult to estimate for large areas because it is frequently highly variable in space and time and is strongly influenced by many environmental and biological factors. It is generally believed that the only feasible way of estimating surface energy fluxes over very large areas is through the use of satellite data.

Comparison of satellite data with surface observations over a wide range of spatial and temporal scales requires sampling of surface conditions on small spatial scales over a region large enough to be observed by satellite, and for periods long enough to obtain a meaningful range of surface conditions, i.e. most of a growing season. Even in cases where experimental designs meet these criteria, evaluation of surface fluxes from remotely sensed satellite data has relied on boundary layer models, since fluxes arise from low level gradients of temperature and humidity that cannot be directly measured from space-based remote sensing instrument. The prospect of estimating surface fluxes over larger area therefore depends on how successfully it relates the fluxes obtained from aircraft or surface based systems to satellite-acquired data of surface characteristics. While many models have been developed over the past two decades, few experiments have been conducted on a scale large enough to provide data for the validation of these models. The Boreal Ecosystem Atmosphere Study (BOREAS) was one of those large scale experiment designed to study the complex interactions occurring at the surface and also to provide data on surface fluxes that can be used to validate process models that use remote sensing data.

Our study used data obtained from the Canadian Twin Otter aircraft over a 16 km x 16 km grid site at the Southern Study Area (SSA) of BOREAS, on July 22 and 26. It examines the variability in fluxes of heat and moisture over the grid site, and to explores the potential ability of satellite-derived estimates to reproduce such distributions.

III Description of the study area.

The SSA of BOREAS is located near Prince Albert, Saskatchewan. The lowland forest of the boreal ecosystem in Saskatchewan grow on flat terrain with a mineral soil base

overlain by a very thin layer of live and decomposed moss, with shallow root zone for conifers [*Sellers et al.*, 1995].

The 16 km x 16 km grid site over which the Twin Otter surface flux observations were made is big enough so that the turbulent structure of the planetary boundary layer could be adequately sampled by aircraft and a reasonable number of satellite pixels could be placed within the site boundary [*Sellers et al.*, 1995].The diagonal corners for the grid site are located at 53.92 ° N/104.81 ° W and 53.78 ° N/104.56 ° W. About 80% of the area is covered by forest, 60 % of which is wet conifers interspersed with fen, and about 12 % is taken up by clearcut. The area beneath the NW-SE diagonal generally contains wetter surfaces, with mixed fen and forest. Forest cover is often controlled by small changes in relief and soil or drainage characteristics.

IV Data Collection And Processing

Data were collected by the Canadian Twin Otter atmospheric research aircraft [*MacPherson*, 1996] in a grid pattern over the site in north-south trajectories. Each grid flight consisted of nine parallel straight lines, spaced 2 km apart, with each line sampled twice in a time-centermode. Aircraft sampling height was maintained at 30 m above the ground level. The aircraft data used for our analysis included air temperature (T_a), surface temperature (T_s), the three components of the vertical wind, incident radiation, and water vapor mixing ratio. Parameters derived from measured variables include net radiation, R_n, difference between surface and air temperature (T_s - T_a) and potential temperature (θ). Data were digitized at 16 Hz. Where necessary, corrections were applied for delays between signals recorded at different sensor locations. Because of the low flight altitude, no atmospheric correction was applied to the airborne radiometric observations. However, the aircraft surface radiation temperature was corrected for surface emissivity [*Sun and Mahrt*, 1995] as

$$T_s = \left(\frac{R\uparrow - (1-\epsilon) R\downarrow}{\epsilon \sigma} \right)^{1/4} \qquad (1)$$

where R↑ is the long-wave radiation, R↓ is the downward radiation, σ is the Stefan Boltzman constant and ϵ is the surface emissivity, which was taken to be 0.97.

All the data were collected around solar noon, under clear weather conditions. The

average temperature for both days was 25 °C, the mean wind was 4.9 m s^{-1} on July 21 and 1.4 m s^{-1} on July 26. Average wind direction was westerly, and thermal stratification was unstable (z/L ≡-0.43). Using aircraft data, the sensible heat and latent heat fluxes were estimated by the eddy correlation technique, after the data were detrended using the criteria outlined in *Ogunjemiyo et al.* [1996]. To remove the effect of altitude changes during flux measuring runs, the potential temperature (θ) was used to compute sensible heat flux (H), and mixing ratio for H_2O, to avoid the need for density correction [*MacPherson*, 1990]. All maps were constructed from 2 km windows along the flight paths, with a 1 km overlap.

NOAA AVHRR Satellite scenes for July 21 at 2205 UTC and 26 at 2244 UTC, 1994 were available for comparisons with the airborne temperature observations. It is assumed that surface patterns are consistent during the afternoon, so that comparison between noon aircraft and late afternoon (2205 UTC=1605 local) temperature observations are possible. Calibrated brightness temperatures from AVHRR channel 4 and 5 were converted to atmospherically-corrected T_s using the method of *Sobrino et al.* [1991]. Air temperatures were extracted from the Canadian Meteorological Centre's regional finite element model (RFE), at the height of the first model layer, approximately 87 m above the surface. Daily heat flux was computed according to *Rambal et al.* [1985],

$$H \propto B(T_s - T_a)^{3/2} \qquad (2)$$

where B is the heat transfer conversion coefficient, with a value of B=0.20 based on previous studies in southern Saskatchewan. The latent heat flux (LE) was estimated on the basis of the following energy balance approximation

$$LE \propto R_n - H - 0.1R_n \qquad (3)$$

where R_n is the net radiation and 0.1 R_n is an approximation to heat transfer to the ground.

V RESULTS AND DISCUSSIONS

(i) The surface minus air temperature (T_s- T_a)

The aircraft-based estimates (T_s- T_a), latent heat flux and sensible heat flux for July 21 and July 26 are mapped in Figure 1. The corresponding maps for the satellite data are shown

in Figure 2. The (T_s- T_a) maps show the thermal signature of the site, and reflect spatial variations in the utilization of radiant energy among the different surface types that dominate the energy partitioning at the site. General agreement can be seen between the aircraft and satellite (T_s- T_a) patterns, even though the observation time of the two data sets was separated by about 4 hours. The relationship between airborne and satellite-observed T_s on July 26 is shown in Figure 3. The correlation between the two data set is 0.81, while correlation on July 21 was only 0.56, probably due to cloud cover that partly obscured the site during the satellite overpass. Both data sets show a greater spatial variability in (T_s- T_a) on July 26 than on July 21. The differences in the range of (T_s- T_a) between the two data sets are associated with the differences in their spatial resolution, which is about 4 m for the aircraft and 1.1 km for the satellite data. This is also related to the methods to obtain T_a, a spatially smooth estimate being made at 87 m height from a 50 km resolution weather model for use in the satellite algorithim, and a high spatial resolution aircraft observation being made at 30m height.

Radiative temperatures are directional properties that depend on the surface physical and chemical properties in addition to the illumination and viewing angles [see *Fuchs et al.*, 1967; *Kimes et al.*, 1980; *Huband and Monteith*, 1986; *Kustas et al.*, 1989; *Vining and Blad*, 1992]. It has also been demonstrated by *Vining and Blad* [1992] that these directional properties may be affected by external factors such as surface winds, which alter the geometric configuration of vegetation. Spatial variation in radiation temperature at the site is to a large extent determined by heterogeneity of soil moisture and canopy architecture. The low surface temperature excess of areas predominantly covered with wet coniferous forest (dark areas in Fig. 1) has been attributed to underestimation of canopy temperature by downward looking radiometers with moist, shaded ground between trees within their view field [*Hall et al.*, 1995; *Sun and Mahrt*, 1995]. High temperature excess (light shading), especially around the middle of the site to the north-eastern edge, is associated with the logged and regenerating areas.

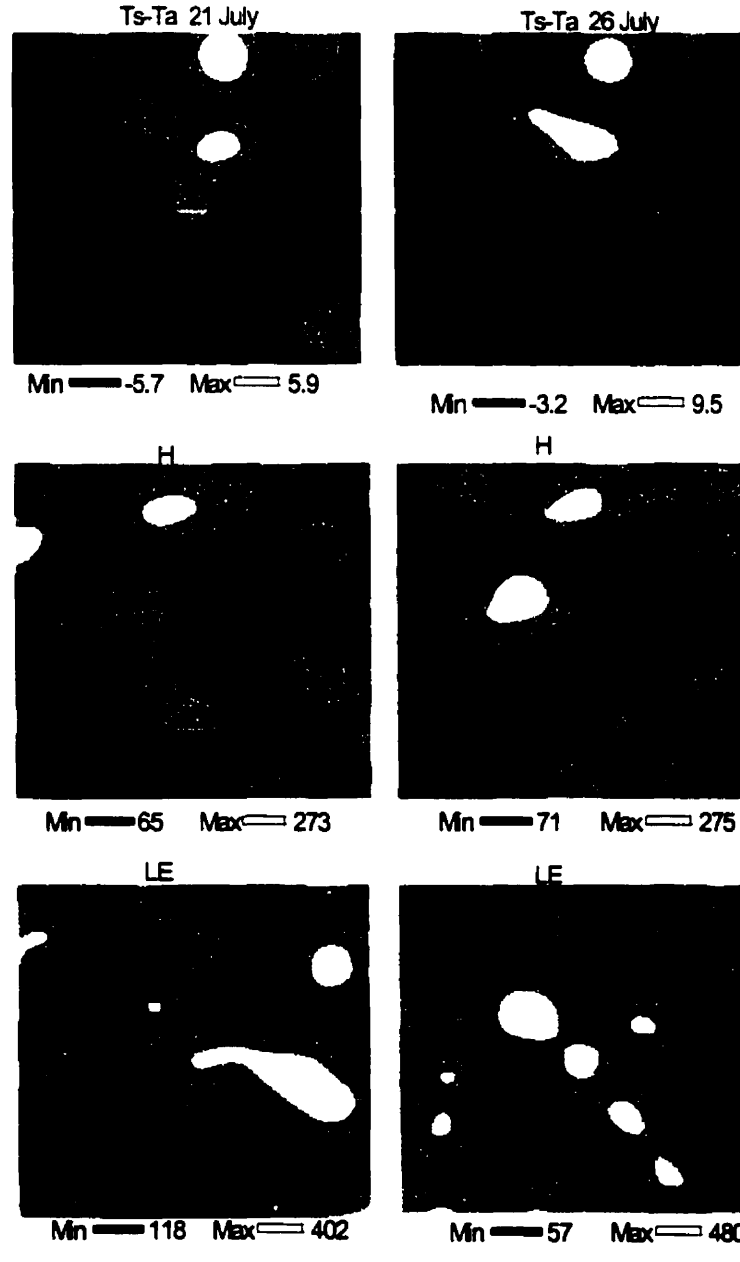

Figure 1. Aircraft T_s-T_a (°C), H (W m^{-2}), and LE (W m^{-2}) maps for July 21 and July 26.

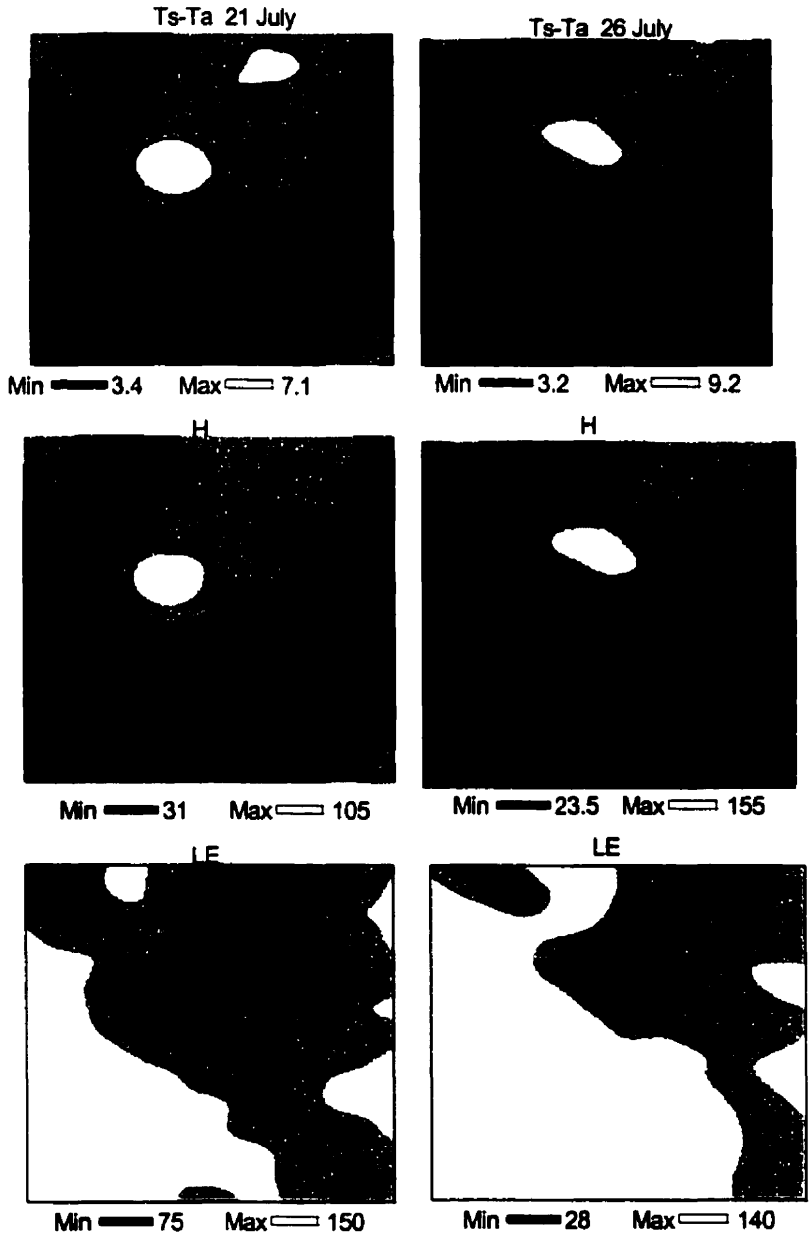

Figure 2. AVHRR T_s-T_a (°C), H (Mj m^{-2} day^{-1}) and LE (Mj m^{-2} day^{-1})for July 21 and July 26.

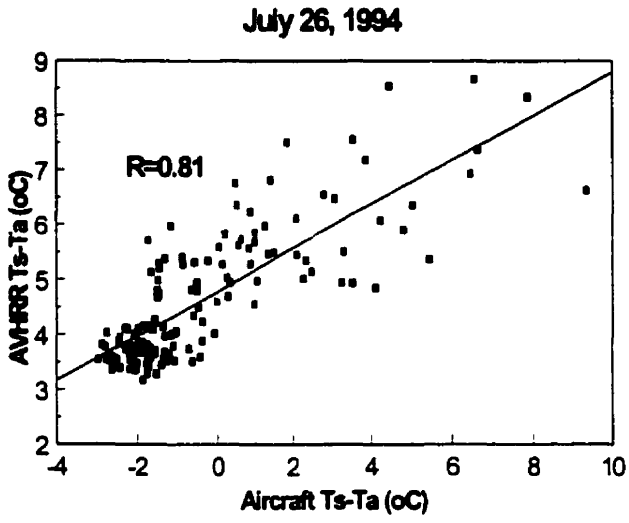

Figure 3 . Aircraft versus satellite T_s-T_a

(ii) Maps of sensible and latent heat fluxes from airborne observations

As seen in all the maps, the grey scales for each of the variables are not the same on both days, since more emphasis in this study is on variability rather than on absolute value of the variables. Some distinct, common patterns can be seen in the aircraft sensible heat flux maps on both days. They include two local maxima at the northern part of the site, over old jack pine and regenerating areas, and two local minima at the southwestern and southeastern edges of the site. By comparing (T_s-T_a) and sensible heat flux maps one can see that the clear distinction in surface temperature excess between the cool coniferous region with fen, below the NW-SE diagonal, and the warmer areas above it, is not reflected in a similar contrast in sensible heat flux. Aircrfat estimate of H and (T_s-T_a) are partially decoupled. It is mainly attributed to the viewing angle problem of the radiometer; the posibility of this being caused by advection effect is not supported by the conditions under which the data were collected and by budget estimate of H. The grid flights were flown around local noon, under unstable atmospheric stability when turbulent transfers dominate vertical scalar transports. There was lack of pronounced horizontal gradient in surface cover for most wind directions at spatial

scales relevant to our flight level. Besides these factors, the upper-air budget analysis carried out by *Barr et al.* [1997] showed that horizontal advection contributed negligibly to H and LE estimates.

Compared with the sensible heat flux maps, the aircraft latent heat flux maps show less characteristic patterns that are common to both days. The relative maximum of LE diagonally across the grid is most likely associated with a preponderance of aspen along the diagonal, and the relatively elevated LE in the SW corner with fen interspersed among the forest.

(iii) Comparison of aircraft and satellite-derived flux estimates.

The application of equation 2 to satellite T_s data generates H patterns which agree poorly with H patterns from aircraft estimates. It suggests that the required conditions for using Equation 2, i.e. the coupling between H and (T_s-T_a), were not satisfied at the grid site. Where these conditions are satisfied, as in homogenous areas with essentially full canopy cover, such equations have produced satisfactory results [*Stone and Horton*, 1974; *Hatfield et al.*, 1984; *Reginato et al.*, 1985; *Choudhury et al.*, 1986]. The application of equation 3 to satellite data also generates LE patterns which agree poorly with LE patterns from aircraft estimates. Errors in the determination of H when estimating LE as a residual in the energy balance equation (Equ. 3), contribute significantly to the disagreement between aircraft-observed flux patterns and those estimated from satellite-based temperature observations. The partial decoupling between H and (T_s-T_a) (as seen in section 3.2 above), is one of the main findings of BOREAS 1994, tentatively associated with aerodynamic and physiological decoupling of tree crown, where sensible heat is primarily exchanged, from the wet and cool underlying area which affects the radiometric field of view. Difficulties in estimating H from remote sensing data due to viewing angle effects were also reported by *Leckie et al.* [1981], *Kustas et al.*[1989], *Paw U et al.* [1989], *Hall et al.* [1992], and *Sun and Mahrt* [1995].

This raises the question of adjustments that might enable Equation 2 to predict sensible heat flux in cases where viewing angle effects become a problem (i.e. where the soil surface is only partly covered by vegetation and the surface temperature measured is a

composite of the vegetation and the substrate). Many approaches have been proposed by different workers to address this issue. For instance *Vining and Blad* [1992], proposed that at wind speeds of less than 4 m s^{-1}, good estimate of H can be made using surface temperatures made at a zenith angle of 40°, whereas for wind speeds greater than about 5 m s^{-1}, the angle should be between 0° and 20°. However, this approach is not practical for airborne and satellite-based measurements. *Hall et al.*, [1992] used the canopy aerodynamic temperature (T_{aero}), estimated as a function of T_s, rather than T_s, but T_{aero} is poorly defined in terms of T_s and small errors in estimating T_s can create large errors in H. Neural network simulation has shown potential for deriving physically meaningful measures of T_a from T_s over simple (grassland) ecosystems [*Abareshi and Schuepp*, 1998], but it is not yet clear if a similar approach is workable for the much more complex forest ecosystem. *Shuttleworth and Wallace* [1985], proposed a two-dimensional approach for partial canopy conditions by partitioning the surface energy balance between the substrate and the vegetation. The problem with this approach is that the actual data required by the model may make it too complicated to implement from an operational standpoint.

The question as to what radiometrically observed T_s represents, is a difficult one. As our analysis has shown, the relationship between H and T_s-T_a is not linear. The poor performance of Equation 2, even when the nonlinearity effect is accounted for, suggests that further amendments to the equation may be necessary, such as the introduction of extra resistance to the heat transfer. As suggested by *Kustas et al.* [1989], this resistance must in some way account for the shift of the source height for H from the soil to the vegetative surfaces.

(iv) Factors affecting the variability of aircraft measured sensible and latent heat fluxes.

Variability of surface fluxes is controlled by many factors. Some represent permanent features of the landscape while others involve underground hydrological processes, boundary layer structure, factors imposed by man in term of land utilization (for example, burning and logging), and radiant energy supply. Plant factors such as leaf area index, density and size of the stomata, depth of the active root zone and type of vegetation also play an important role in controlling surface fluxes. Since the root zone moisture does not appear to exert a major control to the surface energy balance in the boreal forest [*Sellers et al.*, 1995], it can

be said that the surface flux variability is primarily due to the non-uniform distribution of the incoming energy, and the inhomogeneity of surface covers which react differently to this incoming energy. Our concern here is to examine which of these two factors has greater influence on the spatial variability of the fluxes, and to explore the possibility of relating the surface fluxes to boundary layer (BL) structures.

Table 1 shows the estimates of incoming radiation R↓, net radiation, R_n, H and LE for July 21 and July 26 based on averaging over all the flight data (grid average) and on the interpolated maps at the 135 points used to construct the maps (map estimates). The solar radiation received at the site during the flight is almost uniformly distributed on July 21, with a standard deviation (*s*) of 13.5 Wm^{-2} and a spatial range (max-min) of less than 60 Wm^{-2}, unlike on July 26 when *s* is 65.7 Wm^{-2} and the spatial range is about 300 Wm^{-2}. It is surprising to see that this difference in R↓ between the two days is not reflected in H estimates but possibly in LE estimates. The grid average and the spatial range of H is almost the same for both days, while for LE the grid average is higher on July 26 by 18 Wm^{-2} and the spatial ranges are about 300 Wm^{-2} and 400 Wm^{-2}, on July 21 and July 26, respectively. The fact that higher radiation levels do not necessarily lead to higher absolute values of moisture (and CO_2) has been tentatively associated with a high degree of stomatal control of the coniferous trees which appear to be moisture stressed at relatively low radiation levels at the given sites [*Sellers et al.*, 1995]. The response in spatial distribution of LE to spatial distribution in radiation might be due to the unusual wetness of the site at the time of observation, with spatially varying patches of surface water whose exchange is controlled by available radiant energy rather than physiological response.

The coefficient of variations (*cv*) of surface fluxes of latent heat, sensible heat and net radiation were used by *Hiyama et al.*[1995] to asses whether surface cover or radiation had larger effects on the inhomogeneity of the surface fluxes over a heterogenous experimental site during TABLE 92. Based on their approach the surface cover has a greater effect if the *cv* of the fluxes are higher than that of the radiation. Using the same approach and the values of *cv* in Table 1, it is clear that despite the large variations in LE due to variations in the radiation, the variation in surface cover had a somewhat larger effect compared to radiation, on the inhomogeneity of the surface fluxes at the site.

Table 1. Summary statistics of the aircraft grid data based on the run averages (grid average) and the flux maps data (from map estimates).

			From map estimates				
		Grid Avg Wm^{-2}	Min Wm^{-2}	Max Wm^{-2}	Mean Wm^{-2}	*S* Wm^{-2}	*CV*
July 21	R_l	771.8	723.0	781.0	760.5	13.5	0.02
	R_n	630.4	590.6	667.3	640.0	15.0	0.02
	LE	237.3	118.9	402.6	232.3	54.2	0.23
	H	157.7	65.0	273.0	156.0	37.3	0.24
July 26	R_l	705.9	396.0	792.9	698.4	65.7	0.09
	R_n	554.9	307.2	653.7	573.5	59.1	0.10
	LE	219.4	57.9	500.7	223	65.0	0.29
	H	156.6	71.6	275.8	156.2	41.2	0.26

The structure and growth of the boundary layer depend on the exchange of sensible and latent heat at the surface. The balance between the surface fluxes and the entrainment determines the rate of boundary layer deepening, warming and moistening (or drying). Boundary layer profile analysis over the study area by *Barr et al.* [1997] showed a well developed nocturnal BL in early morning soundings, which gave way to mixed-BL development by 1515 GMT. The analysis also showed that a well defined superadiabatic zone underlay the mixed BL. Figure 4 shows the BL profiles on July 21 and July 26, during the period when the grid flights were executed. The upper-air soundings shown here were taken about 5-10 minutes after the start (1716 GMT) and the end (1917 GMT) of each flight, and fairly represent the BL conditions during the flights. Thermal stratification was unstable in all cases, with average z/L of -0.14 on July 21 and -0.73 on July 26. The mixed layer growth started earlier on July 21, and by 1716 GMT the height (z_i) has reached 1.19 km as against 0.64 km on July 26. The execution of the grid flight coincided with a slow growth phase of the mixed layer on July 21 and a high growth phase on July 26, leading to Δz_i of 0.17 km on July 21 compared to 0.73 km on July 26. The marked difference in stability parameter between these days suggests a difference in the flux footprint, a factor which can

cause differences in flux patterns. The low average wind speed (1.4 m s^{-1}) on July 26 coupled with intense vertical mixing favoured the development of thermal and moisture plumes that could bias grid estimates, and may partly explain the large spatial variations in fluxes that are associated with this day's grid flight.

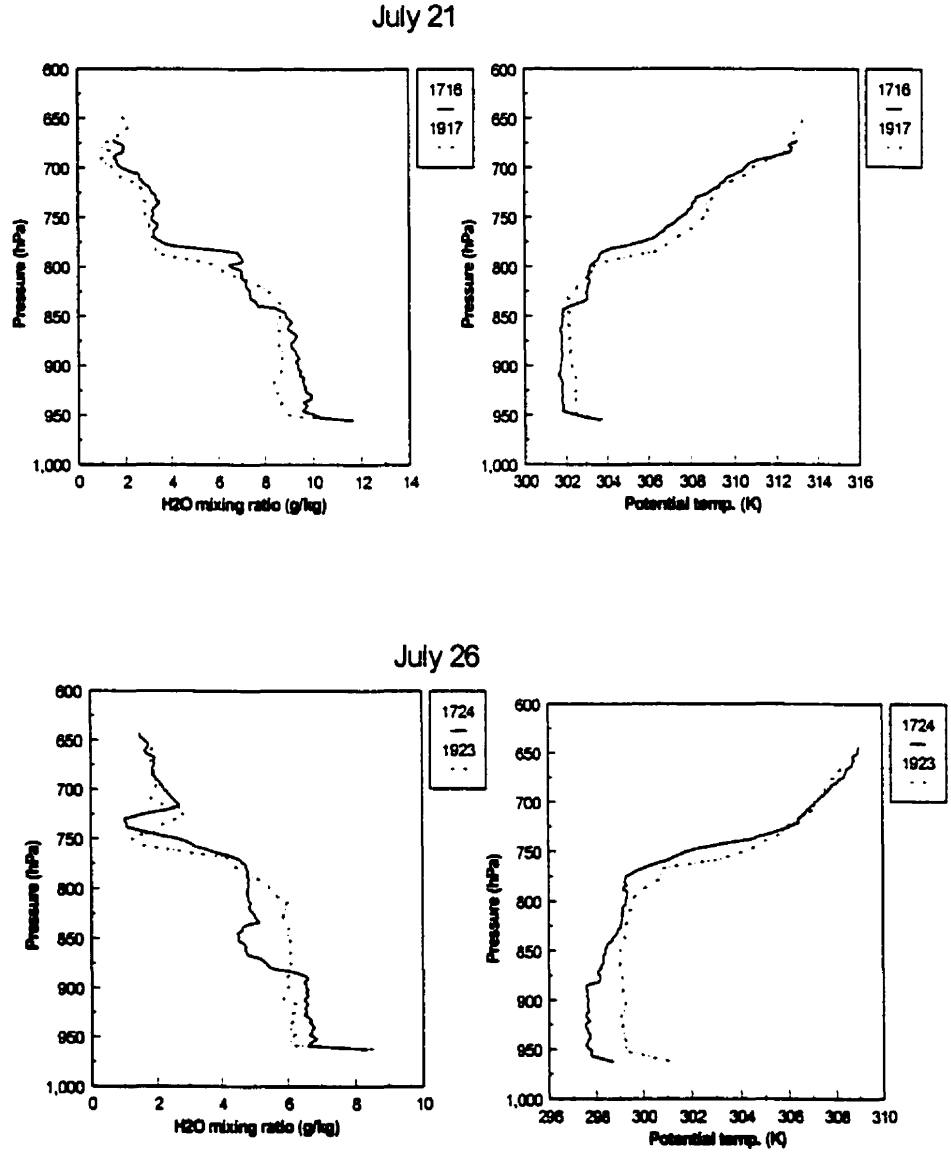

Figure 4. Boundary layer profile of potential temperature and water mixing ratio for July 21 and July 26

By comparing the profiles of July 21 and July 26, it is apparent that the BL was more humid and warmer on July 21 than on July 26. Average BL θ and q were 302.1 K and 9.1 g kg^{-1} on July 21 compared to 298.4 K and 6.4 g kg^{-1} for July 26. These differences, however, are not reflected in the grid average fluxes, especially in H, which is almost the same for both days. Considering the low value of θ on July 21, the relatively high corresponding value of H can be related to higher convective instability and higher change in θ that occurred during the flight. The changes in θ and q during the flight were 0.41 °C and -0.855 g kg^{-1} on July 21, while the corresponding changes on July 26 were 1.51 °C and -0.589 g kg^{-1}, respectively. The negative Δq and positive $\theta\Delta$ indicate drying and warming of the BL. The vapour pressure deficit (VPD) obtained by averaging data from the three towers within the site showed that VPD increased steadily during the flight, with magnitude about the same on both days. This trend in VPD close to the surface and the drying of the BL provided favourable conditions for evapotranspiration, and may partly explain the high latent heat fluxes that were measured by the aircraft. The behaviour of the BL can also be used to explain the differences in flux patterns between the two days.

VI Conclusion

An attempt is made to interpret energy flux distribution over a 16 km x 16 km site in the boreal forest, in terms of surface characteristics obtained by radiometric remote sensing from aircraft and satellite. Preliminary analysis suggests that variability in surface fluxes at the site were associated more with heterogeneity of the surface cover than with variations in available radiant energy. The analysis also showed that remotely sensed surface temperature over the boreal ecosystem covered by the datasets is a poor indicator of the canopy temperature due to the problem associated with the viewing angle of the radiometers. The poor coupling between aircraft-measured heat fluxes and temperature differences between surface and atmosphere (T_s-T_a) resulted in weak agreement between these fluxes, and those estimated from satellite, based on radiometric surface temperatures. This result poses a challenge to the prediction of the surface energy balance from satellite-based remote sensing observations. It suggests that in order to successfully estimate sensible heat flux from

remote sensing data over heterogenous surfaces (and latent heat flux as a residual in the energy balance), a non-linear relationship between sensible heat flux (H) and T_s-T_a be considered, with appropriate adjustment that will account for the possible shift of the source height for H from the soil to the vegetative surfaces.

References:

Abareshi, B., and P.H., Schuepp, (1998) : Sensible heat flux estimation over the FIFE site by Neural Networks. *J. Atmos. Sc.* **55**,1185-1197

Barr, A.G., and A. K. Betts, (1997) : Radiosonde boundary layer budgets above a boreal forest. *J. Geophys. Res.* **102**(D24), 29,205-29,213

Choudhury, B. J., R. J. Reginato, and S. B. Idso, (1986): Analysis of infrared temperature observations over wheat and calculation of latent heat flux. *Agric. For. Meteorol.* **37**, 75-88.

Fuchs, M., E. T. Kanemasu, J. P. Keer, and C. B. Tanner, (1967) : Effect of viewing angle on canopy temperature measurements with infrared thermometers, *Agron, J.*, **59**, 494-496

Hall , G. H., K. F. Huemmrich, S. J. Goetz, P. J. Sellers, and J. E. Nickson, (1992) : Satellite remote sensing of surface energy balance: Success, failure, and unresolved issues in FIFE, *J. Geophys. Res.*, **97**(D17), 19,061-19089

Hall, F. G., Y. E. Shimabukoro, and K. F. Huemmrich (1995) : Remote sensing of forest biophysical structure using mixture decomposition and geometric reflectance models, *Ecol. Appl.*, **5** *(4)*, 993-1013, 1995

Hatfield J. L., R. J. Reginato, and S. B. Idso (1984) : Evaluation of canopy temperature - Evapotranspiration models over various crops, *Agric. For. Meteorol.*, **32**, 41-53

Hiyama T., M. Sugita, and I. Kayane (1995) : variability of surface fluxes within a complex area observed during TABLE 92, *Agric. For. Meteorol.*, 73, 189-207

Huband, N. D., and J. L. Monteith, (1986) : Radiative surface temperature and energy balance of wheat canopy, 1, Comparison of radiative and aerodynamic temperatures, *Boundary-Layer Meteorol.*, **36**, 1-17

Kelly, R. D., Smith, E. A., MacPherson, J. I., (1992) : A comparison of surface sensible and latent heat fluxes from aircraft and surface measurements in FIFE 1987, *J. Geophys. Res.* **97** (D17), 18445-18453

Kimes, D. S., S. B. Idso, P. J. Pinter, Jr., R. J. Reginato, and R. D. Jackson, (1980) : View angle effects in the radiometric measurements of plant canopy temperatures, *Remote Sens. Environ.*, **10**, 273-284

Kustas, W. P., B. J. Choudhury, M. S. Moran., R. J. Reginato, R. D. Jackson, L. W. Gay, and H. L. Weaver, (1989) : Determination of sensible heat flux over sparse canopy using thermal infrared data, *Agric. For. Meteorol.*, **44**: 197-216

Leckie, D. G., T. A. Black, and P. A. Murtha, (1981): Development and testing of a method of estimating sensible heat from natural surfaces using remotely sensed surface temperatures, *Can. J. Chem. Eng.*, **59**, 189-193

MacPherson, J.I, (1990): Wind and Flux Calculations on the NAE Twin Otter. *Rep. LTR-FR-109*, Natl. Res. Counc., Ottawa, Ontario, Canada

MacPherson, J.I., (1996) : NRC Twin Otter Operations in BOREAS, *Rep. LTR-FR-129*,

Natl. Res.Counc., Ottawa, Ontario, Canada.

Ogunjemiyo, O. S, P. H. Schuepp, J. I., MacPherson, R.L. Desjardins, (1997) : Analysis of flux maps vs. surface characteristics from Twin Otter grid flights in BOREAS 1994. *J. Geophys. Res.* **102**(D24), 29,135-29,147

Paw U., K. T., S. L. Ustin, and C. A. Zhang, (1989) : Anisotropy of thermal infrared reflectance in sunflowers canopies, *Agric. For. Meteorol.*, **48**, 45-85.

Rambal, S., B. Lacaze., H. Mazurek, and G. Debussche, (1985) : Comparisons of hydrologically simulated and remotely sensed actual evapotranspiration from some Mediterranean Vegetation Formulations. *Int J. Remote Sensing,* **6** (8), 1475-1481

Reginato, R. J., R. D. Jackson, and P. J. Jr. Pinter (1985), Evapotranspiration calculated from remote multispectral and ground station meteorological data, *Rem. Sens. Environ.*, **18**, 75-89.

Sellers, P., F. Hall, H. Margolis, B. Kelly, D. Baldocchi, G. den Hartog, J. Cihlar, M. G. Ryan, B. Goodison, P. Crill, K. J. Ranson, D. Lettenmaier, and D. E. Wickland (1995) : The Boreal Ecosystem-Atmosphere Study (BOREAS): An Overview and Early Results from the 1994 Field Year', *Bull. Amer. Meteorol. Soc.*, **76** (9) , 1549-1577.

Shuttleworth, W. J., and J. S. Wallace, (1985) : Evaporation from sparse crops - An energy combination theory, *Q. J. R. Meteorol. Soc.*, **111**, 839-855

Sobrino, J. A., C. Coll, and V. Caselles, (1991) : Atmospheric correction for land surface temperature using NOAA-11 AVHRR channels 4 and 5. *Remote Sens. Environ.* **38**(19),19-34

Stone, L. R. , and M. L. Horton, (1974) : Estimating evapotranspiration using canopy temperatures: field evaluation, *Agron. J.*, **66,** 450-454

Sun J. and L. Mahrt, (1995) : Relationship of surface heat flux to microscale temperature variations: Application to BOREAS, *Boundary Layer Meteorology* **76**: 291-301

Vining, R. C., B. L., Blad, (1992) : Estimation of sensible heat flux from remotely sensed canopy temperatures, *J. Geophys. Res.*, **97**(D17), 18951-18954